Université d'Évry-Val-d'Essonne – Université Paris-Saclay

Mémoire présenté pour obtenir

le diplôme d'Habilitation à Diriger des Recherches

de l'Université d'Évry-Val-d'Essonne

Spécialité : Mathématiques Appliquées

par

Alexandre VIDAL

Maître de Conférences

From qualitative analysis of complex dynamics to parameter estimation in neuronal models

Rapporteurs :

Stephen Coombes, Professor (University of Nottingham, United Kingdom)
Peter De Maesschalck, Professor (Universiteit Hasselt, België)
Nikola Popovic, Senior Lecturer (University of Edinburgh, United Kingdom)

Soutenance le mercredi 14 décembre 2016 devant le jury composé de :

Stephen Coombes, Professor, rapporteur (University of Nottingham, United Kingdom)
Peter De Maesschalck, Professor, rapporteur (University of Hasselt, België)
Béatrice Laroche, Directeur de Recherches, examinateur (INRA Jouy-en-Josas, France)
Pierre-Gilles Lemarié-Rieusset, Professeur, examinateur (Université d'Evry, France)
Alain Miranville, Professeur, examinateur (Université de Poitiers, France)
Nikola Popovic, Senior Lecturer, rapporteur (University of Edinburgh, United Kingdom)
Marie Postel, Maître de Conférences HDR, examinateur (Université P. & M. Curie, France)

Remerciements

Je tiens à exprimer ma gratitude aux rapporteurs et aux membres du jury qui ont accepté d'évaluer mon travail. Je suis très reconnaissant à Stephen Coombes, Peter De Maesschalck et Nikola Popovic pour le temps et l'énergie qu'ils ont consacrés à l'étude de mes travaux et à la rédaction des rapports. Je remercie chaleureusement Béatrice Laroche, Alain Miranville, Pierre-Gilles Lemarié-Rieusset et Marie Postel pour leur présence en tant que membre du jury.

Je remercie également mes collaborateurs avec une pensée spéciale pour Frédérique Clément, Habib Benali et Jonathan Touboul. Je remercie Jean-Pierre Françoise pour ses précieux conseils. J'adresse une pensée particulière à Justyna, Soledad, Aurélie et Elif.

Mes pensées vont également à tous mes collègues du LaMME avec lesquels j'éprouve un réel plaisir à travailler et interagir dans une ambiance si plaisante. Je remercie particulièrement Pierre-Gilles, Arnaud et Marie-Luce pour leur appui et leur bienveillance.

À Soen, Elynn, Emilie et mes parents

Contents

Introduction and Outline

Qualitative analysis of dynamical systems in its broader sense addresses the question of characterizing the essential structure of dynamics for describing the phase portrait and, therefore, the qualitative properties of a system, in particular according to the values of its parameters. The theories that have been (and keep being) developed with this aim, such as bifurcation theory and geometric singular perturbation theory, provide useful tools for analyzing the dynamical mechanisms underlying the complex behaviors of a system. Yet, they even overcome this goal by providing rigorous results to approximate or reduce the dynamics and to stress the structure of the parameter space according to the panels of behaviors that the system can adopt. Therefore they offer a better context to retrieve also quantitative information on the generated orbits.

Naturally applied to models in life sciences for characterizing the impact of the parameters on the orbits (and thus the signals generated by the state variables), qualitative analysis has been proven to be particularly useful in the neuroscience field. The general purpose of mathematical neuroscience is to develop models and dedicated analysis methods to better apprehend complex relationships between brain function and structure. In addition to gaining a better understanding of neural compartments and their dysfunctions, this process enables a transfer of neuroscience knowledge by offering new ways to process information. To develop new models, to study their mathematical properties for judging their ability to reproduce individual or mesoscopic activities, and to fit their outputs with actual data, allow us to improve our understanding of the mechanisms of brain function in humans and animals.

In this context, the problematic of parameter estimation in models generating complex behaviors (transitory regime, complex oscillations, differential response to impulse) appears to be essential. Methodological tools based on original approaches are needed to tackle this question, and may differ according to the model features and the biological knowledge (from both the theory and the experimental data). From the application viewpoint, they rely on original processes for model fitting and an unusual approach of experimental signals for retrieving information relevant to the dynamical mechanisms.

This manuscript present models, using the dynamical system formalism, developed at different scales (individual, population, network) of several neural activities. It summarizes results obtained from the analysis of these systems generating complex oscillations based on bifurcation analysis, geometric singular perturbation theory and desingularization methods. Although the models share common features such as formalism and relative low-dimension, they differ in their structure and properties, as well as the level of interpretation of the parameters. Hence the link between the dynamics analysis and the parameter estimation is a two-way road. The challenge can be to fit the outputs of the system to given quantitative features (with biologically relevant hypothesis). Or it can consist, for a model based on known biological mechanisms, in exploring the panel of behaviors, identifying the regions in the parameter space corresponding to each of them and studying the associated transitions between them. Within this latter question, we focus on Mixed-Mode Oscillations (MMOs) and Mixed-Mode Bursting Oscillations (MMBOs) generated by two different mechanisms: the canard-induced MMOs in differentiable dynamics and a geometric mechanism in a hybrid system.

The presented results are based on the published articles [5, 6, 9, 10, 12, 13, 14, 15] and studies submitted for publication [16, 17, 19] listed in the Internal References at the end of this manuscript. The manuscript is organized as follows.

Chapter 1. We introduce basic models (in the sense that they will be used for building more sophisticated ones) of neural activities, either well-known – non-linear Integrate-and-fire, FitzHugh-Nagumo – or proposed for the first time in the above articles – intracellular calcium concentration (ICC) model, Gonadotropin Releasing Hormone (GnRH) secretion model, extended neural-mass model (NMM), neuron-glia mass model (NGMM). The chapter is split according to the scale of the modeling paradigm: individual cell activities and mass approach considering coupled neuron populations. We briefly recall the structure of each model (biological mechanisms, state variables and parameters), its qualitative behavior and results needed for subsequent analysis.

Chapter 2. We present methodological tools based on bifurcation analysis and geometric singular perturbation for tackling the question of parameter estimation in different contexts defined by the considered model and the associated quantitative specifications brought by the biological knowledge. We summarize theoretical results, based on implicit reductions to slow manifolds, that ground a method for tuning the parameter of the three timescale GnRH Secretion model to reach quantitative specifications [5]. We present a method based on MMOs analysis for reproducing the variable oscillatory patterns in ICC with the corresponding model [10]. We present the results of a bifurcation analysis of the NMM for (i) characterizing the panel of possible qualitative patterns, (ii) studying the impact of each excitatory feedbacks involved in the model, (iii) reproducing an experimental time-series recorded in an epileptic mice [13]. We combine bifurcation theory and classical constrained optimization method for characterizing the quantitative conditions on coupling gain parameters of the NGMM corresponding to differential response to astrocyte deficiency [15].

Chapter 3. We study MMOs and MMBOs pattern generated by the GnRH secretion model [9], on the one hand, and by the non-linear integrate-and-fire model [19], on the other hand. In both cases, we focus on characterizing the parameter values corresponding to specific features in

the signature and its changes with parameter values. In the first case, we use blow-up methods for desingularizing a three-time scale reduction of the GnRH secretion model featuring a folded node and prove the existence of sectors of rotations. We estimate the contraction of the global return map and state the constraints on the parameters for ensuring sufficient counterbalance of the expansion. We therefore show that the canard-induced MMOs undergo smooth signature transition, *i.e.* a small oscillation is added without appearance of chaotic dynamics. In the second case, we study the dynamics of the non-linear Integrate-and-Fire system by mean of analyzing an associated discontinuous 1D map. We extend results of the rotation theory and link the rotation numbers to the signature of generated MM(B)O orbits. We stress the partition of the reset parameter space according to the signature.

Chapter 4. We tackle the problematic of complex oscillations synchronization in bilaterally coupled systems and network models. We present a generalization of the GnRH secretion model accounting for two systems bilaterally coupled impacted by the same regulation from a slower dynamics [17]. We show how to reproduce exotic GnRH secretion patterns observed in experimental data and highlight the synchronization/desynchronization process between the two coupled systems occurring in the pulsatility phase. Using two approaches of reduction, we estimate the time of desynchronization according to the parameters. In the subsequent section, we summarize a synchronization study between two identical ICC dynamics, generating MMOs, under the impact of a symmetric coupling [16]. We characterize the 6D model behaviors according to the coupling gain value for both inhibition and excitation cases and the persistence of MMOs in the excitatory case. We prove the frequency decrease when the inhibitory coupling is strengthened. We also present a network model studied in [10] in which all cells reproduce MMO patterns of ICC with individual quantitative features and synchronize episodically – yet periodically – under the influence of a global variable. We use both the analysis of the 3D model of ICC in individual cells and qualitative results on the network dynamics for reproducing the quantitative features and the different types of episodic synchronization observed in experimental data from GnRH neurons.

In the conclusion, we present some perspectives and briefly describe preliminary results of ongoing studies.

Chapter 1

A few models in Neuroscience : complex oscillations and qualitative analysis

At the microscopic level, neurons communicate via spontaneous and rapid variations in membrane potential, called action potential or nerve impulse. Together these electrical phenomena and their related properties have been studied in models, in particular using dynamical system formalism. These models, such as the celebrated model developed by Hodgkin and Huxley [1952], enable us to understand and simulate mechanisms that reproduce neuronal behavior in generating action potential, dendritic integration and axonal propagation. An exciting challenge consists in studying the overall behavior of a neuronal population using either networks of microscopic models (for instance [Stefanescu and Jirsa, 2008]) or macroscopic models based on the organization of cell interactions (for instance [Jansen and Rit, 1995]).

Mathematical analysis of such models provide a key tool for interpreting the electrophysiological data and for revealing the different (patho-)physiological mechanisms that underlie the observed patterns. These models also provide assumptions about the behaviors of the observed system according to parameters that can be interpreted from a biophysical point of view. The choice of the modeling paradigm depends strongly on the tackled problem and the biological question. Yet, due to the intrinsic complexity of neuronal activities, all models capturing the essential features of neuronal mechanisms at a given scale belong to the class of complex systems.

In this chapter, we present a few compact models either well-known or introduced in the context of the studies presented in this thesis. We briefly recall essential properties that are needed for establishing the results summarized in the subsequent chapters.

1.1 Compact models of individual neural cells activity

1.1.1 Integrate-and-fire model

The seminal integrate-and-fire model built by [Lapicque, 1907] is the first attempt to reproduce the sequence of spike emissions by a neuronal cell with a simple dynamics. This hybrid system couples a differential equation describing the dynamics of the cell depolarization, with a discrete dynamics corresponding to the emission of action potentials and the subsequent reset. This formalism has been used during a century for building and studying models reproducing more accurately the underlying mechanisms and the experimental outputs (see for instance [Brette and Gerstner, 2005, Coombes et al., 2012, Izhikevich, 2004, Touboul, 2008]). Among these models, nonlinear bidimensional integrate-and-fire neuron models are simple yet very versatile representations of neuronal dynamics and widely used in applications. When the neural cell is not firing an action potential, these models describe the dynamics of the membrane potential v together with an adaptation variable w as a nonlinear differential equation (sub-threshold dynamics):

$$\dot{v} = F(v) - w + I \tag{1.1a}$$

$$\dot{w} = a(bv - w), \tag{1.1b}$$

where a and b are real parameters accounting respectively for the time constant ratio between the adaptation variable and the membrane potential, and for the coupling strength between these two variables. The real parameter I represents the input current received by the neuron, and F is a real function accounting for the leak and spike initiation currents.

In the following, we assume that F is regular (at least three times continuously differentiable), strictly convex and its derivative admits a negative limit at $-\infty$ and an infinite limit at $+\infty$. Moreover, we assume that F is superquadratic at $+\infty$ (*i.e.* there exists $\eta > 0$ such that F grows faster than $v^{2+\eta}$), so that the membrane potential blows up in finite time and, at this explosion time t^*, the adaptation variable converges to a finite value $w(t^{*-})$. A spike is emitted at time t^* when the membrane potential blows up, *i.e.* $\lim_{t \to t^{*-}} v(t) = +\infty$. Subsequently, the voltage is reset and the adaptation variable updated. Considering spikes as stereotypical electrical impulses $s(t) = \frac{1}{\delta t} U(\frac{t}{\delta t})$ where $U(t)$ is the spike shape rescaled on the dimensionless interval $[0, 1]$, and δt the spike duration, assumed to be small compared to the input integration timescale $0 < \delta t \ll 1/\varepsilon$. The adaptation variable integrates this sharp impulse:

$$w(t^* + \delta t) = w(t^{*-}) e^{-\varepsilon \delta t} + \int_0^{\delta t} b s(t) e^{-\varepsilon(\delta t - s)}\, ds = \gamma w(t^{*-}) + d$$

with $\gamma = e^{-\varepsilon \delta t} < 1$ and $d = b \int_0^1 S(u) e^{-\varepsilon \delta t (1-u)}\, du$. Hence, the reset mechanism is defined as follows:

$$\begin{cases} v(t^*) = v_r, \\ w(t^*) = \gamma w(t^{*-}) + d, \end{cases} \tag{1.2}$$

with $\gamma \leq 1$ and $d \geq 0$ corresponding to the effect on the adaptation variable of a spike emission.

The excitability properties of the system governed by the sub-threshold system (1.1) were investigated exhaustively in [Touboul, 2008]. It was found that all models undergo a saddle-node bifurcation and a Hopf bifurcation, organized around a Bogdanov-Takens bifurcation,

along curves that can be expressed in closed form. An instance of the bifurcation diagram with respect to (I, b) is depicted in Figure 1.1. For (I, b) in region B, the stable manifold of

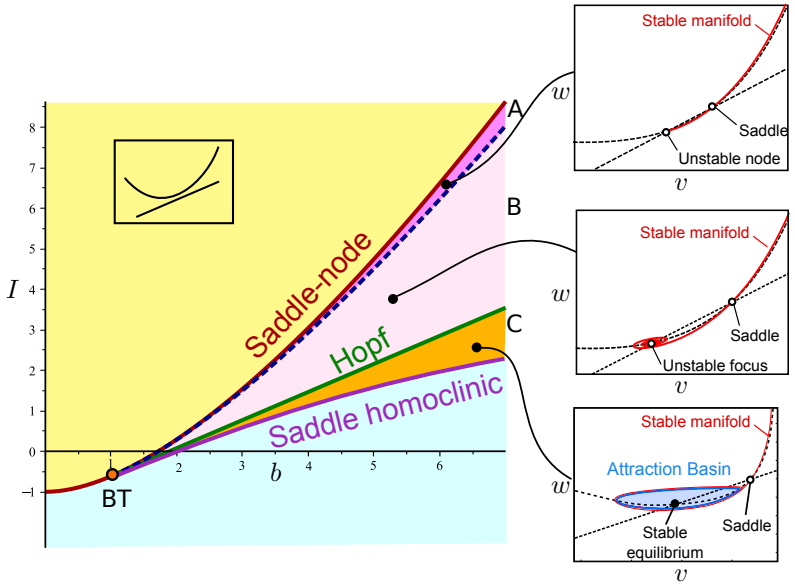

FIGURE 1.1: Bifurcations of the adaptive exponential model and its saddle-node (brown), Hopf (green), saddle homoclinic (purple) and Bogdanov-Takens (BT) bifurcations in the (I, b) parameter plane. The analytical curve separating regions of unstable focus and unstable node is added in dashed blue. Typical phase planes in the different regions of interest are depicted as smaller insets. They feature the nullclines (dashed black) and the stable manifold (red).

the saddle is made in part of a heteroclinic orbit $\mathcal{W}^s_-$ winding around the unstable focus (see Figure 1.2). Hence, if the value of v_r is chosen such that the reset line $v = v_r$ crosses the heteroclinic orbit, typical orbits display Mixed-Mode Oscillations formed by the alternation of small oscillations around the focus (sub-threshold oscillations during the quiescence phase) and subsequent blow-up (corresponding to spike emission). For low enough reset values, several spikes are emitted and train of spikes (bursts) are generated before the next quiescence phase, leading to Mixed-Mode Bursting Oscillations (MMBO).

Hence, even in region B of the bifurcation diagram, the model benefits from a great versatility and can generate a large panel of patterns according to the values of the reset mechanisms v_r, γ and d. In section 3.2, we present the results of a first study of the MM(B)Os signature according to the reset parameter values, by mean of an induced return map (adaptation map) and its rotation properties. Note that the mechanism generating the small oscillations, that can be compared to the one underlying Resonate-and-Fire systems, differs from slow-fast mechanism of canard-induced MMOs.

1.1.2 Fitzhugh-Nagumo model: a paragon model of excitable cell

FitzHugh-Nagumo's system [FitzHugh, 1961, Nagumo et al., 1962] is one of the most famous differentiable system featuring the excitability property. Developed to reproduce a neuron firing rate by a compact dynamics, this slow-fast system has also been widely studied for identifying fine dynamical behaviors, including canard phenomenon first highlighted on a specific case of this dynamics. Several models presented in this thesis are based on this dynamics (extension with a third variable, coupling between oscillators, slow-fast regulation, etc). We only briefly

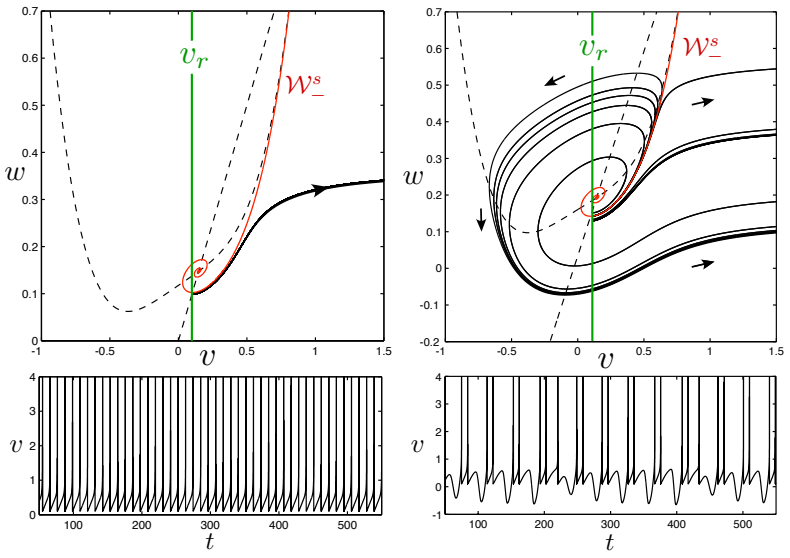

FIGURE 1.2: Instances of orbits and generated signals (regular spiking and MMBO). The dotted lines represent the nullclines of the sub-threshold system.

recall the properties that will be useful for the presentation of the subsequent results and refer the reader to the literature for more details.

We use the following parameterization of the slow-fast FitzHugh-Nagumo dynamics

$$\frac{dX}{d\tau} = -Y + g(X) \tag{1.3a}$$

$$\frac{dY}{d\tau} = \varepsilon\,(b_0 X + b_1 Y + b_2) \tag{1.3b}$$

with $g(X) = -X^3 + 3\nu^2 X$. Classical changes of parameters and variables show that this one-parameter family of cubic functions allows to embed all qualitative and quantitative features of the output obtained with any other cubic function. We assume the timescale separation parameter ε to be small, b_1 small (in a sense defined according to the different contexts) and $b_0 > 0$ (without loss of generality when considering a single system, we assume $b_0 = 1$). In the subsequent models, we will consider either positive and negative values for b_1. In the interpretation of this dynamics as a model of a single neuron activity, X represents the electric activity while the recovery variable Y relies on ionic dynamics. Nevertheless, in the following, we will also use this dynamics as a paragon of excitable system reproducing a fast switch between two states that are transitory stable.

We introduce the classical terminology of slow-fast system analysis. Hence, the cubic critical manifold $Y = g(X)$ consists of singular points of the fast dynamics (1.3a) for the various value of the slow variable Y considered as a parameter. The right fold $P^g_+ = (\nu, 2\nu^3)$ and the left fold $P^g_- = (-\nu, -2\nu^3)$ split the critical manifold into three branches: the left and right branches are attractive for the fast dynamics and the middle branch is repulsive. After the theory of Fenichel [1979], any compact submanifold $\mathcal{M}$ of these branches (that does not contain a fold point) perturbs for ε small enough into an invariant and normally hyperbolic manifold lying in a $O(\varepsilon)$-neighborhood of $\mathcal{M}$ for the Hausdorff distance. Despite such manifold is not uniquely defined, in the case of the left (resp. right) branches, for any ε, a single attractive perturbed manifold

admits an extension by the flow that is asymptotic to the critical manifold for $X \to -\infty$ (resp. $-\infty$): this one is called the left (resp. right) slow manifold.

In the following, we only recall briefly a few results on the bifurcations according to (b_1, b_2, ε) that will be used in the sequel. Therefore, we assume both b_1 and b_2 positive and small enough for the $\dot{Y}$-nullcline to intersect the critical manifold on the middle branch at a repulsive singular point (X_0, Y_0). Two other intersection points lie respectively on the left and right branch. A surface of Hopf bifurcation of (X_0, Y_0) exists in (b_1, b_2, ε) defined for ε small enough

$$\mathcal{H}_p : b_2 = h_p(b_1, \varepsilon) = \nu + 2b_1\nu^3 + O(\varepsilon) \tag{1.4}$$

Such bifurcation happens when the middle singular point (X_0, Y_0) is close to the left fold P^g_- of the critical manifold. The Hopf bifurcation gives birth to a small limit cycle which surrounds the middle singular point (X_0, Y_0) as (ε, b_1, b_2) crosses transversally $\mathcal{H}_p$ to enter the set $b_2 < h_p(b_1, \varepsilon)$. This limit cycle undergoes a Canard explosion as (ε, b_1, b_2) moves away from $\mathcal{H}_p$ and becomes quickly a big relaxation limit cycle (see Figure 1.3-a)

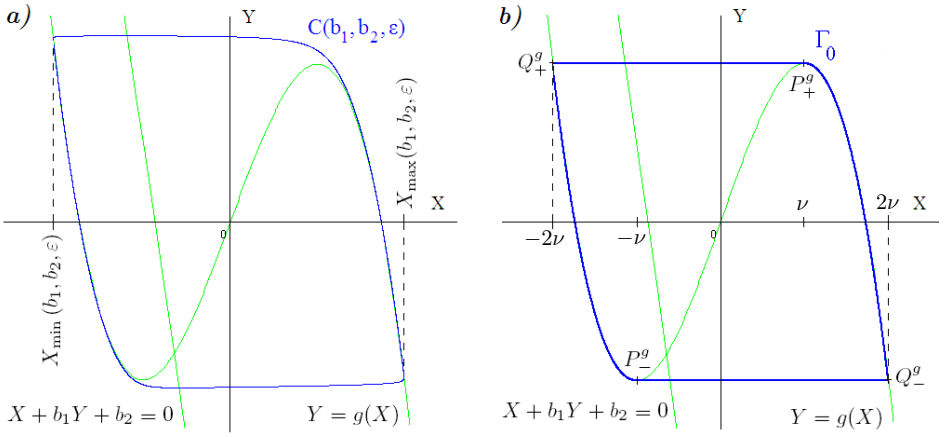

FIGURE 1.3: a) Limit cycle of the Regulating System (RS_ε) for the following parameter values: $b_1 = 0.1$, $b_2 = 1$, $\varepsilon = 0.1$. b) Limit-periodic set Γ_0: limit of the family of genuine limit cycles $(C(b_1, b_2, \varepsilon))_{\varepsilon \in]0;\varepsilon_0]}$ as ε tends to 0 according to the Hausdorff distance.

We introduce the projections of the fold points along the fast fibers on the opposite branch: $Q^f_+ = (-2\lambda, 2\lambda^3), Q^g_+ = (-2\nu, 2\nu^3)$. We can state the following lemma that ensures the existence of a relaxation limit cycle and its asymptotic shape when $\varepsilon \to 0$.

Lemma 1.1. *For each $\alpha > 0$, for all (b_1, b_2) such that $0 \leq b_2 < \min(\nu + 2b_1\nu^3 - \alpha; 2\nu - 2b_1\nu^3)$, there exists $\varepsilon_0 > 0$ such that, for all $\varepsilon \in]0, \varepsilon_0[$, the limit cycle of (RS_ε) exists and contains some points of $[\nu, +\infty[\times\mathbb{R}$. Moreover, for (b_1, b_2) fixed, the limit cycle $C(b_1, b_2, \varepsilon)$ lies in a $O(\varepsilon^{2/3})$-neighborhood of the union Γ_0 of the two branches of the cubic $Y = g(X)$ linking Q^g_+ to P^g_- and Q^g_- to P^g_+, with the segments $[P^g_+, Q^g_+]$ and $[P^g_-, Q^g_-]$.*

Fixing the value of α, we will be interested in the homoclinic bifurcation of the relaxation limit cycle described by the following statement.

Proposition 1.2. *There exists, locally near $\varepsilon = 0$, a $\mathcal{C}^1$-surface of homoclinic connections in the (b_1, b_2, ε)-space given by the graph over $b_1 \in \left]\frac{\nu+\alpha}{4\nu^3}, \frac{1}{\nu^2}\right[$:*

$$\mathcal{H}_c : b_2 = h_c(b_1, \varepsilon) = 2\nu - 2\nu^3 b_1 + O\left(\varepsilon^{2/3}\right).$$

1.1.3 Dynamics of intracellular calcium concentration in neural cell

Models of intracellular calcium concentrations have been proposed in the literature (for instance [Harvey et al., 2011]) with the aim of reproducing a large panel of oscillatory behaviors. Focusing on certain types of neural cells, we have designed a model as compact as possible (three-dimensional) dedicated to reproduce the features observed in the experimental recordings and accounting for the essential mechanisms identified in those cells.

Biological background Detailed investigations in different neural cells (GnRH cells, motoneurons) revealed that the intracellular calcium concentration evolves in an oscillatory manner reflecting the electric activity on a slower timescale and impacting it. This phenomenon is known as Calcium Induced Calcium Release (CICR) (*i.e.* the ability of calcium dynamics through the neuron membrane to activate calcium release from intracellular stores) [Thul et al., 2008]. The most common patterns of variation of calcium level in one neural cell are characterized by the following qualitative features. Each pattern consists of successive peaks characterized by a fast increase followed by a slower decrease to a baseline. Before the subsequent peak, a quiescent phase of a few minutes occurs, as either a jitter near the constant baseline calcium level or a slight and slow increase. We have built a minimal model with one fast and two slow variable embedding CICR dynamical property and able to reproduce the most common pattern of the time-varying intracellular calcium concentration (ICC) [10, 16].

Calcium dynamics We add a third variable Ca to the FitzHugh-Nagumo dynamics standing for the ICC. Its dynamics is built as a slow integration of the electric variable x together with a clearance term, and slow variable Ca acts as a feedback upon the x dynamics. The model, accounting for one fast and two slow variables, reads

$$\dot{x} = (-y + f(x) - \phi_{\text{fall}}(Ca)) \tag{1.5a}$$

$$\dot{y} = \varepsilon k\,(x + a_1 y + a_2) \tag{1.5b}$$

$$\dot{Ca} = \varepsilon\left(\phi_{\text{rise}}(x) - \frac{Ca - Ca_b}{\tau_{Ca}}\right) \tag{1.5c}$$

with

$$f(x) = -x^3 + 3\lambda^2 x, \quad \phi_{\text{fall}}(Ca) = \frac{\mu Ca}{Ca + Ca_d}, \quad \phi_{\text{rise}}(x) = \frac{\lambda_{\text{rise}}}{1 + \exp(-\rho_{Ca}(x - x_{\text{on}}))}. \tag{1.6}$$

Parameter $k > 0$ is of order 1 compared to ε. Parameter Ca_b represents the baseline of the intracellular calcium level. We assume $a_1 < 0$ and small in absolute value so that the y-nullcline is steep, and system (1.5a)-(1.5b) admits a single singular point for any value of Ca. When ϕ_{rise} is inactive ($\phi_{\text{rise}}(x)$ close to 0), Ca reaches a quasi-steady state close to Ca_b. The speed of this motion is determined by the ε/τ_{Ca} ratio, *i.e.* the exponential decay rate. The feedback on x dynamics through the increasing function $\phi_{\text{fall}}(Ca)$ bounded by μ reduces the electric activity of the neuronal population in response to the rise of the calcium concentration. Parameters μ and Ca_d are positive, ensuring that $\phi_{\text{fall}}(Ca)$ is well-defined and positive for all positive values of Ca.

Slow-fast dissection The dynamics features classical properties of slow-fast relaxation systems with one fast and two slow variables. The critical manifold S (or x-nullcline), given by $y = f(x) - \phi_{\text{fall}}(Ca)$, is an S-shaped surface with two fold lines: $\mathcal{F}^-$ at $x = -\lambda$ and $\mathcal{F}^+$ at $x = \lambda$. The fold lines split S into three parts (see Figure 1.4): the left and right sheets contained entirely in the half-spaces $x < 0$ and $x > 0$, respectively, are attracting for the fast dynamics and the middle sheet is repelling. The y-nullcline $a_0x + a_1y + a_2 = 0$ is a plane crossing $\mathcal{F}^-$ for a given value Ca_f of Ca. The Ca-nullcline $Ca = \tau_{Ca}\phi_{\text{rise}}(x) + Ca_b$ is an attractive surface for Ca dynamics. The right hand side of this latter equation is a smooth sigmoidal function of x.

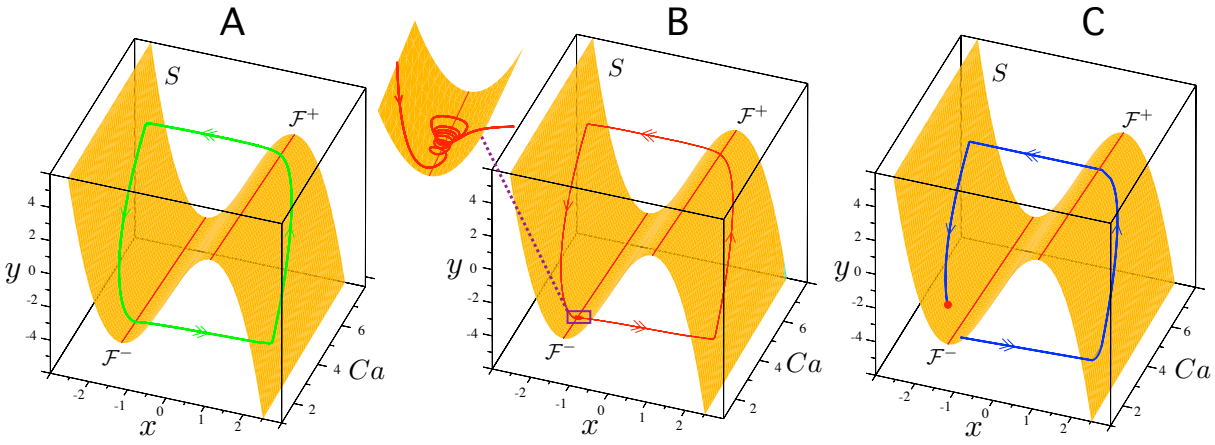

FIGURE 1.4: Different types of system (1.5) orbits according to the value of μ. In each panel, the surface represents the x nullcline S whose folds $\mathcal{F}^{\pm}$ are represented by red lines. Panel A: attractive periodic orbit without small oscillations near the fold $\mathcal{F}^-$. This type of orbit is obtained for small values of μ. Panel B: attractive MMO limit cycle with small oscillations near the fold $\mathcal{F}^-$. This type of orbit is obtained for an interval of μ values. Panel C: orbit that, after a transient excursion in the phase portrait, tends to the attractive singular point of system (1.5) lying on the left sheet of S. This type of orbit is obtained for large value of μ. Panel D is the zoom of the purple box of Panel B and shows a magnified view of the small oscillations of the orbit.

We briefly describe the typical interactions between the state variables, starting from a low level of Ca, close to Ca_b, and initial (x, y) condition such that (x, y, Ca) lies just below $\mathcal{F}^-$. Under the influence of the fast dynamics, the current point (x, y, Ca) quickly reaches the right sheet of S, so that x and $\tau_{Ca}\phi_{\text{rise}}(x)$ quickly increase. Consequently Ca increases while the current point moves up along the right sheet of S towards $\mathcal{F}^+$. Then, once the current point has arrived above $\mathcal{F}^+$, it quickly comes back near the left sheet of S under the influence of the fast dynamics ; variable x quickly decreases as well as the term $\tau_{Ca}\phi_{\text{rise}}(x)$, that becomes almost zero. The current point, driven by the slow dynamics, moves down along the left sheet of S and Ca decreases eventually down to Ca_b. Then, depending on the value of parameter μ, several main situations may occur, illustrated in Figure 1.4.

A: For small values of μ, when the current point reaches the vicinity of $\mathcal{F}^-$, system (1.5a)-(1.5b) is in an oscillatory regime. The current point directly and quickly reaches the right sheet of S, and the behavior described above repeats immediately.

B: For an interval of values of μ, system (1.5a)-(1.5b) is in the excitable regime when Ca approaches Ca_b. Then (x, y) reaches the vicinity of the singular point of (1.5a)-(1.5b) close to the left knee. Ca keeps decreasing until the current point is very close to the attractive

Ca-nullcline and system (1.5a)-(1.5b) enters the oscillatory regime. During this passage, the current point describes small oscillations around the fold $\mathcal{F}^-$ before it undergoes the fast transition to the right sheet and the whole motion repeats. Therefore, the global orbit displays MMOs.

C: For large values of μ, system (1.5a)-(1.5b) remains permanently in the steady regime. Hence, after an excursion in the phase space, the current point reaches and remains in the attractive singular point vicinity. Consequently, the Ca pattern consists of one peak and subsequent return to the baseline.

Each qualitative behavior is identified in experimental data, both in hypothalamic GnRH (gonadotropin releasing hormone) neurons [Richter et al., 2002, Terasawa et al., 1999] and in motoneurons [Fallani et al., 2015]. In section 2.2, we show the ability of this model to generate outputs matching quantitative specifications related to amplitude, pulse and quiescence phase durations (and therefore pulse frequency), and explain the underlying dynamical mechanisms used for defining the parameter estimation process.

It is worth noting that other types of orbits are generated in case B for each transition in the number of small oscillations in the MMO orbit (see [Krupa and Wechselberger, 2010, Szmolyan and Wechselberger, 2001]). Yet in such systems with one fast and two slow variables, it is known that such transition (change in the MMO signature) involves chaotic behaviors. The problematic of parameter estimation to reach given global specifications for this type of oscillations is an open problem to-date. An analysis of the signature change according to the parameter is performed in section 3 on other models, featuring additional properties, namely the Integrate-and-Fire model introduced in section 1.1.1 and the GnRH secretion model described in the next section.

1.2 Mass approach modeling

Neural mass modeling is a part of computational neuroscience that was developed to study the general behavior of neuronal populations. Using this paradigm, the precise features of the individual activities and the microscopic dynamical interactions are no longer taken into account. The state variables of the models are global outputs of neuron assemblies considered to behave jointly, and the parameters involved in the dynamics aggregate several individual parameters. Such mesoscopic model is able to generate output signals that are comparable with experimental data. Moreover, the model dimension is obviously much lower than the dimension of a corresponding network model based on the coupling between individual activities. Therefore, the qualitative analysis remains an accurate tool for studying the fundamental mechanisms underlying the dynamics and for deciphering between different phase portrait structures according to the parameter values.

We present models built for reproducing neuronal activities in two different contexts: the secretion of the neurohormone GnRH (Gonadotrophin Releasing Hormone) by hypothalamic neurons, and the cortical activity resulting from the interactions (mediated by the neurotransmitter concentrations in the extracellular space) between neurons and astrocytes.

1.2.1 Mass approach model of GnRH secretion

Biological background In mammals, the reproductive system is made up of the hypothalamus, belonging to the central nervous system (CNS), the pituitary gland and the gonads (ovaries in females, testes in males). Within the hypothalamus, specific neurons secrete GnRH in a pulsatile manner, which plays a fundamental role in the differential control of the secretion of both LH (Luteinizing Hormone) and FSH (Follicle Stimulating Hormone) by the pituitary gland which, in turn, stimulate differentially the secretion of progesterone (P) and estradiol (E2) by the gonads. The estradiol signal is conveyed to GnRH neurons through a network of interneurons. The balance between stimulatory and inhibitory signals, emanating from the plasmatic level of steroids (estradiol E2 and progesterone P) and relayed by the interneurons, controls the behavior of the GnRH network. This global mechanism and hormone secretion patterns described below are schematized in Figure 1.5.

In females, the pulsatile part of the GnRH pattern is divided into the luteal and follicular phases. The luteal phase is characterized by the secretion of progesterone from the corpus luteum. The follicular phase is characterized by increasing secretion of estradiol. The experimental studies have established that the GnRH pulse frequency not only was greater in the early follicular phase than in the luteal phase, but also increases further within the follicular phase as the surge approaches. Hence, the pulse frequency from the beginning to the end of the pulsatile phase is increased by a factor (about 4 in studied species). The GnRH pulsatile pattern is tremendously altered once per ovarian cycle into a surge which triggers LH surge and ovulation in response to increasing levels of estradiol.

The set of neuronal and glial cells involved in the control of GnRH secretion is commonly known as the "GnRH pulse generator". It includes the GnRH neurons and the regulatory neurons processing the steroids signals and regulating the GnRH neuron activities accordingly. From the beginning of the century, a specific regulatory system, formed by the kisspeptin producing neurons, has been identified as playing a key role in mediating the steroid feedback control of GnRH secretion [Pinilla et al., 2012]. Different subsets of kisspeptin neurons can be associated with hypothalamic areas involved differentially in the ovarian feedback exerted either on the pulse frequency in the pulsatile regime (arcuate nucleus) or on the surge triggering (antero-ventral periventricular nucleus). This differential effect and the sudden change in the type of impact exerted by regulatory neurons on GnRH neurons activity, as well as the cyclicity of the biological system, motivates us to model this impact with an excitable system.

GnRH secretion model A mathematical model accounting for the alternating pulse and surge pattern of GnRH secretion was proposed in [Clément and Françoise, 2007] and further studied in [5, 6, 9, 14]. The model is based on the slow-fast coupling between two FitzHugh-Nagumo systems. We thus consider the following four-dimensional dynamical system with three different timescales:

$$\epsilon\delta\dot{x} = -y + f(x), \tag{1.7a}$$

$$\epsilon\dot{y} = a_0 x + a_1 y + a_2 + cX, \tag{1.7b}$$

$$\epsilon\dot{X} = -Y + g(X), \tag{1.7c}$$

$$\dot{Y} = X + b_1 Y + b_2, \tag{1.7d}$$

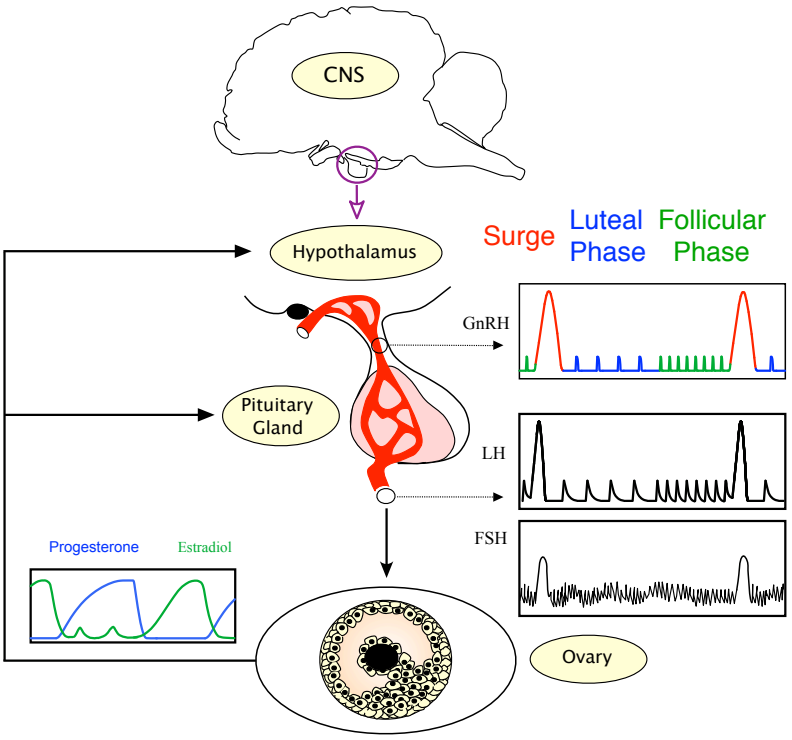

FIGURE 1.5: Scheme of the global feedback loop regulating the GnRH secretion by hypothalamic neurons in mammals. The pulsatile release of GnRH into the hypothalamo-pituitary portal blood induces the pulsatile secretion by the pituitary gland of luteinizing hormone (LH) and follicle-stimulating hormone (FSH) controlling the development of ovarian follicles and their secretory activity. In turn, steroid hormones progesterone and estradiol modulate the secretion of GnRH, LH and FSH. In females, the GnRH secretion pattern dramatically alters once per ovarian cycle, in response to the time-varying levels of ovarian steroids, and switches to the GnRH surge characterized by a massive release of GnRH (red in the corresponding insert).

where a_i, b_i and c are positive parameters (b_0=1) and the timescale separation parameters ε and δ are positive and small. The associated model output is

$$y^{out}(t) = y(t)\chi_{\{y(t)>y_{th}\}}, \tag{1.8}$$

χ_A being the indicator function ($\chi = 1$ on A, 0 elsewhere). In the following, we consider the parameterization

$$f(x) = -x^3 + 3\lambda^2 x, \quad g(X) = -X^3 + 3\nu^2 X.$$

so that the local extrema are $P^f_\pm = (\pm\lambda, \pm 2\lambda^3)$ and $P^g_\pm = (\pm\nu, \pm 2\nu^3)$. The projections of these fold points on the other branch of the cubics $Q^f_\pm$ and $Q^g_\pm$, are easy to compute:

$$Q^f_+ = (-2\lambda, 2\lambda^3), \quad Q^g_+ = (-2\nu, 2\nu^3), \quad Q^f_- = (2\lambda, -2\lambda^3), \quad Q^g_- = (2\nu, -2\nu^3) \tag{1.9}$$

System (1.7a)-(1.7b), named "Secretor", reproduces the average activity of GnRH neurons, while system (1.7c)-(1.7d), named "Regulator", corresponds to the average activity of regulatory neurons. Within this framework, the FitzHugh-Nagumo system is used (twice) for reproducing excitability behaviors of the whole neuronal population, on a variation timescale much slower than the individual neuron activity. Yet, each of them reproduces, using a mass approach, the change in the corresponding subpopulation output, resulting from joint activities of individual

inner cells. The linear coupling between both systems is mediated through the unilateral influence of the slow regulatory interneuron population onto the fast GnRH neuron population, which aggregates the global balance between inhibitory and excitatory neuronal inputs onto the GnRH neurons. We consider the output y^{out} to reproduce the shape of the pulse: a pulse is triggered only if the recovery variable y overcomes threshold y_{th}, fixed once for all.

Underlying dynamical mechanisms and qualitative properties of the output It is convenient to take advantage of the slow-fast coupled structure of the model for a first qualitative description of the different phases that underlie the pattern generation. Under the general assumption (involving parameters b_1 and b_2) that the Regulator admits a relaxation limit cycle, variable X alternates mostly between two states either $X > \nu$ or $X < -\nu$, and switches from one state to another almost instantaneously. This property reflects the estradiol surge-inducing effect on the interneuron network occurring in a low progesterone environment.

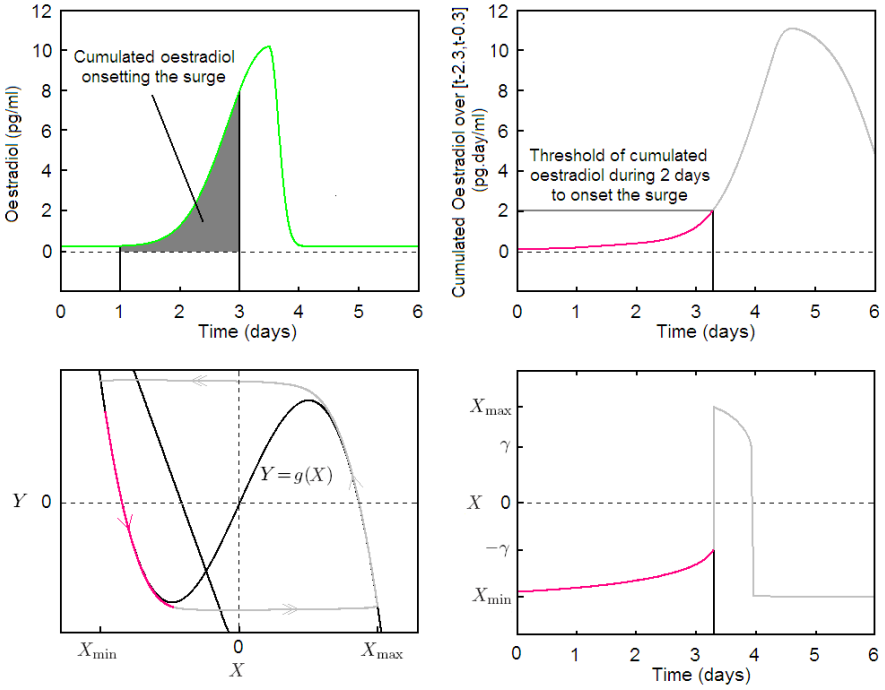

FIGURE 1.6: Dynamical pattern of variable X reflecting the estradiol surge-inducing effect on the interneuron network. Top left panel: schematic temporal changes in estradiol plasma levels (inspired from [Baird et al., 1981]). Top right panel: temporal changes in the estradiol levels cumulated over the sliding window $[t-56\text{h}, t-8\text{h}]$. Bottom panels: limit cycle of the Regulator and dynamical pattern of variable X. The temporal changes in X mimic the cumulated dose of estradiol (pink parts) until the time when the threshold $X = -\nu$ is reached. Beyond $X = -\nu$, the state of variable X changes quasi-instantaneously to $X > \nu$. The threshold corresponds to the cumulated dose of estradiol (in the absence of progesterone) needed to trigger the surge.

The top left panel of Figure 1.6 illustrates the pattern of estradiol plasma levels during the follicular phase. The top right panel shows the estradiol levels cumulated over a two-day sliding window and shifted by a delay that accounts for the time-lag needed to relay the integrated estradiol signal onto GnRH neurons. Considering the two right panels simultaneously enlightens how the dynamical pattern of variable X along the left part of the limit cycle ($X < -\nu$) mimics the cumulated estradiol pattern, until the time when a given threshold is reached (horizontal

black lines hitting the pink curves). The cumulated estradiol threshold corresponds to the (grey) area under the (green) curve on the top left panel of Figure 1.6. The switch of variable X from negative to positive values coincides, on the interneuron network level, with the surge-triggering time.

We now briefly recall the sequential changes undergone by the X-driven Secretor along the limit cycle of the Regulator and reproducing the qualitative properties of the GnRH secretion pattern. The y-nullcline $a_0x + a_1y + a_2 + cX = 0$ is translated according to the value of X and the number of singular points of the Secretor and their positions with respect to the folds of the x-nullcline change with time. Accordingly, the resulting periodic sequence can be divided into 4 phases (Figure 1.7): pulsatile regime, transition from pulsatility to surge, surge, and resumption of pulsatility. During the pulsatile regime, the Secretor admits an unstable singular point on the middle branch of $f(x)$ (between the upper and lower folds) which is surrounded by an attracting relaxation cycle. This cycle disappears through a Hopf bifurcation near the lower fold of the critical manifold in the transition from pulsatile regime to surge. In contrast, in the surge regime, the current point of the Secretor climbs up along the left branch of the critical manifold. In some cases (discussed later in this manuscript), it may follow a stable quasi-stationary point lying on this branch and moving as X changes. The opposite transition from surge to pulsatility phase occurs when the y-nullcline is brought back rightwards. If the rightward motion does not overcome the right fold, the pulsatile regime resumes at once. Otherwise a "pause" with small amplitude oscillations precedes pulsatility resumption, resulting from an MMO mechanism.

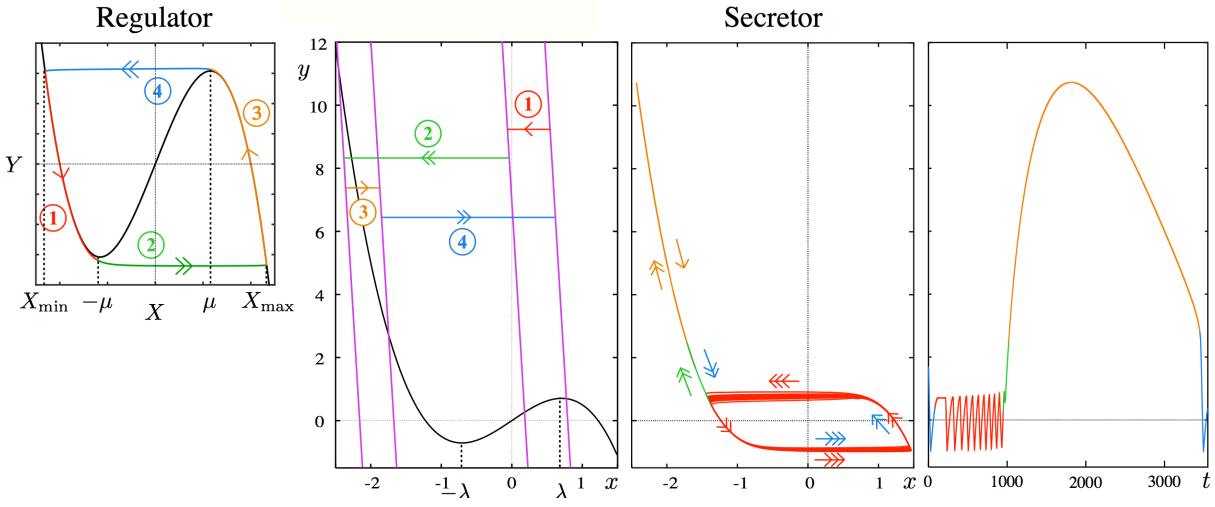

FIGURE 1.7: Decomposition of the Secretor dynamics according to the four phases of the Regulator limit cycle.

One of the salient features of the model is the frequency increase occurring during the pulsatile regime. This increase ensues from the changing location of the unstable stationary point lying on the middle branch of the cubic $f(x)$. At the beginning of the pulsatile regime, this point is close to the upper fold of the cubic. As a consequence, the current point (x, y) running on the limit cycle is slowed down in the vicinity of the stationary point, hence the period of the cycle is rather long (this low frequency pattern corresponds to the so-called luteal phase of the ovarian cycle). As X increases, the y-nullcline moves leftwards, so that the stationary point moves away from the right fold; the current point escapes from the influence of the stationary point and the period gets smaller and smaller, up to the surge triggering (this high frequency

pattern corresponds to the follicular phase of the ovarian cycle). This feature is illustrated by Figure 1.8.

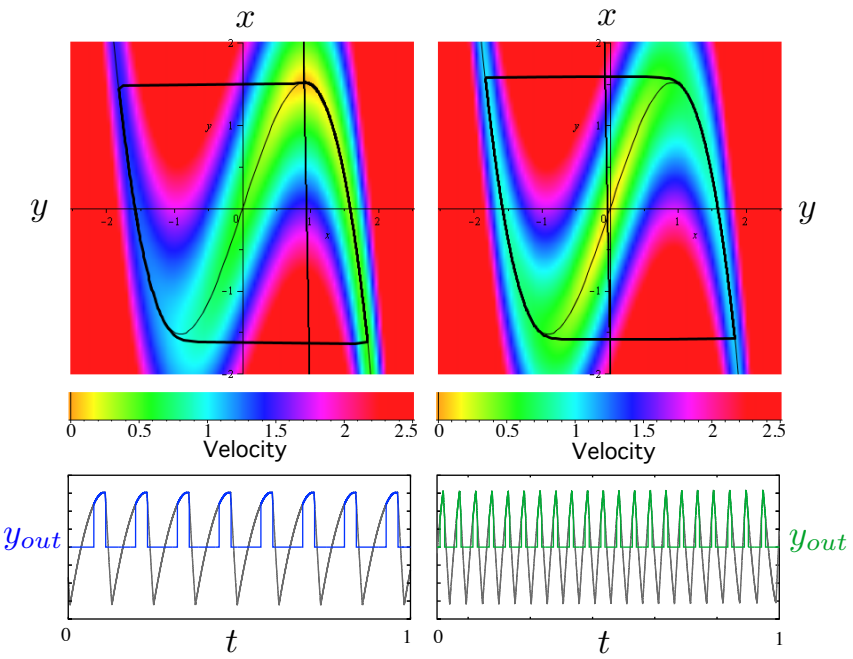

FIGURE 1.8: Magnitude of the vector field associated with the Secretor during the luteal phase (left panel) and at the end of the follicular phase (right panel). The phase plane (x, y) is colored according to the magnitude of the vector field at each point. In the left panel, the singular point lies near the right knee: the weak magnitude of the vector field in the gold neighborhood slows down the dynamics along the limit cycle. In the right panel, the singular point is away from the limit cycle along which the velocity remains medium to high. Consequently, the pulsatile frequency is greater during the follicular phase than during the luteal phase.

In [5], constraints on the parameters were obtained from geometric arguments to guarantee not only the proper qualitative sequence of secretory events, but also quantitative features subject to biological specifications and dealing with the duration, amplitude and frequency of the GnRH signal. These results and the most important methods developed to perform such parameter estimation are presented in section 2.1. In [9], we have performed an in-depth analysis of the pause event guaranteed by a slow passage though a Hopf bifurcation. The most striking result of this analysis consists in the non chaotic transition during the small oscillation adding phenomenon, *i.e.* the existence of an attracting MMO limit cycle even during the signature transition induced by a change in a parameter value. The main steps of this analysis are presented in section 3.1. Furthermore, this 4D model has been recently extended into 6D system by adding a second Secretor interacting with the first one, and subject to the same forcing from the Regulator. This extension, accounting for the clustering of the GnRH neuron network, allows us to reproduce singular patterns of GnRH secretion observed in experimental data (for instance [Caraty et al., 1998, Moenter et al., 1990, 1991]) displaying a double surge (*i.e.* a surge with two "bumps"). A link between the occurrence of such double surge and the subsequent desynchronization between clusters at the end of the pulsatile phase are presented in section 4.1.

1.2.2 Neural mass model with double excitatory feedbacks

The neural mass approach for building model of the cortical activity has been extensively developed since the seminal work of Beurle [1956] and keep being used and studied [Coombes and Byrne, 2016]. Among others, Griffith [1963, 1965] used a neural field formalism and introduced a second order linear differential operator to represent both excitatory and inhibitory interactions between neural cells. Thereafter Wilson and Cowan [1972, 1973] derived the non-linear temporal dynamics for spatially localized neuron populations (voxel) driven the average firing rates associated with a two subpopulation model. Their work popularized the neural mass models using the ODE formalism as an efficient tool for studying the interaction mechanisms at a mesoscopic level. Besides, such models produce output signals, especially local field potentials (LFP), comparable with experimental results such as those produced by electroencephalography (EEG) [Lopes da Silva et al., 1974].

Neural mass models that have been developed mainly involved the dynamical interactions between two neural populations: a main population of pyramidal cells P and a population of inhibitory interneurons I. For a more realistic modeling, some authors have considered a feedback of each subpopulation on itself. In particular for the excitatory feedback of principal cells, two approaches have been considered. On the one hand, a classical way to model this excitatory feedback involving a direct link from the output of principal cells to their input was proposed by Wilson and Cowan [1973] and used by many authors [Liley et al., 2002, Molaee-Ardekani et al., 2010, Robinson et al., 1997]. On the other hand, Jansen and co-workers proposed an indirect track that amounts to considering an intermediary population of pyramidal cells P' interacting with P through synaptic connections [Jansen and Rit, 1995, Jansen et al., 1993]. Interactions between these populations are those introduced by Lopes da Silva et al. [1974, 1976] and the indirect excitatory feedback of pyramidal cells follows the structure studied by Katznelson [1981]. Afterwards, Wendling et al. [2000] applied similar models using indirect excitatory feedback to simulate paroxystic neural activity in the context of partial epilepsies.

From the modeling perspective, we cannot privilege one type of feedback over the other since both couplings are physiologically relevant and can co-exist, a very local one and a more or less distant one. Nevertheless a difference may exist in the range of the local connections considered in these approaches. In practical terms, an indirect feedback induces a delay in the excitatory coupling, which may model a larger neighborhood involved in this feedback. In fact the different couplings studied imply specific underlying dynamics of the model and, therefore, give rise to different panels of behaviors. The emergence of identifiable temporal output features (subthreshold oscillations, epileptic spikes, etc.) can be characterized or predicted by understanding these dynamics.

Therefore, we have embedded both types of excitatory feedbacks in a single neural mass model that we will call NMM in the following [13]. Hence, it includes three feedback loops on population P activity: an inhibitory feedback through the interneuron population I, a direct excitatory feedback of P onto itself (referred to as "direct feedback") and an indirect excitatory feedback (referred to as "indirect feedback") involving the population P' (Figure 1.9(a)). We briefly describe how the dynamics is built in the following paragraph.

The model structure mainly follows the one of Jansen and Rit's model. After the work of Van Rotterdam et al. [1982], the processes converting the average pulse density into excitatory and inhibitory postsynaptic potential are based on the α-functions $h_E(t) = A\,a\,t\,e^{-a\,t}$ and $h_I(t) = B\,b\,t\,e^{-b\,t}$, respectively. Those are Green's functions of the differential operators $\mathcal{F}_E$ and

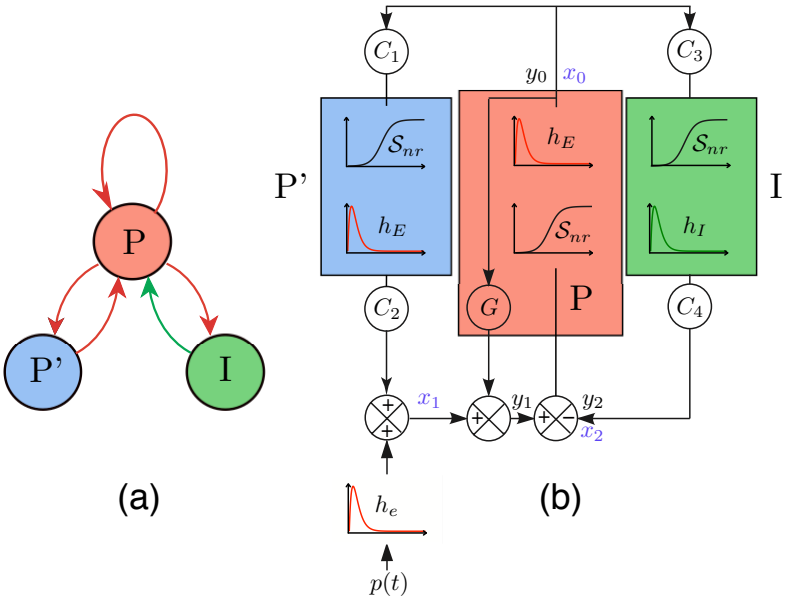

FIGURE 1.9: Two schematic representations of the NMM with double excitatory feedbacks. P: main population of pyramidal cells. I: Interneuron population. P': secondary population of pyramidal cells. Red (resp. green) arrows in (a): excitatory (resp. inhibitory) interactions. Box h_E (resp. h_I): second order process converting action potentials into excitatory (resp. inhibitory) post-synaptic potential. Box $\mathcal{S}_{nr}$: process converting average membrane potential into average action potential density discharge by neurons of populations P, P' and I respectively. C_i for $i \in [\![1, 4]\!]$: coupling gain parameters depending on the maximal number C of synaptic connections between two populations. G: direct feedback coupling gain. $p(t)$: external input. y_0, y_1, y_2: state variables. x_0, x_1, x_2: intermediary variables.

$\mathcal{F}_I$ respectively:

$$\mathcal{F}_E(h_E) = \tfrac{1}{A}\left(\tfrac{1}{a}\, h''_E + 2\, h'_E + a\, h_E\right), \tag{1.10a}$$

$$\mathcal{F}_I(h_I) = \tfrac{1}{B}\left(\tfrac{1}{b}\, h''_I + 2\, h'_I + b\, h_I\right). \tag{1.10b}$$

Parameter A (resp. B) stands for the average excitatory (resp. inhibitory) synaptic gain and tunes the amplitude of excitatory (resp. inhibitory) postsynaptic potentials. Additionally, $1/a$ (resp. $1/b$) represents the time constant of excitatory (resp. inhibitory) postsynaptic potentials representative of the kinetics of synaptic connections and delays introduced by circuitry of the dendritic tree [Freeman, 1975, Jansen et al., 1993, Van Rotterdam et al., 1982]. Following the work of Freeman [1975], the functions converting the average membrane potential into an average pulse density can be approximated by sigmoids. We thus introduce

$$\mathcal{S}(x, x_{\text{th}}, r_{\text{sl}}) = \frac{1}{1 + e^{r_{\text{sl}}\,(x_{\text{th}} - x)}}.$$

Yet, for sake of compactness of the NMM presentation, we introduce an auxiliary parameterization after [Freeman, 1975]:

$$\mathcal{S}_{nr}(x, v) = 2\, e_0\, \mathcal{S}(x, v, r) = \frac{2\, e_0}{1 + e^{r\,(v - x)}}$$

where $2\, e_0$ represents the maximum discharge rate, v the excitability threshold and r the stiffness of neuronal excitability. Finally, the NMM receives an excitatory input $p(t)$ standing for

the action on population P of neural populations in other areas through long-range synaptic connections. This input can be deterministic for representing a specific stimulus. To reproduce a non-specific input and generate realistic model outputs, one classically considers $p(t)$ a gaussian variable.

Parameters $C_i = \alpha_i C$, $i \in \{1, 2, 3, 4\}$, represent the average number of synapses between two populations and weight the coupling modeling the synaptic connections (Figure 1.9(b)). Therefore, parameter C, denoting the maximal number of synapses between two populations, represents the global synaptic coupling strength. The excitation of P by its own output, resulting from the intra-population synaptic connections, is weighted by the coupling gain G. We refer to Table 1 in Appendix for the description and values of all the parameters of the model.

The model writes with the same state variables as the Jansen-Rit model: the excitatory output y_0 and the excitatory y_1 and inhibitory y_2 inputs of the main population P. Hence following the diagram in Figure 1.9(b), one obtains:

$$\ddot{y_0} = A\,a\,\mathcal{S}_{nr}(y_1 - y_2, v_P) - 2\,a\,\dot{y_0} - a^2\,y_0, \tag{1.11a}$$

$$\ddot{y_1} = A\,a\,[C_2\,\mathcal{S}_{nr}(C_1\,y_0, v_{P'}) + G\,\mathcal{S}_{nr}(y_1 - y_2, v_P)] - 2\,a\,\dot{y_1} - a^2\,y_1 + A\,a\,p(t), \tag{1.11b}$$

$$\ddot{y_2} = B\,b\,C_4\,\mathcal{S}_{nr}(C_3\,y_0, v_I) - 2\,b\,\dot{y_2} - b^2\,y_2. \tag{1.11c}$$

We often consider the local field potential (LFP) as the main model output. Following [Jansen et al., 1993], it is defined by $\mathrm{LFP}(t) = y_1(t) - y_2(t)$. It is important to note that, generally, studies of neural mass models only considered the case with the same constant excitability thresholds for all populations, *i.e.*

$$v_P = v_{P'} = v_I = v_0.$$

The panel of this model outputs is very large depending on the values of the parameters and reflect the ability of the model to represent the activity of the different type of voxel (size of the neural populations, structure of the synaptic connections, etc). In [13], we have performed a bifurcation analysis involving parameters $p = p(t)$ (first considered as a parameter), C, α_2 and G for identifying the different types of outputs. The results of this analysis are presented in section 2.3.

1.2.3 Neuron-glia mass model

Biological and computational background Considered as simple energy suppliers for the neurons, the role of the glial cells in the information processing has been neglected for a long time. In the last decade, a specific interest has emerged for the impact of the glial cells activity, in particular astrocytes, upon the neuron behavior. The presence of transporters for GABA and glutamate (the main neurotransmitters of the central nervous system) in both neurons and astrocytes raised the question of the functional importance of the astrocytes in the regulation of the neural activity [Wang and Bordey, 2008]. Henceforth, it has been shown that glial cells and particularly astrocytes have a great impact on both the metabolic regulation [Lee et al., 2011, Sahlender et al., 2014, Schousboe et al., 2013, Volman et al., 2007] and the cerebral blood flow dynamics [Kowianski et al., 2013]. Indeed, the astrocytes activity modulates the dynamics of neurotransmitter concentrations, and consequently the neuronal excitability threshold that depends on the neurotransmitter concentrations in the synaptic cleft, the synaptic transmission

and the neural activity [Araque et al., 1998, 1999, Campbell and Hablitz, 2008, Chever et al., 2016, Losi et al., 2014]. Consequently, astrocytes dysfunctions are involved in several brain pathologies [Losi et al., 2012, Pittenger et al., 2011, Seifert et al., 2006]. Studying the interactions between the neurons and astrocytes cells has therefore become an essential problem in neurophysiology and biophysics. However, there exists no experimental dynamical variations of neurotransmitter concentrations data published in the literature to date.

Several models including these metabolic regulation mechanisms have been proposed in the literature: models of tri-partite synapse [Nadkarni and Jung, 2007, Postnov et al., 2009, 2007, Volman et al., 2012, 2007], models of a single neuron coupled with an astrocyte [De Pittà et al., 2011, Gruetter et al., 2001, Silchenko and Tass, 2008] and sometimes with a hemodynamic compartment [Aubert and Costalat, 2002, 2005, Aubert et al., 2005]. In general, these models are built using conductance-based models of individual neuron activities, and therefore need to scale up for the investigation of the mesoscopic scale. Computational network models of the neuron-glia interactions have also been introduced in [Savin et al., 2009, Volman et al., 2013] to study post-traumatic injury and epileptogenesis respectively. Although those models are useful for comparing *in silico* and *in vivo* data, these network models are hardly mathematically tractable.

Therefore, in [15], we have proposed a neuron-glia mass model built on two bilaterally coupled compartments: the NMM presented in section 1.2.2 generates the neural activity dynamics and the dynamics of neurotransmitter concentrations in the extracellular space involving their uptakes by the local astrocytes.

Neurotransmitter concentrations in the extracellular space The glial compartment is based on the model introduced in [Blanchard et al., 2016] for reproducing the dynamics of GABA and glutamate concentrations (driven by the GABAergic interneurons and glutamatergic pyramidal cells activities) in the extracellular space locally to the main population P. The local nature of this interaction implies that the firing rate of the secondary population P' of pyramidal cells does not impact the glial dynamics associated with the neighboring astrocytes of the main population P. Figure 1.10 illustrates the following mechanism: excited pyramidal cells (resp. interneurons) release glutamate (resp. GABA) in the extracellular space (synaptic cleft). Astrocytes and pre-synaptic neurons reuptake the neurotransmitters. Astrocytes recycle or consume the neurotransmitters while the presynaptic neurons capture them to complete their stock.

The glial compartment is driven by the firing rates of the pyramidal cell and interneuron populations. We introduce the following state variables: (i) J_G^{en} and J_γ^{ei}: the fluxes of glutamate and GABA from neurons to extracellular space, (ii) $[\text{Glu}]_\text{e}$ and $[\text{GABA}]_\text{e}$: the neurotransmitter concentrations in the extracellular space, (iii) $[\text{Glu}]_\text{a}$ and $[\text{GABA}]_\text{a}$: the quantity of neurotransmitters recycled and consumed by the astrocytes. Naturally, the dynamics governing J_G^{en} and J_γ^{ei} are driven by second-order differential operators similar to the synaptic transfer dynamics introduced in (1.10) (see [Molaee-Ardekani et al., 2013, Van Rotterdam et al., 1982]):

$$\begin{aligned}
\mathcal{F}_G(h_G) &= \frac{1}{W}\left(\frac{1}{w_1}\,h_G'' + \frac{w_1+w_2}{w_1}\,h_G' + w_2\,h_G\right),\\
\mathcal{F}_\gamma(h_\gamma) &= \frac{1}{Z}\left(\frac{1}{z_1}\,h_\gamma'' + \frac{z_1+z_2}{z_1}\,h_\gamma' + z_2\,h_\gamma\right).
\end{aligned}$$

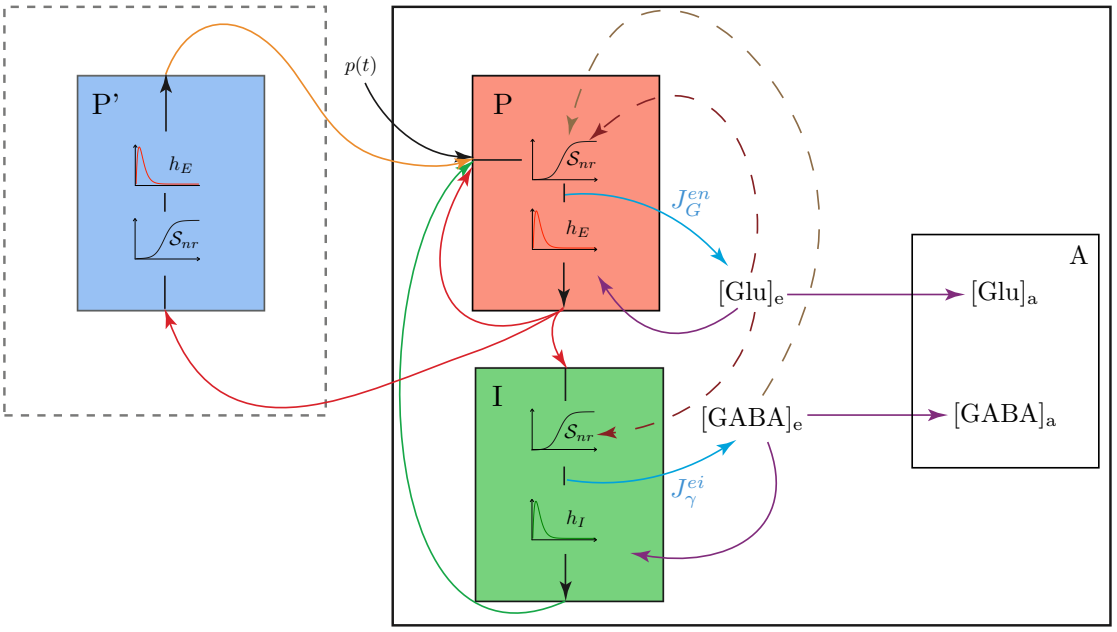

FIGURE 1.10: Neuron-glia model with glial feedback. P and P': main and secondary populations of pyramidal cells. I: interneuron population. $p(t)$: external input on population P. $[\text{Glu}]_e$ and $[\text{GABA}]_e$: glutamate and GABA extracellular concentrations. $[\text{Glu}]_a$ and $[\text{GABA}]_a$: glutamate and GABA glial concentrations. Red arrows: $P \to P$, $P \to I$ and $P \to P'$ couplings. Orange arrow: $P' \to P$ coupling. Green arrow: $I \to P$ coupling. Cyan arrows : glutamate and GABA release by populations P and I into extracellular space (fluxes J_γ^{en} and J_γ^{ei}). Purple arrows: glial and neural reuptakes of neurotransmitters. Red dashed arrows: glutamate feedbacks on populations P and I. Brown dashed arrow: GABA feedback on population P.

As for the synaptic transfer functions, parameter W (resp. Z) tunes the peak amplitude of glutamate (resp. GABA) concentrations and parameters w_1 and w_2 (resp. z_1 and z_2) tune the rise and decay times of glutamate (resp. GABA) release transfer function (see Table 1 in Appendix for the description and values of all the parameters involved in the model). These dynamics are well-suited for reproducing the qualitative and quantitative properties of rise and decay in neurotransmitter concentrations.

The reuptakes of glutamate from the extracellular space by astrocyte and neurons are triggered when extracellular concentration of glutamate reaches a threshold. Moreover, the efficiencies of these processes saturate for high concentration values, which leads to model these dynamics using sigmoidal functions. GABA reuptakes are modeled with Michaelis-Menten dynamics following the experimental literature [Blanchard et al., 2016], using the following function:

$$\mathcal{H}(x,k) = \frac{x}{x+k}$$

The dynamics of the extracellular concentrations ($[\text{Glu}]_e$ and $[\text{GABA}]_e$) are derived from the input (induced by the fluxes J_G^{en} and J_γ^{ei} of neurotransmitters released by the neurons) and output fluxes (induced by the glial and neuronal reuptakes) described above. The astrocyte concentration dynamics ($[\text{Glu}]_a$ and $[\text{GABA}]_a$) result from the glial reuptake ones and a linear consumption term. We introduce parameters V_G^{ae} and V_G^{ne} as the maximal rates of glutamate reuptakes by the astrocytes and the neurons respectively, and V_G^c and V_γ^c as the glutamate and GABA degradation rates in astrocytes.

Following the above explanations, we obtain the dynamics for the glial compartment, where y_0, y_1 and y_2 follow the NMM (1.11):

$$\frac{d^2 J_G^{en}}{dt^2} = W\, w_1\, \mathcal{S}_{nr}(y_1 - y_2, v_P) - (w_1 + w_2)\, \frac{dJ_G^{en}}{dt} - w_1\, w_2\, J_G^{en}, \tag{1.12a}$$

$$\frac{d[\mathrm{Glu}]_\mathrm{e}}{dt} = J_G^{en} - (V_G^{\mathrm{ae}} + V_G^{\mathrm{ne}})\, \mathcal{S}([\mathrm{Glu}]_\mathrm{e}, s_g, r_g), \tag{1.12b}$$

$$\frac{d[\mathrm{Glu}]_\mathrm{a}}{dt} = V_G^{\mathrm{ae}}\, \mathcal{S}([\mathrm{Glu}]_\mathrm{e}, s_g, r_g) - V_G^c\, [\mathrm{Glu}]_\mathrm{a}, \tag{1.12c}$$

$$\frac{d^2 J_\gamma^{ei}}{dt^2} = Z\, z_1\, \mathcal{S}_{nr}(C_3\, y_0, v_I) - (z_1 + z_2)\, \frac{dJ_\gamma^{ei}}{dt} - z_1\, z_2\, J_\gamma^{ei}, \tag{1.12d}$$

$$\frac{d[\mathrm{GABA}]_\mathrm{e}}{dt} = J_\gamma^{ei} - V_\gamma^{\mathrm{ae}}\, \mathcal{H}([\mathrm{GABA}]_\mathrm{e}, K_\gamma^{\mathrm{ea}}) - V_\gamma^{\mathrm{ne}}\, \mathcal{H}([\mathrm{GABA}]_\mathrm{e}, K_\gamma^{\mathrm{en}}), \tag{1.12e}$$

$$\frac{d[\mathrm{GABA}]_\mathrm{a}}{dt} = V_\gamma^{\mathrm{ae}}\, \mathcal{H}([\mathrm{GABA}]_\mathrm{e}, K_\gamma^{\mathrm{ea}}) - V_\gamma^c\, [\mathrm{GABA}]_\mathrm{a}. \tag{1.12f}$$

Modulation of neuron excitability by neurotransmitter concentrations The concentrations of neurotransmitters in a synaptic cleft act on the excitability threshold of the postsynaptic neuron [Araque et al., 1998]. The alteration of this neural excitability threshold can be reproduced in the NMM by dynamical changes in v_P, $v_{P'}$ and v_I. In the following, we describe how we model the modulation of the neuron excitability in each population by the neurotransmitter concentrations in the extracellular space basing ourselves on biological knowledge.

Extracellular concentrations of neurotransmitters have a thresholded impact on neural activity [Araque et al., 1998]. Precisely, on one hand, the impact of neurotransmitter concentrations on neural activity is implicitly taken into account in the neuronal compartment, thus the glial feedback steps in only when the concentrations become larger than physiological ones. On the other hand, the postsynaptic neurons are saturated when these concentrations become to large and, consequently, the neural excitability remains bounded. As explained in the introduction, quantitative experimental data of the impact of neurotransmitter concentrations on neural excitability do not exist up to now. Hence, to reproduce qualitatively the biological mechanisms, we have considered sigmoidal functions to model the glial feedback on neural excitability which is a natural choice for aggregating the qualitative experimental knowledge. It is worth noticing that the qualitative properties are preserved with any bounded increasing functions with a unique inflection point.

We introduce three sigmoidal functions to model the components of the glial feedback:

(a) $m_G^P\, \mathcal{S}([\mathrm{Glu}]_\mathrm{e}, v_G, r_G)$ for the glutamate feedback on pyramidal cells,
(b) $m_G^I\, \mathcal{S}([\mathrm{Glu}]_\mathrm{e}, v_G, r_G)$ for the glutamate feedback on interneurons,
(c) $m_\gamma\, \mathcal{S}([\mathrm{GABA}]_\mathrm{e}, v_\gamma, r_\gamma)$ for the GABA feedback on pyramidal cells.

Note that the fixation mechanisms of glutamate on pyramidal cells and interneurons are the same since the neurotransmitter transporters are independent on the type of neuron [Huang et al., 2004, Pittenger et al., 2011]. Thus, only parameters m_G^P and m_G^I representing the maximal coupling gains of the glutamate-related component of the glial feedback discriminate between the coupling functions $m_G^P\, \mathcal{S}([\mathrm{Glu}]_\mathrm{e}, v_G, r_G)$ and $m_G^I\, \mathcal{S}([\mathrm{Glu}]_\mathrm{e}, v_G, r_G)$, since the synaptic sensitivities may not be the same in pyramidal cells and interneurons.

At the beginning of this section, we evoked that the glial feedback acts on the excitability thresholds of neurons. More specifically, if there is an excess of neurotransmitter in a synapse,

the extracellular concentration of this neurotransmitter acts on the postsynaptic neuron by modulating its excitability threshold. Following the mass approach, we scale this feature to the populations. We build the feedbacks (dotted arrows in Figure 1.10) on the dynamics of the neural compartment, for each type of synaptic connection, using the sigmoidal functions of the neurotransmitter concentrations, basing ourselves on the biological knowledge (*e.g.* [Araque et al., 1998]).

- $P' \to P$ or $P \to P'$. The glial compartment only takes into account neurotransmitters released locally by neurons of populations P and I, whereas population P' is non local to population P. Hence, extracellular concentrations of neurotransmitters in the vicinity of P' have no impact on P and the concentrations in the neighborhood of P and I do not influence postsynaptic neurons of population P'. Consequently, we keep constant $v_{P'} = v_0$.
- $P \to I$. In case of extracellular glutamate excess, the postsynaptic neuron is more excitable. Consequently, more neurons are activated in the population I. We model this mechanism by introducing a dependency of population I excitability threshold and set

$$v_I = v_0 - m_G^I \, \mathcal{S}([\mathrm{Glu}]_\mathrm{e}, v_G, r_G). \tag{1.13}$$

  Note that GABA consumption through "intern" cycles (GABA shunt) is considered as a secondary mechanism compared to the GABA uptake by interneurons [Liang et al., 2006, Patel et al., 2005]. As a consequence, in our model, we decided to neglect the excitability modulation of interneurons by GABA.
- $I \to P$ and $P \to P$. GABA excess strengthens the inhibition of the postsynaptic neuron, *i.e.* less neurons are activated in P. Moreover, a synaptic connection of type $P \to P$ is impacted by the extracellular concentration of glutamate implying a modulation of variable x_0 dynamics as well. In case of an excess of glutamate in a $P \to P$ type synapse, the postsynaptic neuron is more excitable. Gathering both modulations impacting the excitability of population P, we set

$$v_P = v_0 + m_\gamma \, \mathcal{S}([\mathrm{GABA}]_\mathrm{e}, v_\gamma, r_\gamma) - m_G^P \, \mathcal{S}([\mathrm{Glu}]_\mathrm{e}, v_G, r_G). \tag{1.14}$$

The whole neuron-glia mass model is thus obtained by coupling the NMM (1.11) and the glial dynamics (1.12) with the dynamical entries v_I and v_P mentioned above. Consequently, the sigmoidal functions appearing in equations (1.11a), (1.11b), (1.11c), (1.12a) and (1.12d) become

$$\begin{aligned}
\mathcal{S}_{nr}(y_1 - y_2, v_P) &= \frac{2\,e_0}{1 + e^{r\,(v_0 + m_\gamma\,\mathcal{S}([\mathrm{GABA}]_\mathrm{e}, v_\gamma, r_\gamma) - m_G^P\,\mathcal{S}([\mathrm{Glu}]_\mathrm{e}, v_G, r_G) - (y_1 - y_2))}}, \\
\mathcal{S}_{nr}(C_1\,y_0, v_{P'}) &= \frac{2\,e_0}{1 + e^{r\,(v_0 - C_1\,y_0)}}, \\
\mathcal{S}_{nr}(C_3\,y_0, v_I) &= \frac{2\,e_0}{1 + e^{r\,(v_0 - m_G^I\,\mathcal{S}([\mathrm{Glu}]_\mathrm{e}, v_G, r_G) - C_3\,y_0)}}.
\end{aligned}$$

The modulation of the neural activity by the neurotransmitter concentrations has been identified in recent studies as an essential mechanism of several pathologies triggered by glial reuptake deficiencies. In [15], we have performed a model-based study of the link between the glial reuptake deficiency and the neuronal hyperexcitability which is an essential point for understanding the genesis of epileptic behaviors. In section 2.4, we present the main results of this study, based on the analysis of a dynamical bifurcation using constrained optimization tools.

Chapter 2

Bifurcation-based tools for parameter estimation

2.1 GnRH secretion model

2.1.1 Species-dependent specifications of the GnRH secretion pattern

The quantitative features of the GnRH secretion pattern are subject to a huge between-species variability, although the general biological mechanisms are common. Consequently, a fundamental question for properly applying the model to the investigation of the GnRH secretion model introduced in section 1.2.1 has been to develop an efficient way for tuning the parameters of the model so that the outputs fulfill a set of quantitative features. These specifications are

- the ratio between the pulsatility phase and the surge durations,
- the duration of the follicular and luteal phases,
- the ratio between the pulse and surge amplitudes,
- the pulse frequency increase from the beginning to the end of the pulsatile phase.

From the dynamical viewpoint, the challenge is to prove the existence, for any set of quantitative specifications, of a set of parameter values leading to a matching output. Moreover, since a single parameter may impact several features of the generated output, it is important to find the good sequence for fixing the parameters according to each quantitative constraint on the pattern. We have developed an algorithm-like procedure for tuning the parameters detailed in [5] built on the slow-fast properties of the subsystems extracted from the model. The main idea, summarized in the following, is to take advantage of the unilateral coupling between the Regulator (FitzHugh-Nagumo system) and the Secretor (FitzHugh-Nagumo system driven by the Regulator) to identify, for any value of ε small enough, values of (b_1, b_2) leading to a given surge-to-pulsatile phase duration ratio. Then, among these values, one couple leads to the wanted value for the luteal-to-follicular phase duration ratio. Therefore, parameter ε value,

which is critical in the sense that it impacts both amplitudes and durations related features of the outputs as well as the mean pulse frequency, can be chosen together with the other values of the Secretor parameters without taking into account the phase durations. Parameter (b_1, b_2) values can be chosen afterwards for fitting the phase durations.

In the sequel, we summarize the theoretical results on the link between the phase durations and parameters (ε, b_1, b_2) by mean of a foliation of the parameter space. Then, we explain the algorithm-like procedure to tune all the parameters of the GnRH secretion model so that the output fulfills a given quantitative set of specifications. We give two results of this procedure application by mean of reproducing GnRH patterns fulfilling the quantitative specifications of the secretion pattern in the rhesus monkey and the ewe.

2.1.2 Foliation of the Regulator parameter space

Parameter space restriction From the bifurcation results recalled in section 1.1.2, we reduce the (ε, b_1, b_2) parameter space for imposing the existence of a relaxation limit cycle to the Regulator. Hence, along such attractive cycle, the X variable alternatively takes negative and positive values, which discriminates between the pulse phase and the surge of the whole system (1.7). In the sequel, we will only consider (ε, b_1, b_2) values both below the surface $\mathcal{H}_c$ of homoclinic connections, and below and far enough from the Hopf bifurcation surface to avoid any canard phenomenon. With the notations of Lemma 1.1, for ε small enough, the surface of homoclinic bifurcations $\mathcal{H}_c$ is given by $b_2 = h_c(b_1, \varepsilon)$ and the surface of Hopf bifurcation $\mathcal{H}_p$ by $b_2 = h_p(b_1, \varepsilon) = h_p^0(b_1) + O(\varepsilon)$. We introduce a security plane:

$$\mathcal{H}_p^{-\alpha} : b_2 = h_p^0(b_1) - \alpha = \nu + 2b_1\nu^3 - \alpha, \qquad \alpha > 0 \tag{2.1}$$

Thus we consider the new reduced parameter space (see Figure 2.1)

$$(b_1, b_2, \varepsilon) \in \mathcal{R}_1 = \left\{ (b_1, b_2, \varepsilon) \in \mathbb{R}^3_+ \;\middle|\; \begin{array}{l} b_2 < h_p^0(b_1) - \alpha \\ b_2 < h_c(b_1, \varepsilon) \\ \varepsilon < \varepsilon_0 \end{array} \right\}.$$

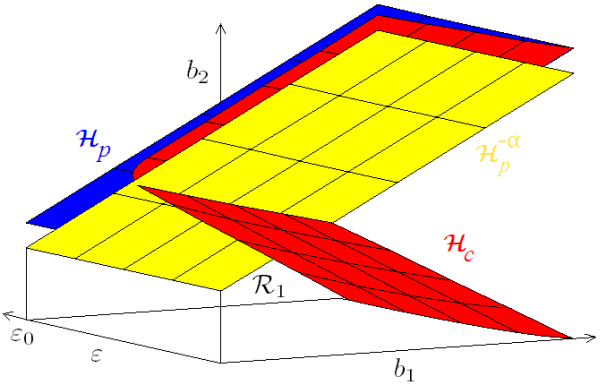

FIGURE 2.1: Bifurcation diagram for $\varepsilon < \varepsilon_0$ and restriction $\mathcal{R}_1$ of the parameter space.

Approximations of pulsatility phase and surge duration Classical results of singular perturbation theory [Dumortier and Roussarie, 1996, Fenichel, 1979, Szmolyan and Wechselberger, 2001] ensures that the left (resp. right) slow part of the limit cycle is exponentially close to the left (resp. right) slow manifold. We note that the perturbed compact slow manifold [Jones, 1995] does not cross the critical manifold and that is can be expressed as a graph over X. Hence, the invariant slow manifold fulfills the following differential equation :

$$\frac{dY}{dX} = \frac{\dot{Y}}{\dot{X}} = \varepsilon \frac{X + b_1 Y + b_2}{-Y + g(X)} < 0 \tag{2.2}$$

By introducing the difference between the left (resp. right) branch of the critical manifold and the corresponding compact slow manifold, we can express integral forms of ε-approximations for the time spent along the limit cycle in $X < 0$ and $X > 0$ respectively. The detailed proof of the following lemma can be found in [5] (Lemma 4.1).

Lemma 2.1. *For $(b_1, b_2, \varepsilon) \in \mathcal{R}_1$, note $(X(t), Y(t))$ a parameterization of the limit cycle $C(b_1, b_2, \varepsilon)$ such that $X(0) = 0$ and $Y(0) > 0$, and $T(b_1, b_2, \varepsilon)$ its period.*
Then, there exists a unique $T_-(b_1, b_2, \varepsilon)$ such that $X(t) < 0$ for $t \in (0, T_-(b_1, b_2, \varepsilon)]$ and $X(t) > 0$ for $t \in [T_-(b_1, b_2, \varepsilon), T(b_1, b_2, \varepsilon)]$. Note $X_{\min}(b_1, b_2, \varepsilon)$ and $X_{\max}(b_1, b_2, \varepsilon))$ the minimal and maximal value respectively taken by X along $C(b_1, b_2, \varepsilon)$, and $T_+(b_1, b_2, \varepsilon) = T(b_1, b_2, \varepsilon) - T_-(b_1, b_2, \varepsilon)$. Then, as ε tends to 0

$$T_-(b_1, b_2, \varepsilon) = \int_{X_{\min}(b_1,b_2,\varepsilon)}^{-\nu} \frac{g'(X) + \frac{\partial \Psi_-}{\partial X}(X, \varepsilon)}{X + b_1 \left(g(X) + \Psi_-(X, \varepsilon)\right) + b_2} dX + O(\varepsilon) \tag{2.3a}$$

$$T_+(b_1, b_2, \varepsilon) = \int_{X_{\max}(b_1,b_2,\varepsilon)}^{\nu} \frac{g'(X) + \frac{\partial \Psi_+}{\partial X}(X, \varepsilon)}{X + b_1 \left(g(X) + \Psi_+(X, \varepsilon)\right) + b_2} dX + O(\varepsilon) \tag{2.3b}$$

where $\Psi_- < 0$ and $\Psi_+ > 0$ are differentiable functions defined on $]X_{\min}(b_1, b_2, \varepsilon), -\nu] \times]0, \varepsilon_0]$ and $[\nu, X_{\max}(b_1, b_2, \varepsilon)[\times]0, \varepsilon_0]$ respectively such that

$$\exists \lambda(\varepsilon) \underset{\varepsilon \to 0}{=} O(\varepsilon^{2/3}), \begin{cases} \forall X \in]X_{\min}(b_1, b_2, \varepsilon), -\nu], |\Psi_-(X, \varepsilon)| < \lambda(\varepsilon) \\ \forall X \in [\nu, X_{\max}(b_1, b_2, \varepsilon)[, |\Psi_+(X, \varepsilon)| < \lambda(\varepsilon) \end{cases} \tag{2.4}$$

Note that the approximations obtained when considering $\varepsilon = 0$ are easier to compute :

$$T_-^0(b_1, b_2) = \int_{-2\nu}^{-\nu} \frac{g'(X)}{X + b_1 g(X) + b_2} dX, \quad T_+^0(b_1, b_2) = \int_{2\nu}^{\nu} \frac{g'(X)}{X + b_1 g(X) + b_2} dX.$$

Note that in application to GnRH secretion pattern, the duration of the pulsatility phase has to be much longer than the surge duration. To do so, the current point (X, Y) has to be confined for a while in the vicinity of the left singular point, which means (b_1, b_2, ε) very close to the surface of homoclinic bifurcations. But, close to $\mathcal{H}_c$, the above approximations are not precise enough for characterizing accurately the value of a large duration ratio between the pulsatility phase and the surge. For this reason, we shall take into account the time spent along the $O(\varepsilon^{2/3})$ path from $X = X_{\min}$ to $X = -2\nu$, even more so since the motion is very slow near the singular point. This remark has motivated the introduction of the ε approximations (2.3). It is worth noticing that this way of calculating durations using implicitly the reduction to the

slow manifold has been extended for a more complex system of two coupled three-dimensional oscillator generating MMOs (see section 4.2.3).

Control of the pulse-to-surge duration ratio Yet, the case $\varepsilon = 0$ is important to ground the subsequent results on the ε-dependent approximations. Hence, we first state the dependence of T_-^0 and T_+^0 on b_1 and b_2 in the following technical lemma. The main property is the possibility, for any b_1 in a precise interval, to choose b_2 so that T_-^0 is as large as we want, while T_+^0 remains bounded.

Lemma 2.2. *1) For all $b_1 \in \left[0, 1/\nu^2\right[$, $b_2 \to T_-^0(b_1, b_2)$ (resp. $b_2 \to T_+^0(b_1, b_2)$) is a $\mathcal{C}^1$ strictly increasing (resp. strictly decreasing) function on $\left[0, \min\left(h_p(b_1) - \alpha, h_c^0(b_1)\right)\right[$*
2) In $\overline{\mathcal{R}_1}$, $T_+^0(b_1, b_2)$ remains finite, while

$$\forall b_1 \in \left[\frac{\nu+\alpha}{4\nu^3}, \frac{1}{\nu^2}\right[, \lim_{b_2 \to 2\nu - 2b_1\nu^3} T_-^0(b_1, b_2) = +\infty$$

3) The function $b_1 \to T_-^0(b_1, h_p(b_1) - \alpha)$ (resp. $b_1 \to T_+^0(b_1, h_p(b_1) - \alpha)$) is $\mathcal{C}^1$ and strictly increasing (resp. strictly decreasing) on $\left[0, \frac{\nu+\alpha}{4\nu^3}\right[$. Moreover:

$$\lim_{b_2 \to 2\nu - 2b_1\nu^3} T_-^0(b_1, h_p(b_1) - \alpha) = +\infty$$

We now prove that we can select the value of b_2 from fixed values of b_1 and ε any ratio $r > 1$ for T_-/T_+, first for $\varepsilon = 0$ in Proposition 2.3, then for any ε small enough using the implicit function theorem in Theorem 2.4.

Proposition 2.3. *There exists a $\mathcal{C}^1$-foliation of $\mathcal{R}_1 \cap \{\varepsilon = 0\}$ of 1-dimensional leaves such that:*
1) for each leaf $\mathcal{F}$, there exists $\bar{b}_1^r \in \left[0, \frac{\nu+\alpha}{4\nu^3}\right[$ such that $\mathcal{F}$ is the graph: $b_2 = l_r^0(b_1)$ of a differentiable function l_r^0 defined on $\left[\bar{b}_1^r, \frac{1}{\nu^2}\right[$,
2) for each $r \geq 1$, there is a unique leaf $\mathcal{F}_r^0$ on which $T_-^0(b_1, b_2)/T_+^0(b_1, b_2) = r$.

Theorem 2.4. *There exists a $\mathcal{C}^1$-foliation of $\mathcal{R}_1$, defined near $\varepsilon = 0$, of two dimensional leaves such that:*
1) each leaf is the graph $b_2 = l_r(b_1, \varepsilon), b_1 \in \left[\bar{b}_1^r, \frac{1}{\nu^2}\right[$ of a differentiable function l_r,
2) for each $r \geq 1$, there exists a unique leaf $\mathcal{F}_r$ on which $T_-(b_1, b_2, \varepsilon)/T_+(b_1, b_2, \varepsilon) = r$.

We have thus proved that, for any prescribed ratio r of the duration of the pulsatility phase to the surge duration, there exists a 2-dimensional manifold of solutions in the parameter space (ε, b_1, b_2), and we have provided a $O(\varepsilon^{2/3})$ approximation of the leaf by the surface:

$$\left\{(\varepsilon, b_1, b_2) \quad | \quad 0 \leq \varepsilon \leq \varepsilon_0, \quad b_2 = l_r^0(b_1), \quad \bar{b}_1^r \leq b_1 \leq \frac{1}{\nu^2}\right\}$$

Starting from this initial guess, a numerical process allows us to reach the precise value of the ratio. We have performed a global simulation for building discretization of several leafs shown in Figure 2.2.

2.1.3 Algorithm for tuning the model parameter

We present the algorithm-like procedure for tuning the parameter values in order to meet the set of quantitative specifications together (the values of parameters λ, ν appearing in functions

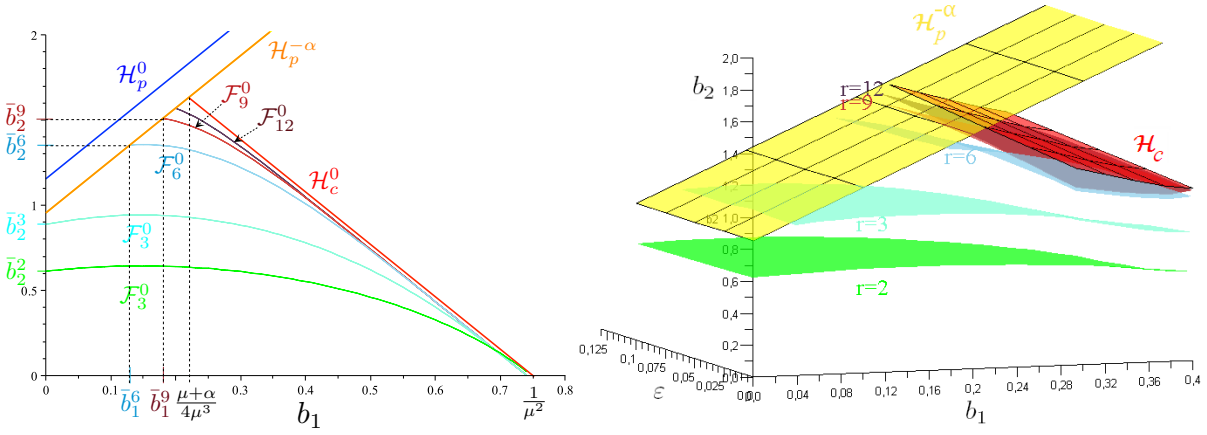

FIGURE 2.2: Left panel : one-dimensional leaves $\mathcal{F}_r^0$, $r = 2, 3, 6, 9, 12$, of the foliation of $\mathcal{R}_1 \cap \{\varepsilon = 0\}$. Each leaf is defined by $T_-^0/T_+^0 = r$. Right panel : two-dimensional leaves in $\mathcal{R}_1$ defined by $T_-/T_+ = r$. This ratio corresponds to the pulsatility phase duration over the surge duration.

f and g as well as δ are chosen once for all). This procedure is detailed in [5]. In particular, we don't recall the constraints on the parameter values, obtained from classical geometric arguments on the nullclines, that ensure the pulse and surge alternation in the generated output.

The procedure first consists in obtaining an initial guess for the parameters values, from the following specification-driven and analysis-based operating sequence:

1. Fix the value of a_2 between λ and $\lambda\sqrt{3}$ so that the $\dot{y}$-nullcline for $X = 0$ separates left fold of the x-nullcline, on its left, from the origin, on its right. The value a_2 is chosen even greater that the prescribed surge amplitude is high.

2. Choose the order of magnitude of ε to fit the average pulse frequency. Combining the whole cycle duration with the average pulse frequency, we can get an approximate number of pulses along a cycle. Since ε is a timescale separation parameter between the Regulator (which drives the whole cycle) and the Secretor (which produces the pulses), it is in the order of the inverse of the pulse number.

3. Tune the value of a_0 to obtain a suitable frequency at the end of the pulsatility phase. Assuming that a_1 is small, we may approximate the minimum period of the GnRH Secreting System, for X ranging between -2ν and $-\nu$, by:

$$T_{min} = 2\varepsilon \int_{-2\lambda}^{-\lambda} \frac{f'(x)}{a_0 x} dx = \frac{\varepsilon}{a_0} \left(9\lambda^2 - 6\ln 2\right) \tag{2.5}$$

   Hence, to obtain a prescribed frequency ϕ at the end of the pulsatility phase, we can link a_0 to ε by $T_{min} = 1/\phi$. The corresponding value of a_0 will impact the pulse to surge amplitude ratio, since the surge amplitude increases exponentially as a_0 decreases.

4. Find the value of c consistent with the pulse frequency ratio ρ between the beginning and the end of the pulsatility phase. With a_2 ranging between λ and $\lambda\sqrt{3}$, the period of the limit cycle of the Secretor for $X = -\nu$ can be approximated by the minimum T_{min}. In that case, the period of the limit cycle for $X = -2\nu$ is equal to T_{min}/ρ. Finding c thus

amounts to solve the implicit equation:

$$\int_{-2\lambda}^{-\lambda} \frac{f'(x)}{a_0 x + a_1 f(x) + a_2 - c\nu} dx + \int_{2\lambda}^{\lambda} \frac{f'(x)}{a_0 x + a_1 f(x) + a_2 - c\nu} dx = \frac{T_{min}}{\rho} \tag{2.6}$$

It is worth noticing that this equation does not admit a solution in c for every value of ρ. The greatest ratio can be reached with the following value of c:

$$c = \frac{a_0\lambda + 2a_1\lambda^3 + a_2}{2\nu} \tag{2.7}$$

5. Define the precise value of a_1. We already assume that a_1 is small enough. The precise choice of a_1 affects marginally the amplitude of the surge, which increases as a_1 increases.

6. Deduce the values of b_1 and b_2 from the results stated in section 2.1.2. For a prescribed duration ratio r between the pulsatility phase and the surge durations, there is a one-dimensional curve of solutions in the (b_1, b_2)-space. Along one such curve of constant ratio, the smaller b_1 is (within the $\left[\bar{b}_1^r, \frac{1}{\nu^2}\right[$ interval), the longer X remains close to $-\nu$, in comparison with the time spent near $X = -2\nu$, hence the sooner the pulse frequency increases. This property is used to set the durations of the luteal and follicular phases.

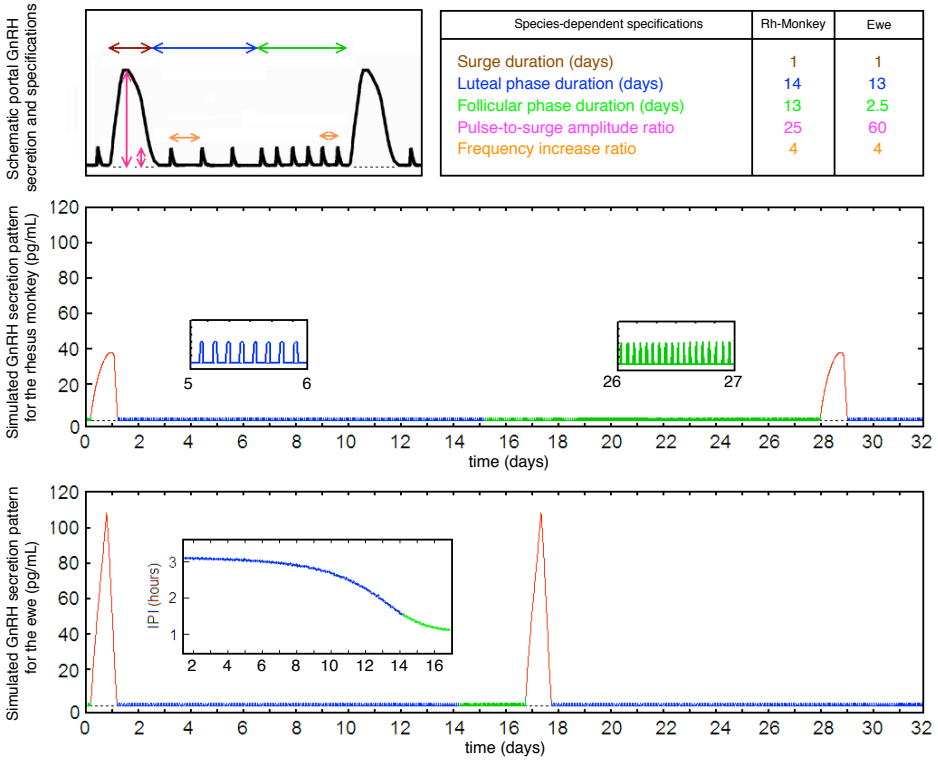

FIGURE 2.3: Outputs of the GnRH Secretion model fulfilling the quantitative features of the GnRH secretion patterns in the rhesus monkey and the ewe respectively. Parameter values have been obtained from the algorithm-like procedure.

From this initial guess, numerical simulations are then performed to improve gradually the compliance with the specifications. More precisely, the values of ε and a_0 are updated from the comparison of the observed generated output with that of the prescribed signal. The value of ε

is updated once (multiplied by the ratio of the prescribed to the observed number of pulses along the cycle). In contrast, since the search for a_0 is a little more heuristic, several trial simulations may be needed before obtaining the expected pulse to surge amplitude ratio. The remaining parameter values are fixed from entering directly step 4 in the sequence described above.

From the general biological knowledge and experimental studies that have been performed on ewes [Moenter et al., 1992, 1990, 1991, Skinner et al., 1997] and rhesus monkey [Catchpole and Wagenen, 1975, Xia et al., 1992], a set of values for the specification can be inferred. Using the parameter tuning process described above, we can find two sets of parameter values for which the GnRH secretion model produce outputs fulfilling the two sets of specification values consistent with the GnRH secretion pattern in the ewe and the rhesus monkey respectively (see Figure 2.3).

2.2 Intracellular calcium oscillations in neurons

In this section, we address the problem of choosing the parameter values of model (1.5) for reproducing oscillatory patterns of ICC in a single cell fulfilling prescribed quantitative features. From experimental studies, we observe that the frequency and amplitudes of the calcium oscillations as well as the baseline in a given cell is often quite close to constant while considerable variability exists between different cells (see for instance [Richter et al., 2002, Terasawa et al., 1999] for GnRH neurons and [Fallani et al., 2015] for motoneurons). In our model, the choice of the baseline value is straightforward by mean of parameter Ca_b. We thus focus on the InterPeak Interval (IPI) and the peak height. As mention in section, a long quiescent phase is reproduced along orbits of the model displaying MMOs. The parameter estimation for such dynamics requires different methods than the one developed in the previous section, although they are based on the application of geometric singular perturbation theory.

Note that, in order to meet the physical timescale in the pattern without changing the parameters of function f involved in the fast dynamics, we have introduced a time rescaling parameter τ (that does not impact the phase portrait of the system). Hence, the ICCM presented in section 1.1.3 becomes:

$$\begin{aligned} \dot{x} &= \tau\left(-y + f(x) - \phi_{\text{fall}}(Ca)\right) && \text{(2.8a)} \\ \dot{y} &= \tau\varepsilon k\left(x + a_1 y + a_2\right) && \text{(2.8b)} \\ \dot{Ca} &= \tau\varepsilon\left(\phi_{\text{rise}}(x) - \frac{Ca - Ca_b}{\tau_{Ca}}\right) && \text{(2.8c)} \end{aligned}$$

with the same functions

$$f(x) = -x^3 + 3\lambda^2 x, \quad \phi_{\text{fall}}(Ca) = \frac{\mu Ca}{Ca + Ca_d}, \quad \phi_{\text{rise}}(x) = \frac{\lambda_{\text{rise}}}{1 + \exp(-\rho_{Ca}(x - x_{\text{on}}))}. \qquad (2.9)$$

2.2.1 Folded singularity and MMOs in the model of intracellular calcium dynamics

The occurrence and the types of MMOs generated by the model are explained by the analysis of the folded singularity [Brøns et al., 2006, Guckenheimer, 2008, Guckenheimer and Meerkamp,

2011, Krupa and Wechselberger, 2010, Szmolyan and Wechselberger, 2001]. After a time rescaling, we can state the system reduced to the critical manifold

$$\begin{aligned} h(x,y,Ca) &= f(x) - \phi_{\text{fall}}(Ca), && \text{(2.10a)} \\ \dot{y} &= l_1(x,y) = x + a_1 y + a_2, && \text{(2.10b)} \\ \dot{Ca} &= l_2(x,Ca) = \phi_{\text{rise}}(x) - \frac{Ca - Ca_b}{\tau_{Ca}}. && \text{(2.10c)} \end{aligned}$$

After projection on the $(x, Ca)-$plane and time rescaling by function $-h_x$, one obtains the desingularized system

$$\begin{aligned} \dot{x} &= h_y l_1 + h_{Ca} l_2, && \text{(2.11a)} \\ \dot{Ca} &= -h_x l_2. && \text{(2.11b)} \end{aligned}$$

The folded singularities are fold points $(\bar{x}, f(\bar{x}, \overline{Ca}), \overline{Ca})$ of the critical manifold such that

$$(h_y l_1 + h_{Ca} l_2)\Big|_{y=f(\bar{x},\overline{Ca})} = 0. \tag{2.12}$$

We recall that the critical manifold has two fold lines $\mathcal{F}^-$ ($x = -\lambda$) and $\mathcal{F}^+$ ($x = \lambda$). Let us consider $\bar{x} = -\lambda$ (one can analyze analogously the case $\bar{x} \in \mathcal{F}^+$). Equation (2.12) for $\bar{x} = -\lambda$ is linear in μ, so for every $\overline{Ca}$ it is possible to find $\mu = \bar{\mu}(\overline{Ca})$ such that $(-\lambda, \overline{Ca})$ is a folded singularity. The linearization of the desingularized system provides the topological type of the singular folds. We can therefore observe the existence of a folded saddle-node bifurcation for a given value of μ. Moreover, it is possible to check that it corresponds to a real equilibrium of the full system, proving that it is a folded saddle-node bifurcation of type II [Guckenheimer, 2008, Guckenheimer and Meerkamp, 2011, Krupa and Wechselberger, 2010].

2.2.2 Parameter tuning of calcium patterns

We mimic the variability of the quantitative features of calcium patterns between different cells by choosing different values for parameters of special importance: μ and k. Parameter k essentially tunes the timescale difference between y and Ca (x being much faster). Hence, an increase in k implies a shorter time for subsystem (2.8a)-(2.8b) to complete a relaxation oscillation and, consequently, a shorter time for Ca to increase and decrease back to the baseline. One can thus increase or decrease the height of the Ca peak by tuning the value of parameter k. Of course, a change in k also implies a change in the duration of the quiescence phase and, consequently, the IPI.

Using the results of the preceding section, we can define the sectors of rotation associated with the folded singularity. Therefore, the precise value of μ prescribes the number of small oscillations of the current point near the left fold $\mathcal{F}^-$ and, consequently, the duration of the quiescent phase. Since variations in μ do not impact much the duration of the peaks, this parameter can be considered to control the IPI. Panel B of Figure 3 shows the results of a change in μ: an increase (resp. decrease) in μ value implies an increase (resp. decrease) in the IPI as shown by the green (resp. blue) pattern compared to the red one in Panel A. The range of variation in μ is limited by the need to produce a quiescent phase between two successive peaks in the Ca pattern.

Finally, the peak height and the IPI can be chosen independently by first tuning the value of k and afterwards the value of μ. Figure 2.4 illustrates the way to fit independently the IPI and the peak amplitude in the Ca output of the model by changing k and μ afterwards.

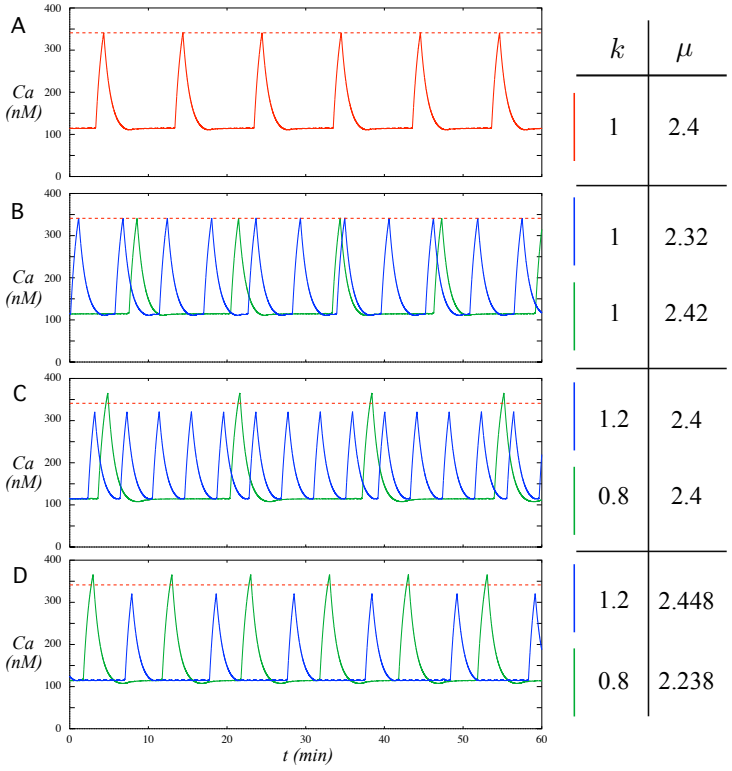

FIGURE 2.4: The values of μ and k corresponding to each colored pattern are given on the right of each panel. Panel A: initial pattern with 10 min IPI and 342 nM peak height. Panel B illustrates the effect of a change in μ on the IPIs. Panel C illustrates the effect of a change in k on both the IPI and the peak height. Panel D shows how to hold the IPI constant (10 min) while changing the peak height.

2.3 Bifurcation analysis of the neural mass model

The neural mass model (1.11) involves, like the GnRH Secretion model, aggregated parameters that can be interpreted at the scale of the populations. Some can be fit according to quantitative experimental data (for instance from EEG and MRI recordings), but others depend on features that can vary according to the context of application, for instance the scale of the populations, the synaptic connectivity in the local area, the possible pathologies. In the study presented in this section, we had a particular interest, in terms of generation of pathological behaviors, on the balanced effects of both excitatory feedbacks which models a fast local feedback versus a delayed neighbor feedback. It is worth noticing that parameters G and α_2 represent the collateral excitations physiologically existing in many brain structures [Frick et al., 2008, Miles and Wong, 1986, Wang et al., 2006]. Increase of local excitatory feedback is prompt to provoke hyperexcitability that may lead to pathological behaviors [Salin et al., 1995], as epileptic discharges [McKinney et al., 1997].

In [13], we have performed a bifurcation analysis according to parameter $p(t) = p$ (considered as a constant), C, α_2 and G. In this analysis, several objects can be defined explicitly or, at least,

expressed as solutions of a simple implicit system of equations. Therefore, we have developed dedicated codes on Matlab® including this theoretical knowledge, which allowed us to perform a more extended analysis (in terms of codimension and size of the parameter space to explore). Nevertheless, parts of the codes were based on general and well-documented numerical methods (in particular numerical continuation) for tracking certain bifurcations involving periodic orbits. The result of this bifurcation analysis allowed us to establish a glossary of identifiable behaviors in the time series underlaid by specific organizations of the NMM bifurcations.

2.3.1 Bifurcation structures with p and time series glossary

To analyze the bifurcations of the NMM, we consider its dynamics presented in section 1.2.2 (system (1.11)) as a system of first order differential equations:

$$\dot{y_0} = y_3, \tag{2.13a}$$
$$\dot{y_1} = y_4, \tag{2.13b}$$
$$\dot{y_2} = y_5, \tag{2.13c}$$
$$\dot{y_3} = A\,a\,\mathcal{S}_{nr}(y_1 - y_2, v_P) - 2\,a\,y_3 - a^2\,y_0, \tag{2.13d}$$
$$\dot{y_4} = A\,a\,[C_2\,\mathcal{S}_{nr}(C_1\,y_0, v_{P'}) + G\,\mathcal{S}_{nr}(y_1 - y_2, v_P)] - 2\,a\,y_4 - a^2\,y_1 + A\,a\,p(t), \tag{2.13e}$$
$$\dot{y_5} = B\,b\,C_4\,\mathcal{S}_{nr}(C_3\,y_0, v_I) - 2\,b\,y_5 - b^2\,y_2. \tag{2.13f}$$

The bifurcation diagram according to $p = p(t)$, assumed to be a constant parameter, traces the evolution of the geometric invariants that organize the dynamics. Basing ourselves on the various possible organizations, we have classified the types of (non trivial) time series (generated this time with a time-varying input $p(t)$) according to their qualitative properties, mostly the changes in the oscillatory pattern. Figure 2.5 displays, for each case, a typical bifurcation diagram (left panel), and an instance of associated LFP time series obtained with $p(t)$ a Gaussian variable and its time-frequency diagram (right panels). We have associated a name, an acronym and a colored flag with each type of time series relying on its fundamental properties.

Note that different diagrams can generate the same type of time series as long as they share essential structural properties. Below we only display one instance of the bifurcation structure associated with one type of generated time series. Yet, the whole set of bifurcation structures leading to the same type of time series can be retrieved from the codimension 2 bifurcation diagrams with respect to C and p displayed in subsequent section 2.3.2.

Noise Modulated Oscillations (NMO). The locus of singular points is a graph over p. Two Hopf bifurcations H_1 and H_2 are linked by a one-dimensional family of limit cycles. For a time-varying input $p(t)$, the generated time series oscillates when $p_{\mathrm{H}_1} < p(t) < p_{\mathrm{H}_2}$ and oscillation amplitude and frequency are modulated by the input value.

Noise Induced Thresholded Amplitude Modulation (NITAM). As in the NMO case, the locus of singular points is a graph over p. The system undergoes 4 Hopf bifurcations at $p_{\mathrm{H}_1} < p_{\mathrm{H}_2} < p_{\mathrm{H}_3} < p_{\mathrm{H}_4}$. The one-parameter family of limit cycles linking H_1 to H_2 admits two folds FLC_1 and FLC_2, while the one linking H_3 to H_4 admits a fold FLC_3. For $p(t)$ a gaussian input, the generated time series alternates between low and high amplitude oscillations due to the presence of stable limit cycles for $p_{\mathrm{FLC}_1} < p(t) < p_{\mathrm{FLC}_2}$ and $p_{\mathrm{FLC}_3} < p(t) < p_{\mathrm{H}_4}$ respectively. Quiescence phases may appear when the point along the orbit follows the stable point for a while.

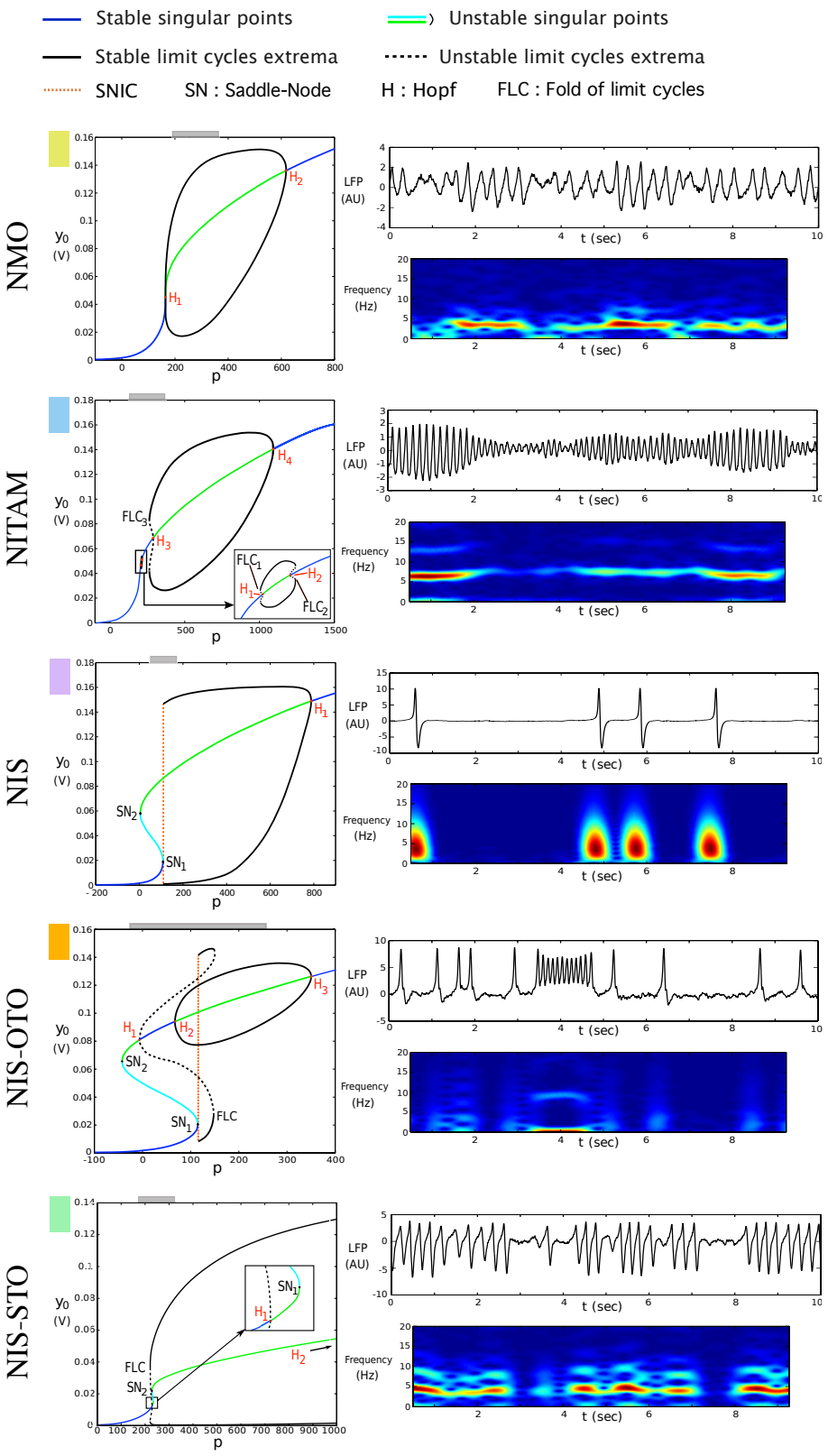

FIGURE 2.5: Bifurcation diagram (left) according to p, instance of LFP time series generated with $p(t)$ a gaussian input and its spectrogram (right). The horizontal grey bar above each diagram represents the confidence interval $[< p > -\sigma, < p > +\sigma]$ of the Gaussian variable used to generate the time series.

Noise Induced Spiking (NIS). The curve of singular points is S-shaped and points SN_1 and SN_2 corresponding to saddle-node bifurcations split it into three branches. A supercritical Hopf bifurcation H_1 on the higher branch creates a stable limit cycle which persists for smaller p values until it disappears through a SNIC bifurcation (Saddle-Node on Invariant Cycle, or saddle-node homoclinic bifurcation) at $p_{\mathrm{SNIC}} = p_{\mathrm{SN}_1}$. For an input $p(t)$ with a mean value close to p_{SN_1}, the system alternates between a stable point on the lower branch and a high-amplitude limit cycle. The period of the cycle is quite large since it is close to the SNIC bifurcation. Hence the generated time series display alternations of spikes and long quiescence phases.

Noise Induced Spiking and Over Threshold Oscillations (NIS-OTO). The locus of singular points is S-shaped as in the NIS case (two saddle nodes SN_1 and SN_2 exist) but three Hopf bifurcations exist on the higher branch: a subcritical one at p_{H_1} and two supercritical ones at p_{H_2} and p_{H_3}. Bifurcation H_1 gives birth to an unstable limit cycle which persists for greater values of p. At p_{FLC}, it disappears through a fold bifurcation of limit cycles with a high-amplitude stable limit cycle. This latter stable cycle exists for p between p_{SN_1}, corresponding to a SNIC bifurcation, and p_{FLC}. Moreover, a family of low amplitude stable limit cycles connects H_2 and H_3. When considering a time varying input $p(t)$, the generated time series alternates high amplitude oscillations (for $p(t) \in]p_{\mathrm{H}_1}, p_{\mathrm{FLC}}[$), low amplitude oscillations for $p(t) \in]p_{\mathrm{H}_2}, p_{\mathrm{H}_3}[$ and quiescence phases.

Noise Induced Spiking and Sub-Threshold Oscillations (NIS-STO).
The set of singular points is split into three branches (lower, middle and higher) by two saddle-node bifurcations SN_1 and SN_2 as in NIS case. A subcritical Hopf bifurcation H_1 exists on the lower branch and a supercritical one on the higher branch. A one-parameter family of limit cycles connects the two Hopf bifurcation points and admits a fold at p_{FLC} (lower than p_{SN_1}) corresponding to a fold bifurcation of limit cycles. With $p(t)$ a gaussian input of mean value close to p_{H_1}, the time series displays an alternation of large oscillations, quiescence phases reflecting the input noise, and sub-threshold oscillations. The large oscillations result from the presence of the stable cycle for $p(t) > p_{\mathrm{FLC}}$. The quiescence phases correspond to periods of time during which the current point is close to lower branch of stable points ($p(t) < p_{\mathrm{H}_1}$). The sub-threshold oscillations occur in the transitions between the two preceding regimes and results from the repulsiveness of the singular point on the lower branch when $p(t) \in]p_{\mathrm{FLC}}, p_{\mathrm{H}_1}[$.
Note that a similar dynamical organization was found by Liley and Walsch [2013] in a mean field model designed to reproduce the burst suppression during anesthesia. This model is able to reproduce small oscillations between high amplitude bursts and burst suppression emerges when adding a slow dynamics driven by the mean field output. Therefore, several physiologically plausible hypotheses arise for explaining the EEG bursting genesis. One of them concerns slow changes of GABA and Glutamate neuro-modulations in activity.

2.3.2 Impact of the balance between direct and indirect feedbacks

Direct and indirect feedbacks have an essential impact on the generated signals resulting in different oscillation profiles. We recall that the indirect feedback gain is defined, in the model, as a proportion $\alpha_2 \in [0, 1]$ of the maximum number C of synaptic connections between populations. Hence, an analysis of the relative effects of direct and indirect feedbacks requires to take into account parameter C in addition to parameters α_2 and G (coupling gain of direct feedback).

For fixed values of α_2 and G, we can identify the different types of time series that the model can generate among those described in the previous section depending on the value of C using the codimension 2 bifurcation diagrams (w.r.t. C and p). By modifying the values of α_2 and G, this diagram changes and so does the panel of possible generated time series.

We have computed the codimension 2 bifurcation diagrams according to C and p and their distribution in the rectangle $(G,\ \alpha_2) \in [0, 80] \times [0, 1]$. We obtain a partition of this rectangle (Figure 2.6) and, for each region representing a scale of direct and indirect feedback gains, a panel of possible behaviors of the NMM. Each region from (a) to (i) is related to a type of codimension 2 diagram according to (C, p) shown in Figure 2.7. We have highlighted the intervals of C values for which the model generates a given type of outputs from those presented in section 2.3.1. Each interval is materialized by a colored vertical band (associated with color flags in Figures 2.5) and the acronym corresponding to the type of related outputs.

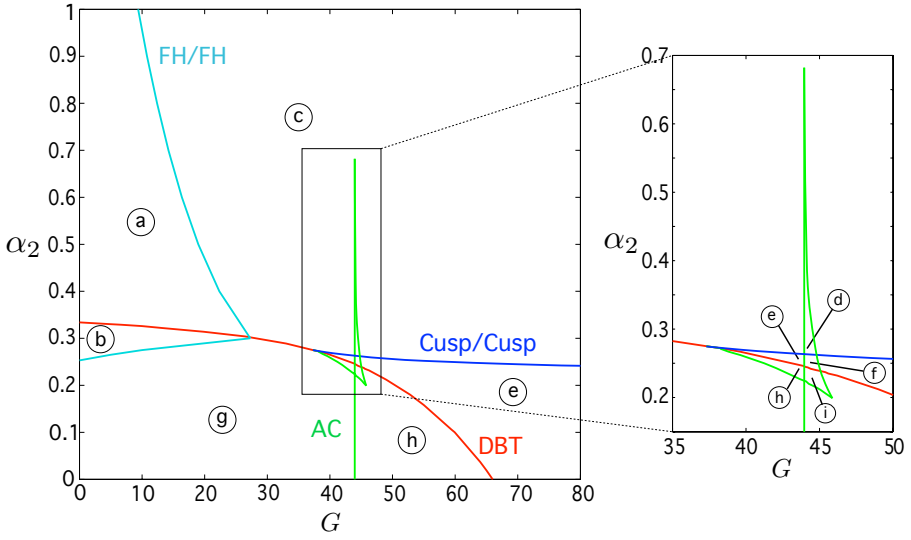

FIGURE 2.6: Partition of the rectangle $[0, 80] \times [0, 1]$ of (G, α_2) values according to the type of bifurcation diagram in (C, p). The right frame is a zoom on the center part of the rectangle. Cyan curve: Appearance/disappearance of two folds of the Hopf branch. Red curve: Degenerated Bogdanov-Takens bifurcation. Blue curve: Cusp-cusp bifurcation. Green curve: Appearance/disappearance of at least one cusp (Cusp_0 or $\text{Cusp}_1/\text{Cusp}_2$ couple). These curves define a partition of the rectangle into 11 regions indexed from (a) to (i): each region is characterized by a structure of the codimension 2 bifurcation diagram in (C, p) shown in the associated panel in Figure 2.7.

We refer to [13] for a detailed description of the codimension 2 bifurcation diagrams. Even if this partition is built by considering the type of time series generated, several transitions between regions correspond to codimension 3 and 4 bifurcations. Indeed, the red curve (separating (a) and (b), (c) and (g), (e) and (h), (f) and (i)) is a degenerate Bogdanov-Takens bifurcation [Baer et al., 2006, Dumortier et al., 1991] occurring with a cusp bifurcation. The intersection between the red curve and the blue curve is a codimension 4 bifurcation in parameters G, α_2, C and p where a degenerate Bogdanov-Takens bifurcation involving a cusp bifurcation coincide with a cusp-cusp bifurcation. Similarly, the intersection point between the red and cyan curves corresponds to simultaneous occurrences of a degenerate Bogdanov-Takens bifurcation and the fusion of two folds of the Hopf bifurcation branch. These two central points in the rectangle partition with values of (G, α_2) primarily organize the time series panel that the system can generate based on the values of the direct and indirect excitatory feedback gains.

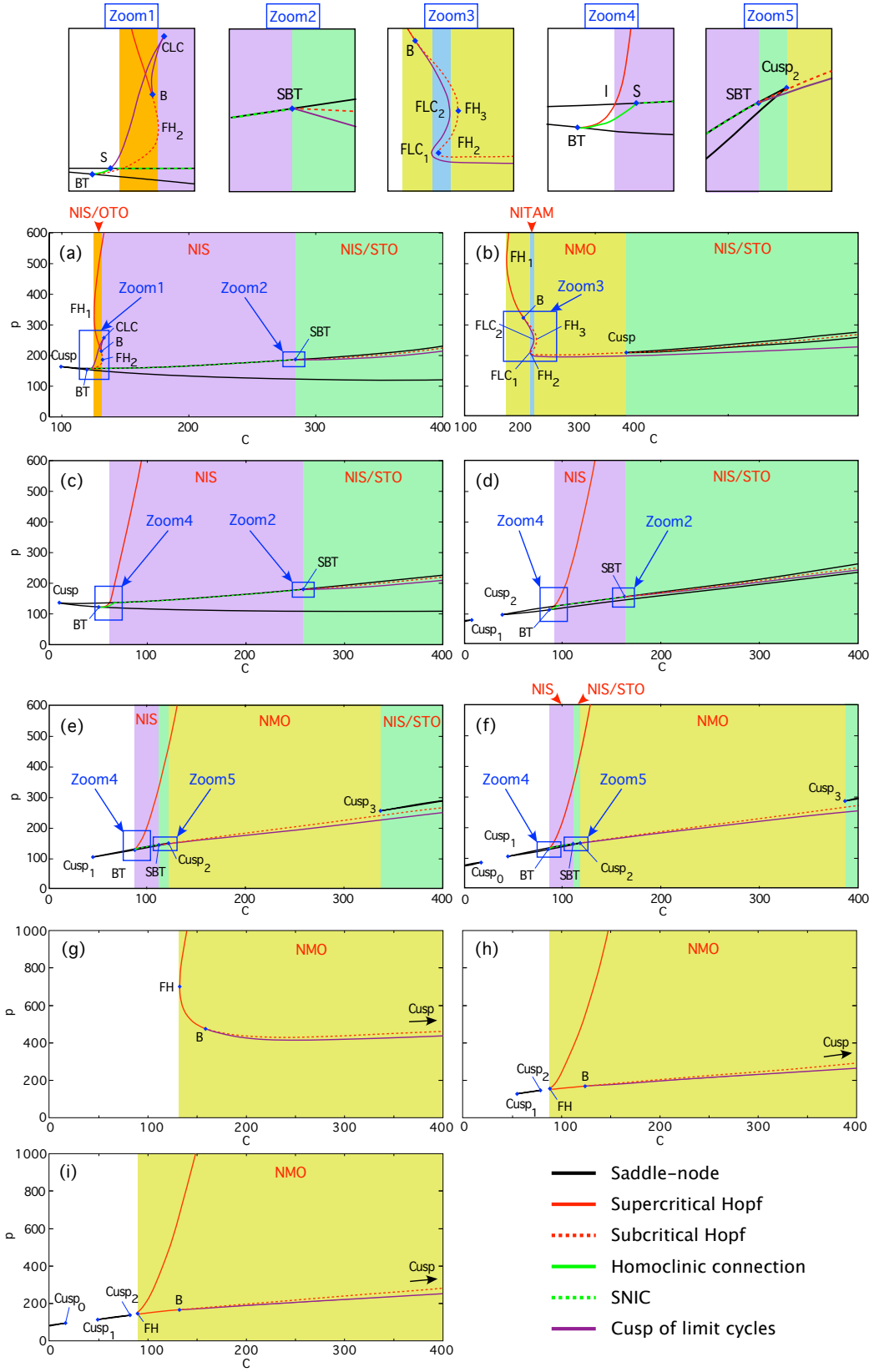

FIGURE 2.7: Structures of the bifurcation diagrams in (C, p) associated with each region (a) to (i) of the (G, α_2) plane partition shown in Figure 2.6. Codimension 2 bifurcations (blue diamonds): Cusp, Bogdanov-Takens (BT), Bogdanov-Takens with SNIC (SBT), Bautin (B), Homoclinic connection to SNIC (S), cusp of limit cycles (CLC). In each diagram, the intervals of C values corresponding to a given type of time series are identified by colored bands and acronyms. Blank intervals correspond to trivial cases.

2.3.3 Estimation of the relative contributions of excitatory feedbacks

Certain types of codimension 2 bifurcation diagrams differ only in the bifurcations that affect trivial cases and, consequently, certain regions of the partition in Figure 2.6 cannot be differentiated by the panel of time series that the system can generate. We have simplified the partition in Figure 2.6 by ignoring the appearances of cusp bifurcations along the green curves and obtain the simplified partition displayed in Figure 2.8. Hence, each new region is characterized by a single panel of time series generated for various values of $C \in [0, 400]$. This panel is identified with a flag composed of the colors related to the types of time series.

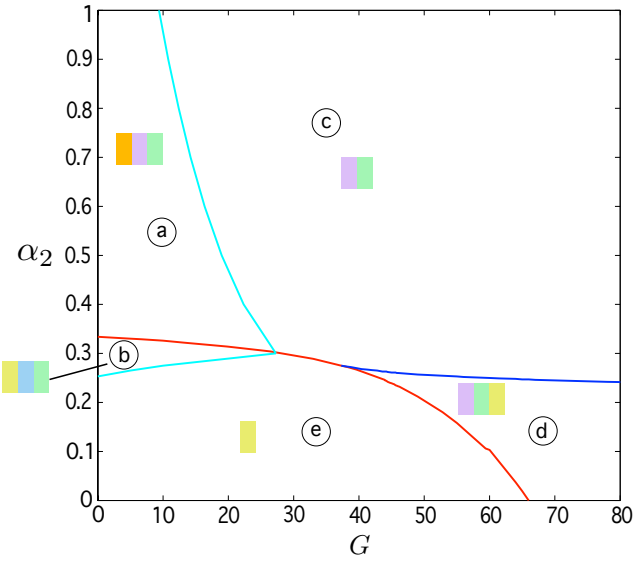

FIGURE 2.8: Partition of parameter (α_2, G) space based on the time series panel that the system can generate for $C \in [0, 400]$. The cyan curve represents the appearance/disappearance of two folds of the Hopf bifurcation branch. The red curve is a branch of degenerate Bogdanov-Takens bifurcations. The blue curve is a branch of cusp/cusp bifurcation. This diagram defines five regions characterized by a single panel of output types: NIS-OTO, NIS, NIS-STO for (a); NMO, NITAM, NIS-STO for (b); NIS, NIS-STO for (c); NIS, NIS-STO, NMO for (e); NMO for (g).

This partition can be used as a tool for inferring the parameter values from the sequential qualitative motifs appearing in experimental time series. A computational process for extracting such information remains to be developed. Yet, we illustrate the impact of a slight change in a parameter values to reproduce the transition from pre-ictal phase to epileptic seizures in experimental data recorded from a Mesial Temporal Lobe Epilepsy (MTLE) mouse model (Figure 2.9 (a)). Using our model, we have generated a time series displaying NIS behavior for $t < 8s$ and NIS-STO behavior afterwards (Figure 2.9 (b)). The transition from NIS case to NIS-STO case is obtained by switching α_2 value (from 0.4 to 0.35) at time $t = 8s$. The spectrograms associated with the model output and the experimental data (Figure 2.9) show that the model output is comparable with the real data in terms of frequency and oscillation amplitudes in each regime.

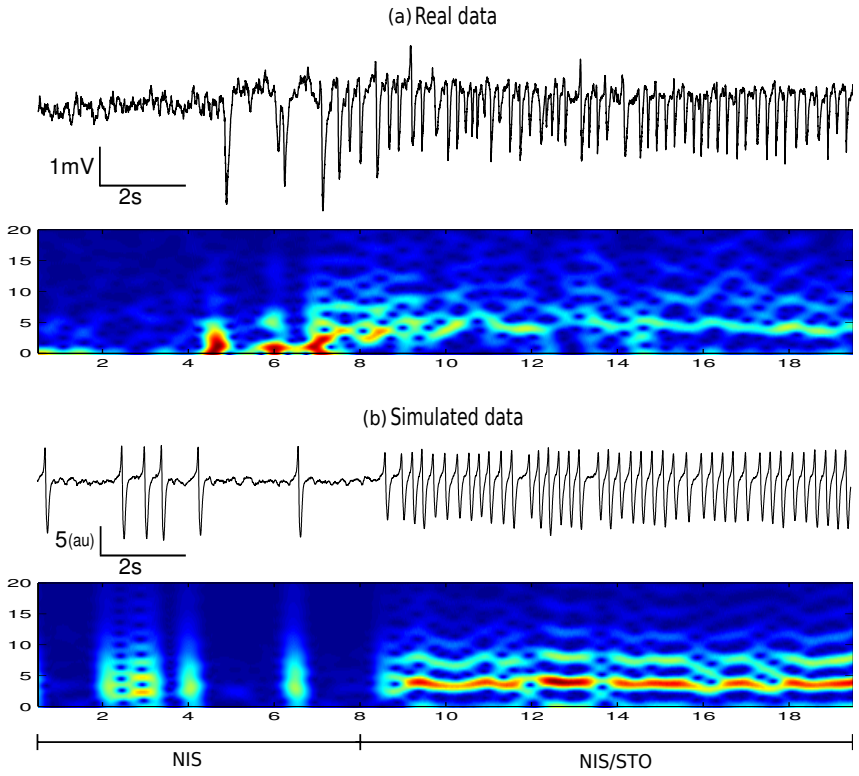

FIGURE 2.9: (a) Experimental LFP time series and associated spectrogram. (b) Model output and associated spectrogram. For $t < 8s$, NIS case ($\alpha_2 = 0.4$) and for $t > 8s$, NIS-STO case ($\alpha_2 = 0.35$).

2.4 Neuron-glia mass model and hyperexcitability

In [Nadkarni and Jung, 2005], the authors have produced numerical evidences of the link between the neuronal hyperexcitability and the neuron-glia interactions at the microscopic scale (individual neuron, interneuron and astrocyte) using the so-called tripartite model. In [15], we have studied this link at the mesoscopic scale using the Neuron-Glia Mass Model (NGMM) presented in section 1.2.3. By coupling arguments from the bifurcation analysis and constrained optimization tools, we have identified both the different types of reaction of the neural compartment in response to astrocyte deficiency and the conditions on the aggregated parameters (related to the neuronal excitability modulation) corresponding to each behavior.

2.4.1 Deficiency in the astrocyte activity

We analyze the impact of the astrocyte deficiency to reuptake neurotransmitters that, consequently, accumulate pathologically in the synaptic cleft. In case of a GABA increase, the post-synaptic neurons receive more inhibition and release less neurotransmitters in the following synapses, we expect a decrease of their activities. A glutamate reuptake deficiency involve more intricate and opposite mechanisms : an increase in the extracellular concentration of glutamate increases post-synaptic neuron excitability. However, interneurons release more GABA implying an increase in the GABA extracellular concentration as well, and an enhancement of the inhibition of the pyramidal activity. Hence, the possible balance between glutamate-induced over-excitation and subsequent GABA-induced over-inhibition may lead to different types of response of the neuronal compartment.

In the model, we can reproduce a reuptake deficiency by decreasing parameter V_γ^{ae} for GABA and V_G^{ae} for glutamate, standing for the maximum rate of each neurotransmitter flux from the extracellular space to the astrocytes, *i.e.* in case of neurotransmitter saturation in the extracellular space. Such changes result in the increase of $[\text{GABA}]_\text{e}$ and $[\text{Glu}]_\text{e}$ respectively. At the neuronal level we are interested in the change in the p_{SNIC} value, standing for the excitability threshold of the NMM, according to the feedback sigmoidal functions. We recall that the fixation mechanisms of glutamate on pyramidal cells and interneurons are the same, which results in the possibility to set

$$\begin{aligned} m_G^I\,\mathcal{S}([\text{Glu}]_\text{e}, v_G, r_G) &\rightarrow v_1, \\ m_G^P\,\mathcal{S}([\text{Glu}]_\text{e}, v_G, r_G) &\rightarrow \frac{m_G^P}{m_G^I}\,v_1, \\ m_\gamma\,\mathcal{S}([\text{GABA}]_\text{e}, v_\gamma, r_\gamma) &\rightarrow v_2. \end{aligned}$$

in the mathematical analysis. The v_1 and v_2 ranges are defined by the limits of $m_G^I\,\mathcal{S}([\text{Glu}]_\text{e}, v_G, r_G)$ and $m_\gamma\,\mathcal{S}([\text{GABA}]_\text{e}, v_\gamma, r_\gamma)$, respectively: $v_1 \in [0, m_G^I]$ and $v_2 \in [0, m_\gamma]$. With these new notations, the dynamical excitability thresholds v_P, $v_{P'}$ and v_I of populations P, P' and I become:

$$\begin{aligned} v_P &= v_0 + v_2 - \frac{m_G^P}{m_G^I}\,v_1, \\ v_{P'} &= v_0, \\ v_I &= v_0 - v_1. \end{aligned}$$

Moreover, the set of singular points obtained for the different values of parameter p can be explicitly expressed according to y_0, v_1 and v_2 all other parameters being fixed:

$$\begin{aligned} p = f(y_0, v_1, v_2) \;=\; & \frac{a}{A}\,(v_0 - \frac{m_G^P}{m_G^I}\,v_1 + v_2) - \frac{a}{A\,r}\ln\left(\frac{2\,A\,e_0 - a\,y_0}{a\,y_0}\right) - \frac{a\,G}{A}\,y_0 \\ & - C_2\,\mathcal{S}_{nr}(C_1\,y_0, v_0) + \frac{a\,B}{b\,A}\,C_4\,\mathcal{S}_{nr}(C_3\,y_0, v_0 - v_1). \end{aligned} \tag{2.14}$$

With these new parameters, an increase or a decrease in GABA (resp. glutamate) extracellular concentration is represented by an increase or a decrease in the value of v_2 (resp. v_1) respectively.

2.4.2 Glial GABA reuptake deficiency

The effect on neural activity of an increase in the extracellular GABA concentration, induced by a deficiency of glial GABA reuptake is characterized by the following

Proposition 2.5. *p_{SNIC} is linear and increasing according to v_2.*

The proof relies on stating the implicit condition defining the saddle-node bifurcation (occurring at the same value of p as the SNIC bifurcation) and using equation (2.14) (see [15]). Hence a deficiency in the glial GABA reuptake implies a decrease in the neural activity. It is worth noticing that the glutamate extracellular concentration remains close to the baseline. Consequently, the impact of the changes in v_1 value can be neglected and, under this approximation, Proposition 2.5 characterizes the global effect of such deficiency on the neural compartment excitability.

We illustrate the application of this proposition by the following simulation. We initialize the NGMM in an oscillatory phase with a low oscillation frequency and consider $p(t)$ a Gaussian input. At $t = 40s$, we turn off the GABA glial reuptake by setting $V_\gamma^{\text{ae}} = 0$ (Figure 2.10). The result is an increase in GABA extracellular concentration implying an increase in p_{SNIC}. As p_{SNIC} increases, the probability for $p(t)$ to overcome p_{SNIC} along the associated brownian motion decreases, and also does the oscillation frequency (Figure 2.10). Consequently, we observe a decrease in the oscillation frequency after $t > 40s$. In the time series, the oscillation frequency decreases gradually during a transient ($40s < t < 60s$) until reaching its minimum. This can be explained by the slow increase of GABA extracellular concentration that reaches its new baseline at $t = 60s$.

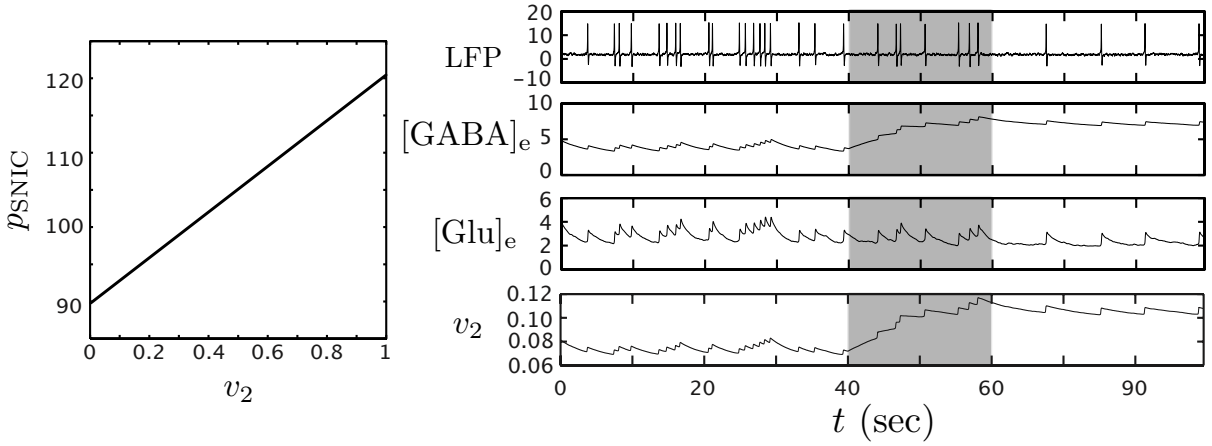

FIGURE 2.10: The dependency of the SNIC value on v_2 explains the impact of an alteration of the GABA glial reuptake on the neural activity. Variation of p_{SNIC} value according to v_2 (left). Time series corresponding to LFP, $[\text{GABA}]_\text{e}$, $[\text{Glu}]_\text{e}$ and $v_2 = m_\gamma \mathcal{S}([\text{GABA}]_\text{e}, v_\gamma, r_\gamma)$ (right from top to bottom) for $p(t)$ a Gaussian variable. At $t = 40$ s, the GABA glial reuptake is artificially altered by setting $V_\gamma^{\text{ae}} = 0$ for any subsequent time. The grey time window highlights the transient towards the new behavior.

2.4.3 Glial glutamate reuptake deficiency

We now consider an increase of the extracellular glutamate concentration that we analyze dynamically by considering changes in v_1 for fixed v_2. We introduce the function

$$g(y_0, v_1) \equiv f(y_0, v_1, v_2)|_{v_2\, fixed}.$$

For each v_1, there exists a unique bifurcation value p_{SNIC} occurring at the non-hyperbolic (saddle-node) singular point characterized by y_{SNIC} which is defined by

$$\frac{\partial g}{\partial y_0}(y_{\text{SNIC}}, v_1) = 0,$$
$$\frac{\partial^2 g}{\partial y_0^2}(y_{\text{SNIC}}, v_1) < 0.$$

This value satisfies $p_{\text{SNIC}} = g(y_{\text{SNIC}}, v_1)$. We cannot find the explicit expressions of $y_{\text{SNIC}}(v_1)$ and $p_{\text{SNIC}}(v_1)$. Thus, for characterizing the variations of p_{SNIC} with v_1, we take advantage of the implicit definitions above and focus on localizing the extrema of $p_{\text{SNIC}}(v_1)$.

Proposition 2.6. *Assume that for any v_1 such that $0 \leq v_1 \leq m_G^I$, p_{SNIC} exists and the associated saddle-node bifurcation is not degenerate. Then*

1. *if $\frac{m_G^P}{m_G^I} \geqslant \frac{B\, e_0\, r\, C_4}{2\, b}$, $p_{\mathrm{SNIC}}(v_1)$ has no local extremum,*
2. *if $0 < \frac{m_G^P}{m_G^I} < \frac{B\, e_0\, r\, C_4}{2\, b}$, $p_{\mathrm{SNIC}}(v_1)$ may admit two local extrema: a minimum at v_1^* and a maximum at v_1^{**}. If both exist, then $v_1^* < v_1^{**}$.*

We stress the idea of the proof based on characterizing the change in the SNIC bifurcation value p_{SNIC} by solving a constrained optimization problem, since it presents a generic feature that can be used in other context involving the dynamical bifurcations, in particular saddle-node bifurcations. The details can be found in [15].

Proof. We search for local extrema of function $p_{\mathrm{SNIC}}(v_1)$ for fixed value of v_2 which is implicitly defined by

$$p_{\mathrm{SNIC}}(v_1) = f(y_0, v_1, v_2), \tag{2.15a}$$
$$\frac{\partial f}{\partial y_0}(y_0, v_1, v_2) = 0, \tag{2.15b}$$
$$\frac{\partial^2 f}{\partial y_0^2}(y_0, v_1, v_2) \leqslant 0. \tag{2.15c}$$

Hence, we are interested in solving the following problem of constrained optimization:

$$\min / \max \left\{ g(y_0, v_1) \quad | \quad \frac{\partial g}{\partial y_0}(y_0, v_1) = 0 \right\}. \tag{2.16}$$

After introducing the associated Lagrangian function, one obtain the necessary condition for the existence of an extremum for g under the constraint $\frac{\partial g}{\partial y_0} = 0$

$$\frac{\partial g}{\partial y_0}(y_0, v_1) - \lambda \frac{\partial^2 g}{\partial y_0^2}(y_0, v_1) = 0, \tag{2.17a}$$
$$\frac{\partial g}{\partial v_1}(y_0, v_1) - \lambda \frac{\partial^2 g}{\partial v_1 \partial y_0}(y_0, v_1) = 0, \tag{2.17b}$$
$$\frac{\partial g}{\partial y_0}(y_0, v_1) = 0. \tag{2.17c}$$

Following the assumption that a non degenerate SNIC bifurcation occurs for any value of v_1 such that $0 \leq v_1 \leq m_G^I$, equation (2.17) admits a solution for any v_1. Hence, if the constrained problem admits an extremum, it corresponds to a SNIC bifurcation occurring at (y_0, v_1) such that

$$\frac{\partial g}{\partial y_0}(y_0, v_1) = 0.$$

From (2.14), for any fixed values of y_0, function $v_1 \to \frac{\partial g}{\partial v_1}(y_0, v_1)$ is bell-shaped and its maximal value does not depend on y_0, one obtains that function $\frac{\partial g}{\partial v_1}(y_0, v_1)$ vanishes in v_1 if

$$0 < \frac{m_G^P}{m_G^I} < \frac{B\, e_0\, r\, C_4}{2\, b}. \tag{2.18}$$

otherwise function $\frac{\partial g}{\partial v_1}(y_0, v_1)$ admits no zero, which proves the first item of the Proposition.

Now, we assume that condition (2.18) is fulfilled. The two values of v_1 satisfying $\frac{\partial g}{\partial v_1}(y_0, v_1) = 0$ can be explicitly calculated using 2.14 and we note them $v_1^* < v_1^{**}$. Note that v_1^* (resp. v_1^{**}) corresponds to the extremum when the saddle-node SN_1 (resp. SN_2) crosses the fold of the surface $g(y_0, v_1) = p$. We consider $v_1 = v_1^*$ and we note y_0^* the value of y_0 corresponding to the SNIC connection for this value of v_1, *i.e.* the solution of

$$\begin{aligned} \frac{\partial g}{\partial y_0}(y_0, v_1^*) &= 0, \\ \frac{\partial^2 g}{\partial y_0^2}(y_0, v_1^*) &< 0. \end{aligned}$$

The bordered Hessian matrix $\overline{H}$ associated with the Lagrangian function at its singular point $(y_0, v_1, \lambda) = (y_0^*, v_1^*, 0)$ reads

$$\overline{H}(y_0^*, v_1^*, 0) = \begin{pmatrix} 0 & \frac{\partial^2 g}{\partial y_0^2} & \frac{\partial^2 g}{\partial v_1 \partial y_0} \\ \frac{\partial^2 g}{\partial y_0^2} & \frac{\partial^2 \mathsf{L}}{\partial y_0^2} & \frac{\partial^2 \mathsf{L}}{\partial v_1 \partial y_0} \\ \frac{\partial^2 g}{\partial v_1 \partial y_0} & \frac{\partial^2 \mathsf{L}}{\partial v_1 \partial y_0} & \frac{\partial^2 \mathsf{L}}{\partial v_1^2} \end{pmatrix}_{|(y_0^*, v_1^*, 0)} = \begin{pmatrix} 0 & \frac{\partial^2 g}{\partial y_0^2} & \frac{\partial^2 g}{\partial v_1 \partial y_0} \\ \frac{\partial^2 g}{\partial y_0^2} & \frac{\partial^2 g}{\partial y_0^2} & \frac{\partial^2 g}{\partial v_1 \partial y_0} \\ \frac{\partial^2 g}{\partial v_1 \partial y_0} & \frac{\partial^2 g}{\partial v_1 \partial y_0} & \frac{\partial^2 g}{\partial v_1^2} \end{pmatrix}_{|(y_0^*, v_1^*, 0)}$$

The determinant of $\overline{H}(y_0^*, v_1^*, 0)$ is given by

$$\det \overline{H}(y_0^*, v_1^*, 0) = -\frac{\partial^2 g}{\partial y_0^2}(y_0^*, v_1^*) \left[\frac{\partial^2 g}{\partial y_0^2}(y_0^*, v_1^*) \frac{\partial^2 g}{\partial v_1^2}(y_0^*, v_1^*) - \left(\frac{\partial^2 g}{\partial v_1 \partial y_0}(y_0^*, v_1^*) \right)^2 \right].$$

On the one hand, the saddle-node associated with the SNIC bifurcation is not degenerate and is a local maximum of $g(y_0, v_1)$, thus $\frac{\partial^2 g}{\partial y_0^2}(y_0^*, v_1^*) < 0$. On the other hand, for any y_0, $v_1 \to \frac{\partial g}{\partial v_1}(y_0, v_1)$ is increasing at (y_0, v_1^*), thus $\frac{\partial^2 g}{\partial v_1^2}(y_0^*, v_1^*) > 0$. Finally $\det \overline{H}(y_0^*, v_1^*, 0) < 0$ and (y_0^*, v_1^*) corresponds to a local minimum of p_{SNIC}. A similar argument proves that (y_0^{**}, v_1^{**}) corresponds to a local maximum of p_{SNIC} (where y_0^{**} is the y_0 value corresponding to SN_2 bifurcation for $v_1 = v_1^{**}$). □

The above proposition can be interpreted as a necessary condition for observing a change in the sense of variations of p_{SNIC} when v_1 varies in $[0, m_G^I]$. Basing ourselves on this result and considering the explicit expression of $\frac{\partial g}{\partial v_1}(y_0, v_1)$, we can derive a necessary and sufficient condition so that v_1^* actually lies in $[0, m_G^I]$: $I_1 \leq \frac{m_G^P}{m_G^I} \leq I_2$, where

$$I_1 = \frac{2\,B\,e_0\,r\,C_4}{b} \frac{e^{r\,(v_0 - C_3\,y_0^*)}}{(1+e^{r\,(v_0 - C_3\,y_0^*)})^2}, \tag{2.19}$$

$$I_2 = \frac{2\,B\,e_0\,r\,C_4}{b} \frac{e^{r\,(v_0 - m_G^I - C_3\,y_0^*)}}{(1+e^{r\,(v_0 - m_G^I - C_3\,y_0^*)})^2}. \tag{2.20}$$

We recall that Proposition 2.5 shows that, for a fixed value of v_1, p_{SNIC} is linear and increasing with v_2. Both results allow us to predict that there exist three shapes of $p_{\text{SNIC}}(v_1, v_2)$ according to the value of $\frac{m_G^P}{m_G^I}$.

(a) If $\frac{m_G^P}{m_G^I} < I_1$ then $v_1^* < 0$ and p_{SNIC} strictly increases with v_1 and v_2.

(b) If $\frac{m_G^P}{m_G^I} > I_2$, then $v_1^* > m_G^I$ and p_{SNIC} strictly decreases when v_1 increases (for v_2 fixed) and strictly increases with v_2 (for v_1 fixed).

(c) If $I_1 \leq \frac{m_G^P}{m_G^I} \leq I_2$, then $0 \leq v_1^* \leq m_G^I$ and p_{SNIC} decreases when v_1 increases in $[0, v_1^*]$ and increases with $v_1 > v_1^*$ (for v_2 fixed).

Figure 2.11 illustrates the three qualitative types of neural activity resulting from an alteration of the glutamate reuptake by the astrocytes: we provide simulations representing the value of p_{SNIC} in (v_1, v_2) space and time series generated by the model.

Biological interpretation The intermediate case discussed above in case of glial glutamate reuptake deficiency (transient hyperexcitability) highlights the possible regulation of an excess of glutamate extracellular concentration after a delay, triggering a decrease of neural activity after the initial increase. Moreover, the frequency after the regulation delay can be greater or lower than the initial one, depending on the value of the ratio $\frac{m_G^P}{m_G^I}$. Note that this value can be tuned to obtain v_1^* small enough and p_{SNIC} large enough so that the frequency after regulation is equal or lower than the one before reuptake deficiency. This property offers the possibility of fitting the model outputs to experimental data and allows us to propose hypotheses about physiological and pathological mechanisms. In particular, this study is a proof of concept of the importance of the balance between the glutamate-induced excitability modulation on the pyramidal cells and the interneurons. This balance would be necessary for the physiological neuro-glial system to benefit from a resilience property in case of lowered astrocyte activity. Otherwise, either the hyperexcitability may degenerate in a crisis or the neural activity diminishes pathologically.

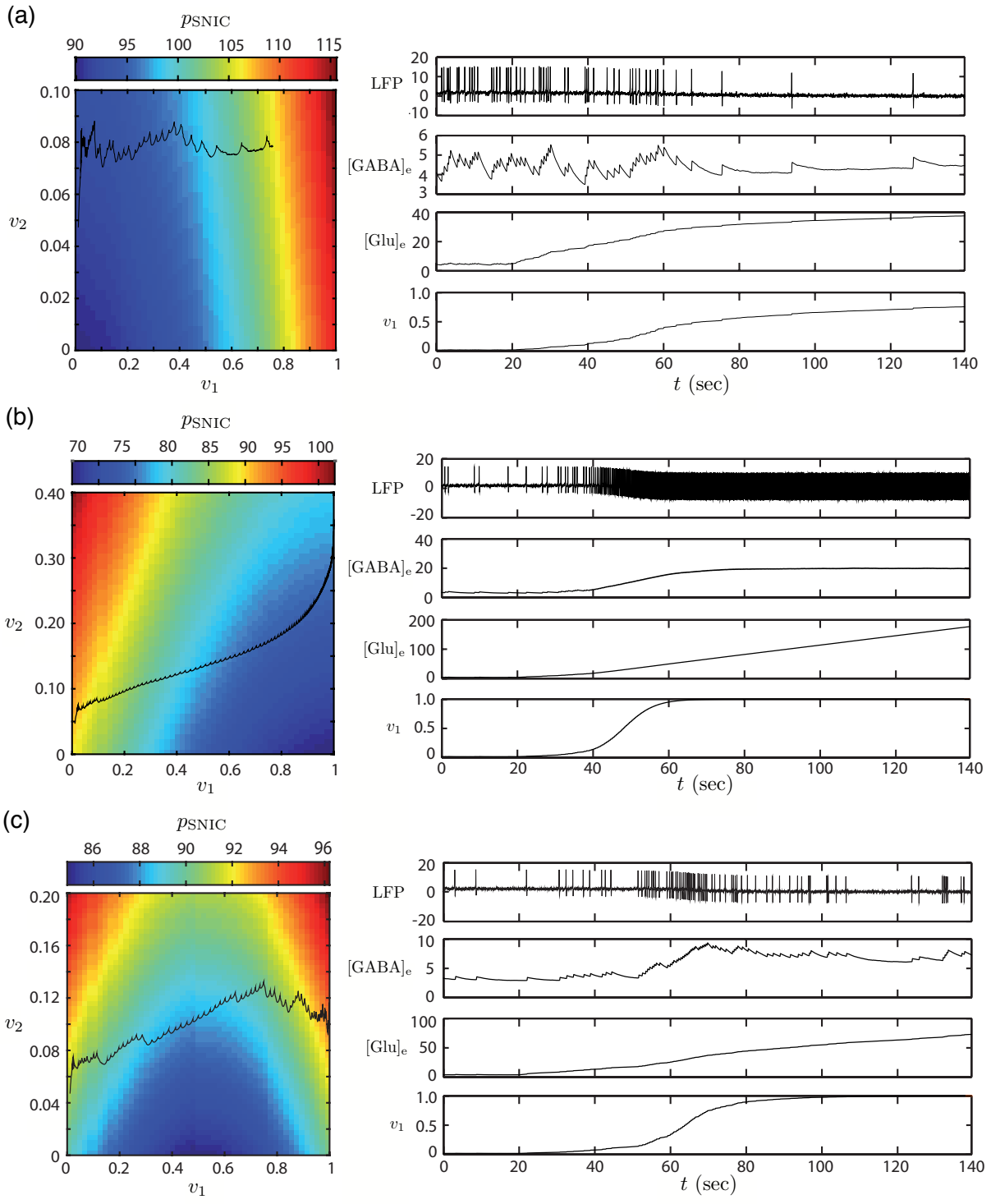

FIGURE 2.11: Alteration of glial glutamate reuptake (a) lessening the excitability, (b) resulting in sustained hyperexcitability, (c) resulting in transient hyperexcitability. In each case, the colormaps on the left display the values of p_{SNIC} in (v_1, v_2) plane, and the time series on the right correspond to LFP, $[\mathrm{GABA}]_e$, $[\mathrm{Glu}]_e$ and $v_1 = m_G^I \mathcal{S}([\mathrm{Glu}]_e, v_G, r_G)$. The black curves on the colormaps are the traces of $(m_G^I \mathcal{S}([\mathrm{Glu}]_e, v_G, r_G),\ m_\gamma \mathcal{S}([\mathrm{GABA}]_e, v_\gamma, r_\gamma))$ along the associated orbits of the model. At $t = 20s$, we alter the glutamate glial reuptake by setting $V_G^{\mathrm{ae}} = 0$. The three cases are obtained with : (a) $\frac{m_G^P}{m_G^I} = 1.7$, (b) $\frac{m_G^P}{m_G^I} = 3.2$, (c) $\frac{m_G^P}{m_G^I} = 2.43$. All other parameters are the same in the three cases and given in Table 1.

Chapter 3

Signature analysis in global MMO and MMBO

MMO patterns are characterized by their signature $\mathcal{L}_1^{s_1}\mathcal{L}_2^{s_2}\mathcal{L}_3^{s_3}\cdots$, where $\mathcal{L}_i$ denotes the number of consecutive large amplitude oscillations and s_i the number of subsequent small oscillations. Periodic signatures with period k are only denoted by finite sequence of length k, $\mathcal{L}_1^{s_1}\mathcal{L}_2^{s_2}...\mathcal{L}_k^{s_k}$.

A challenging question arising from the analysis of MMOs is the change in the signature of the orbits with the change of parameter values. When focusing on the global orbits, such analysis requires both to understand the complex structure of the local dynamics generating the small oscillations, and the control of the global return mechanism to this region of the phase plane. This problem can be tackled for different types of dynamics generating MMOs. In this chapter, we describe the results obtained in two different contexts: in a differentiable three timescale system generating canard-induced MMOs (the GnRH secretion model) and a planar hybrid system (the non-linear adaptive Integrate-and-Fire model).

3.1 Signature variation in MMOs generated by a phantom burster

For canard-induced MMOs, the dynamical structure underlying the generation of the small oscillations is linked with the type of the folded singularity: its analysis, often performed using blow-up methods, enables to characterize the features of each local orbit and, therefore, the number of small oscillations for each. A prototypical example of a folded singularity with small oscillations is the folded node, studied by Benoît [1990], Szmolyan and Wechselberger [2001], and Wechselberger [2005]. These articles focused on the local aspects of the dynamics. An exposition of how the dynamics near the folded node can be combined with a global return mechanism to lead to MMOs was given in Brøns et al. [2006]. This work was used as a basis of various explanations of MMO dynamics found in applications [Ermentrout and Wechselberger, 2009, Rotstein et al., 2008, Rubin and Wechselberger, 2007, Vo et al., 2010]. A shortcoming of the folded node approach is the lack of connection to a Hopf bifurcation that plays a prominent

role in many MMOs. This led to the interest in another, more degenerate folded singularity, known as folded saddle-node of type II (FSNII), originally introduced by Milik et al. [1998] and recently analyzed in some detail by Krupa and Wechselberger [2010]. Guckenheimer [2008] studied a very similar problem in the parameter regime yet closer to the Hopf bifurcation, calling it singular Hopf bifurcation. The transition between the two settings was studied by Curtu and Rubin [2011]. For a more comprehensive overview we refer the reader to the recent review article [Desroches et al., 2012].

Two notions that are central to the study of canard-induced MMOs are secondary canards and sectors of rotation. Secondary canards [Brøns et al., 2006, Wechselberger, 2005] are trajectories which originate in the attracting slow manifold, make a number of small oscillations in the fold region, and continue to the unstable slow manifold. Two trajectories crossing the region between two consecutive canards display the same number of small oscillations. Hence, the regions separated by secondary canards have been called sectors of rotation [Brøns et al., 2006]. As a parameter changes, a periodic orbit may move closer to a canard and pass to the adjacent sector of rotation. Few studies focused on this complex transition, similar to a canard explosion, since chaotic behavior arise, in particular for systems with one fast and two slow variables.

In [9], we have analyzed the dynamical mechanism based on three different timescales that underlies the occurrence of the small oscillations in the GnRH secretion model introduced in section 1.2.1. We proved that, for certain choices of the parameter values, the MMOs, including the pulse phase, surge and pause, exist and are stable limit cycles, even when close to a secondary canard. More precisely, we proved that canards with a specified number of small oscillations are unique (with fixed choices of slow manifolds) and that any two adjacent canards differ by one rotation. Thus we proved that sectors rotation are well-defined and the passage, as a parameter varies, through a secondary canards adds (or subtracts) one small oscillation to the globally attracting orbit. These results are complementary to the results in [De Maesschalck et al., 2014, 2016, Krupa et al., 2008, Krupa and Wechselberger, 2010, Wechselberger, 2005] and relevant to the context of the phantom burster. Finally, coupling this local analysis with the proof of the contraction in each direction resulting from the return mechanism, we proved the existence of an attracting MMO orbit for all parameter values, *i.e.* the transition from an MMO orbit with n small oscillations to an MMO orbit with $n+1$ small oscillations is free of chaotic dynamics, a unique stable periodic orbit exists through the canard transition.

3.1.1 Constraints on the parameters and main theorem

We first warn the reader that parameter ε and δ have been exchanged in [9] compared to system (1.7) used in other publications related to the GnRH secretion model.

Hence, the model becomes:

$$\begin{aligned} \epsilon\delta\dot{x} &= -y + f(x), && \text{(3.1a)}\\ \delta\dot{y} &= a_0 x + a_1 y + a_2 + cX, && \text{(3.1b)}\\ \delta\dot{X} &= -Y + g(X), && \text{(3.1c)}\\ \dot{Y} &= X + b_1 Y + b_2, && \text{(3.1d)} \end{aligned}$$

We refer to this latter notation in this section for the sake of consistency with the corresponding publication. We consider a certain region of the parameter space of system (3.1) for which the Secretor admits a singular point either on the middle or the left branch of the cubic y-nullcline for any X value taken along the Regulator limit cycle. This implies in particular that the Secretor admits 3 singular points: we note $x_{sing}(X)$ the x-component of the middle one. The fact that the result of the subsequent analysis (deterministic transition in the MMO signature) only applies under these assumptions is discussed from the viewpoint of parameter estimation at the end of the section. We assume the following.

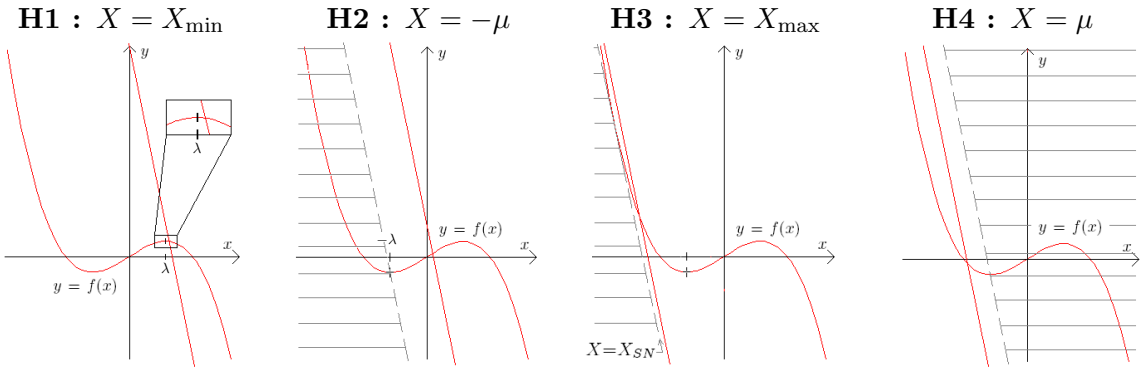

FIGURE 3.1: Illustration of the four hypotheses (H1) to (H4) on parameters to obtain the right system behavior. Hypothesis (H1) requires that the intersection point of y-nullcline with the cubic x-nullcline should be on the right of – and close to – the upper fold. To illustrate the hypotheses (H2) to (H4), we have prescribed the slope of the nullcline, defined by $-a_0/a_1$. Then each of the hypotheses (H2) to (H4) is equivalent to the y-nullcline lying in the corresponding non-hatched half-plane. In each case, the dashed grey line of slope $-a_0/a_1$ is the boundary of the half-plane and represents the position of the y-nullcline in the case of equality associated with the corresponding hypothesis.

(H1) The y-nullcline should pass through the right fold point of the cubic $y = f(x)$ which generates the small oscillations. Hence, we assume that, for $X = X_{\min}$, the y-nullcline should be on the right of – and close to – the upper fold $(\lambda, f(\lambda))$:

$$\lambda \lesssim x_{\text{sing}}(X_{\min}) \quad i.e. \; X_{\min} \lesssim X_f = -\frac{a_0\lambda + a_1 f(\lambda) + a_2}{c}.$$

(H2) Once the y-nullcline has passed the right fold and the relaxation limit cycle of the Secretor appears, the cycle should persist until $X = -\mu$. Hence, we assume that for $X = -\mu$, the y-nullcline intersects the cubic $y = f(x)$ on its middle branch:

$$-\lambda < x_{\text{sing}}(-\mu) \quad i.e. \; -a_0\lambda + a_1 f(-\lambda) + a_2 - c\mu < 0.$$

(H3) From the beginning of the surge phase, the Secretor must admit an attracting node and a saddle on the left branch of the cubic $y = f(x)$. This condition reads

$$a_0 + a_1\lambda_1 > 2\sqrt{a_1 c \lambda_1 X_{\max}} \quad \text{and} \quad x_{\text{sing}}(X_{\max}) < -\lambda.$$

The first part of this condition together with assumption (H4) below implies the second part. Hence, we restrict (H3) to the first part of the condition above which is equivalent

to

$$X_{\max} < X_{SN} = \frac{(a_0 + a_1\lambda_1)^2}{4a_1 c\lambda_1}.$$

Let us note that value X_{SN} of X corresponds to the saddle-node bifurcation of the Secretor occurring when the y-nullcline is tangent to the left branch of the cubic $y = f(x)$.

(H4) Until the end of the surge phase, the Secretor (3.1a)-(3.1b) must admit an attracting node and a saddle on the left branch of the cubic $y = f(x)$ as well. This condition reads

$$-\lambda > x_{\text{sing}}(\mu) \quad i.e. \quad -a_0\lambda + a_1 f(-\lambda) + a_2 + c\mu > 0.$$

Note that (H2) and (H4) are needed for the generation of the adequate pulse-to-surge transition in the generated pattern. (H1) ensures that a pause exists after the surge. (H3) is an additional hypothesis which decipher between certain qualitative features in GnRH Secretion pattern. In particular, large pulse-to-surge amplitude ratio cannot be obtained in that case.

The main result of internal reference [9] is the following theorem.

Theorem 3.1. *Assume that (H1)-(H4) hold. There exists a constant κ such that* [1]*, for any ε small enough and any $\delta < \kappa\varepsilon$, there exists a unique stable limit cycle consisting of a number of small oscillations, a number of pulses and one surge. Some exceptional limit cycles, existing only in exponentially small parameter regions, contain canard segments. All the limit cycles are fixed points of a single passage around the cycle of surge, pause and pulsatility. Varying a regular parameter can lead to a change in the number of pulses or small oscillations by means of a passage through a canard explosion. There are two canard explosions, one associated with the upper fold and another one with the lower fold. A passage through the canard explosion at the upper fold yields a transformation of a small oscillation into a pulse or vice versa. The passage through the canard explosion at the lower fold leads to an addition or a subtraction of a pulse.*

The proof relies on a classical method in global analysis of slow-fast system. Considering a section transverse to the flow, we prove the well-posedness of the return map induced by the flow from this section into itself. We introduce a decomposition of this application by successive transition applications between chosen intermediary sections, namely (see left panel of Figure 3.2)

$$\begin{aligned}
\Sigma^{\text{in}} &= \{(x, y, X, Y) \,:\, y = f(\lambda) - \eta\},\\
\Sigma^{f} &= \{(x, y, X, Y) \,:\, x = \lambda\},\\
\Sigma^{\text{surge}} &= \{(x, y, X, Y) \,:\, x = x_{\text{sing}}(X_{\max}) + \eta\},\\
\Sigma^{\text{endsurge}} &= \{(x, y, X, Y) \,:\, x = x_{\text{sing}}(\gamma) - \eta\}.
\end{aligned}$$

[1] This additional hypothesis ensures that the return map induced by the global flow is contracting. The quantitative statement derives from the comparison between exponential contraction and expansion ratios induced by the flow along the successive phases. Noting X_{-f} the X value for which the slow and fast nullclines cross at the lower fold and $\tilde{f}(x) = -(a_0 x + a_1 f(x) + a_2)/c$, it reads:

$$\varepsilon \int_{x_{\text{sing}}(X_{\max})}^{x_{\text{sing}}(\mu)} \frac{c(\tilde{f}'(x))^2 g'(\tilde{f}(x))dx}{f'(x)(\tilde{f}(x) + b_1 g(\tilde{f}(x)) + b_2)} > \delta \int_{-\lambda}^{\lambda} \left(\frac{(f'(x))^2}{a_0 x + a_1 f(x) + a_2 + cX_{-f}} - \frac{(f'(x))^2}{a_0 x + a_1 f(x) + a_2 + cX_f} \right) dx.$$

with η a small but fixed constant. For each transition function, corresponding mainly to phases from 1 to 4 of the Regulator limit cycle illustrated in Figure 1.7, the GnRH Secretion dynamics can be reduced using a specific reduction to slow manifolds.

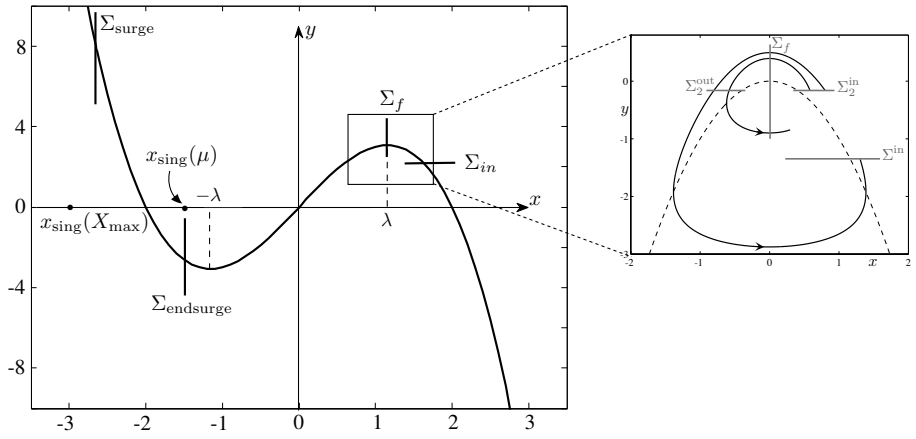

FIGURE 3.2: Sections used for decomposing the return map induced by the global flow represented in the (x, y)-plane. In the vicinity of the fold point (magnified view), a blow-up analysis is performed for characterizing the existence of secondary canards (large amplitude orbit shown) and the canard-induced small oscillations (small amplitude orbit shown) .

Using singular perturbation analysis, we evaluate the amount of contraction (or expansion) of each function according to the timescale separation parameter ε and δ. We therefore prove the exponential contraction of the global return map induced by the flow which ensures the existence and unicity of a fixed point corresponding to an attractive limit cycle. In the following subsections, we stress the key point of the proof: the technical details, in particular the blow-up analysis, can be found in [9].

3.1.2 Reductions of the flow in each phase

Three dimensional reduction with three timescales during the pulsatile phase. Slow motion 1 ($X_{\min} < X < \mu$) corresponds for the Secretor to the oscillatory phase producing the small oscillations and subsequently the pulses in the y-signal. The variables X and Y follow the slowest timescale and the current point (X, Y) remains in a $O(\delta)$-neighborhood of the Regulator critical manifold. This reads $Y = h_\delta(X)$ where $(X, \delta) \mapsto h_\delta(X)$ is an analytic function on $]-\infty, -\mu[\times\mathbb{R}_+^*$ and $h_0 = g$. Thus, on $]-\infty, -\mu[$, $h'_\delta(X) = g'(X) + O(\delta)$.

We introduce a reduced system obtained from (3.1) assuming that $Y = h_\delta(X)$. We differentiate this condition, with δ constant: $\dot{Y} = \dot{X}h'_\delta(X)$. By replacing the dynamics of $\dot{Y}$ in (3.1), one obtains the three-dimensional system with three different timescales:

$$\varepsilon\delta\dot{x} = -y + f(x), \tag{3.2a}$$

$$\delta\dot{y} = a_0x + a_1y + a_2 + cX, \tag{3.2b}$$

$$\dot{X} = \frac{X + b_1(g(X) + O(\delta)) + b_2}{g'(X) + O(\delta)}. \tag{3.2c}$$

Boundary-layer system during the transitions. During fast motions 2 and 4, (X, Y) evolves according to the X timescale and the slowest variable Y is almost constant. After a

time rescaling and setting $\delta = 0$, one obtains the Boundary-Layer System

$$\begin{aligned} \varepsilon\dot{x} &= -y + f(x), && \text{(3.3a)} \\ \dot{y} &= a_0 x + a_1 y + a_2 + cX, && \text{(3.3b)} \\ \dot{X} &= -Y + g(X), && \text{(3.3c)} \end{aligned}$$

with $Y \simeq g(-\mu)$ for fast motion 2 and $Y \simeq g(\mu)$ for fast motion 4.

Two-dimensional reduction with two timescales during the surge phase. Slow motion 3 ($\mu < X < X_{\max}$) corresponds to the surge phase. The current point (x, y) follows the attracting node of the Secretor lying on the left branch of $y = f(x)$. Hence, both approximation $Y \simeq g(X)$ and $y \simeq f(x)$ stand.

By reducing the fastest timescale and setting $Y = g(X)$, one obtains

$$\begin{aligned} \delta f'(x)\dot{x} &= a_0 x + a_1 f(x) + a_2 + cX, && \text{(3.4a)} \\ g'(X)\dot{X} &= X + b_1 g(X) + b_2. && \text{(3.4b)} \end{aligned}$$

Away from the folds of both cubics, we can rewrite (3.4):

$$\begin{aligned} \delta\dot{x} &= \frac{a_0 x + a_1 f(x) + a_2 + cX}{f'(x)}, && \text{(3.5a)} \\ \dot{X} &= \frac{X + b_1 g(X) + b_2}{g'(X)}. && \text{(3.5b)} \end{aligned}$$

Hence we have obtained a two-dimensional slow-fast system with slow variable X and fast variable x.

3.1.3 Local analysis near a folded node with three timescales

Suppose the number of the small rotations for two trajectories (x, y, X) and $(\tilde{x}, \tilde{y}, \tilde{X})$ is different. Then there exists a secondary canard with initial condition somewhere on the segment between (x, y, X) and $(\tilde{x}, \tilde{y}, \tilde{Y})$. This way we can define sectors of the same rotation, or simply sectors of rotation, as the segments of the intersection between the slow manifold and the section Σ^{in} between the consecutive canards. The following theorem leads to a precise definition and description of the sectors of rotation.

Theorem 3.2. *There exists a number $R > 0$ such that, for every $0 < \nu < R$ there exists a family of k^{th} secondary canards with*

$$\frac{\nu}{\delta} < k < \frac{R}{\delta}.$$

The canards with consecutive rotation numbers are next to each other. The distance between the consecutive canards measured in the section Σ^{in} is bounded below by $C_1\delta\sqrt{\varepsilon}$ and above by $C_2\delta\sqrt{\varepsilon}$, where C_1 and C_2 are positive constants.

Corollary 3.3. *The k^{th} sector of rotation, defined as the region between the k^{th} and the $(k+1)^{st}$ secondary canard consists of points whose trajectories make k rotations in the fold region.*

The proof of Theorem 3.2 is based on the application of the blow-up blow up transformation

$$\begin{array}{rccl} \Phi: & \mathbb{R}_+ \times S^4 & \to & \mathbb{R}^4, \\ & (\bar{r}, \overline{x}, \overline{y}, \overline{X}, \overline{\varepsilon}) & \to & (\bar{r}\overline{x}, \bar{r}^2\overline{y}, \bar{r}\overline{X}, \bar{r}^2\overline{\varepsilon}) = (x, y, X, \varepsilon). \end{array} \tag{3.6}$$

to system (3.2) augmented by $\dot{\varepsilon} = 0$. This specific blow-up transformation was used by Dumortier and Roussarie [1996] to study the canard phenomenon and was later slightly adapted by Szmolyan and Wechselberger [2001] to study the folded node.

The four-dimensional sphere S^4 can be identified with a collection of charts and chart-to-chart transformations defined on the overlap of the charts. The local analysis two charts: K1, defined by setting $\bar{y} = -1$, and K2, defined by setting $\bar{\varepsilon} = 1$. Chart K1 is where normal hyperbolicity can be extended. Chart K2 is where at least a part of the timescale separation is lost, in fact if the problem has genuinely just two timescales the system in K2 is no longer slow-fast. In our case we recover a two timescale system in K2. Since we are looking for canards, we wish to make connections from attractive and repulsive slow manifolds. The idea is to extend them to the overlap of K1 and K2, transform them to K2 using the chart-to-chart transformation, and construct the connection in K2.

Finally, note that we define a number of sections of the flow, starting with the entry section Σ^{in}, defined in the original coordinates, then Σ_1^{in}, which is Σ^{in} transformed to K1, Σ_1^{out}, which is the exit section of K1, Σ_2^{in}, which the image by the chart-to-chart transformation of Σ_1^{out} to K2, additional sections in K2, and then similar sections leading from K2 back to K1, near the repulsive slow manifold.

3.1.4 Global attractive limit cycle and small oscillation adding phenomenon

The proof of Theorem 3.1 is based on estimates of both the δ-dependent contraction of the flow during the surge phase, and the maximal ε dependent expansions occurring during the passage through the upper fold of the Secretor (canard-induced small oscillations studied in the local analysis) and the passage from pulsatility to surge. These estimates allows us to state a condition $\delta < \kappa\varepsilon$ ensuring that the contraction overcomes the expansion, ensuring the existence of an isolated fixed point of the return map corresponding to a limit cycle of the whole system.

We illustrate the deterministic signature transition $\mathcal{L}^s$ to $\mathcal{L}^{s+1}$ for varying value of a_2, *i.e.* the addition of a small oscillation in a limit cycle tracked as a_2 changes using numerical continuation method.

It is worth noticing that the fundamental condition (H3), ensuring that the flow is contracting during the whole surge phase, limits the amplitude of the surge in the GnRH secretion generated by the model. Henceforth, the quantitative specifications decipher between different types related to dynamical structure in the GnRH secretion model. For instance, assumption (H3) is violated for the parameter values leading to a GnRH pattern fulfilling the quantitative specifications in the ewe, while it is fulfilled in the case of the rhesus monkey. This difference directly impacts the length of the pause, and its possible variability from one cycle to the subsequent one. The previous study is thus a first step towards the stability analysis of the neuroendocrine control of the ovarian cycle according to the species.

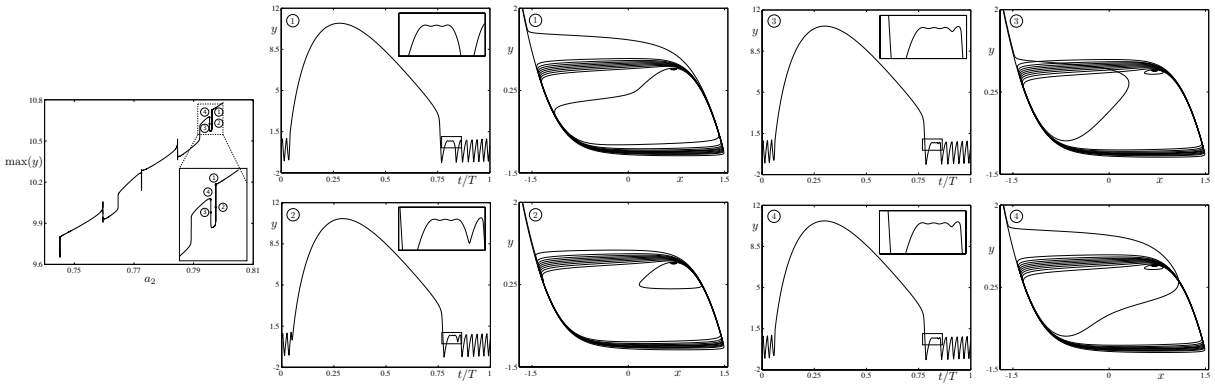

FIGURE 3.3: Family of periodic orbits of system (3.1) when a_2 is varied. The vertical axis shows the maximum in y for each computed limit cycle along the branch. Four orbits have been highlighted with black dots shown in the panels on the right: a small oscillation is added during the passage from orbits 1 to 4.

3.2 MMO and MMBO signature analysis in an integrate-and-fire model

In contrast to the canard-induced MMOs studied in the preceding section, the MMOs emerges in the non-linear integrate-and-fire model (1.1) together with the reset mechanism (1.2) from simpler geometric mechanisms. This relative simplicity allows us to finely characterize the MMO patterns through the study of iterates of a 1D map associated with the hybrid system, called the adaptation map. This map is however singular: it is discontinuous and has unbounded left- and right-derivatives. We have applied and extended rotation theory of circle maps for this class of adaptation maps to precisely characterize the trajectories with respect to the parameters of the system.

3.2.1 Adaptation map

Definition 3.4. The definition domain $\mathcal{D}$ of the adaptation map is the set of adaptation values $w \in \mathbb{R}$ such that the point (v_r, w) does not belong to the stable manifold of the saddle. With any $w \in \mathcal{D}$, the adaptation map associates the value $\Phi(w)$ of the adaption variable after reset for the orbit of the system with initial condition (v_r, w), i.e.

$$\Phi(w) = \gamma W(t^*; v_r, w) + d,$$

where $(V(t; v_r, w), W(t; v_r, w))$ is the solution of equation (1.1) with initial condition (v_r, w) and t^* satisfying $\lim_{t \to t^{*-}} V(t; v_r, w) = \infty$ is the time of the first spike for this solution.

We introduce several objects of interest for the precise description of the adaptation map, shown in Figure 3.4. We focus on the case where the vector field admits a repulsive focus $(v_-, F(v_-) + I)$ and a saddle $(v_+, F(v_+) + I)$ with $v_- < v_+$. We denote by $\mathcal{W}^s$ and $\mathcal{W}^u$ the stable and unstable manifolds of the saddle. Each of these manifolds are made of two branches, and we note $\mathcal{W}^s_-$ the branch of $\mathcal{W}^s$ pointing towards $w < 0$, and $\mathcal{W}^u_-$ and $\mathcal{W}^u_+$ the branches of $\mathcal{W}^u$ pointing towards $v < 0$ and $v > 0$ respectively.

We denote by

• $w^* = F(v_r) + I$ the w-component of the intersection of the reset line $v = v_r$ with the v-nullcline,

• $w^{**} = bv_r$ the intersection of the reset line with the w-nullcline,
• $(w_i)_{i=1}^p$ the sequence of intersections of the reset line with $\mathcal{W}^s$, labeled in increasing order. Except for $v_r = v_-$, there exists a finite number of such points or none depending on the parameter values: an even number of intersections for $v < v_-$ and an odd number for $v > v_-$. In Figure 3.4, we illustrate the case with two intersection points in the magnified view on the unstable focus. We denote by $p_1 = \lceil p/2 \rceil$ the index such that $(w_i)_{i \le p_1}$ are below the v-nullcline and $(w_i)_{i > p_1}$ are above. The points (w_i) split the real line into $p+1$ intervals denoted $(I_i)_{i=0}^p$ corresponding to those in which the number of small oscillations occurring between two consecutive spikes is constant except the interval I_{p_1} which is split into two subintervals by w^*. The number of small oscillations for trajectories starting from I_i is

$$\begin{cases} i & \text{if } i < p_1, \\ (p+1/2) - i & \text{if } i > p_1, \\ p_1 & \text{if } i = p_1 \text{ and } w < w^*, \\ p_1 + 1/2 & \text{if } i = p_1 \text{ and } w > w^* \text{ and } p \text{ is even} \\ p_1 - 1/2 & \text{if } i = p_1 \text{ and } w > w^* \text{ and } p \text{ is odd.} \end{cases} \tag{3.7}$$

We denote by $w^-_{\text{lim}} < w^+_{\text{lim}} < \infty$ the limit of the adaptation variable when $v \to +\infty$ along $\mathcal{W}^u_-$ and $\mathcal{W}^u_+$ respectively and introduce the corresponding values obtained through the reset mechanism:

$$\beta = \gamma w^-_{\text{lim}} + d, \quad \alpha = \gamma w^+_{\text{lim}} + d.$$

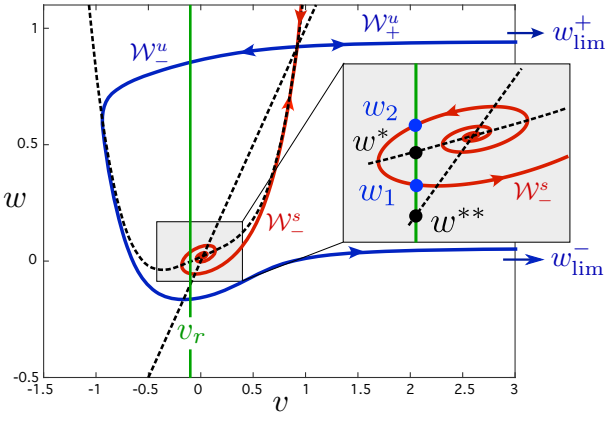

FIGURE 3.4: Geometry of the phase plane with indication of the points relevant in the characterization of the adaptation map Φ. In this example, there are only $p = 2$ intersections of $v = v_r$ with $\mathcal{W}^s$, thus $p_1 = 1$.

Theorem 3.5. *The adaptation map Φ has the following properties.*

1. *It is defined for all $w \in \mathcal{D} = \mathbb{R} \setminus \{w_i\}_{i=1}^p$.*
2. *It is regular (at least C^1) everywhere except at the points $\{w_i\}_{i=1}^p$.*
3. *In any given interval I_i with $i \in \{1 \cdots p+1\}$, the map is increasing for $w < w^*$ and decreasing for $w > w^*$.*

4. *At the boundaries of the definition domain $\mathcal{D}$, $\{w_i\}_{i=1}^p$, the map has well-defined and distinct left and right limits:*

$$\begin{cases} \lim\limits_{w\to w_i^-} \Phi(w) = \alpha \text{ and } \lim\limits_{w\to w_i^+} \Phi(w) = \beta \text{ if } i \leq p_1, \\ \lim\limits_{w\to w_j^-} \Phi(w) = \beta \text{ and } \lim\limits_{w\to w_j^+} \Phi(w) = \alpha \text{ if } j > p_1. \end{cases}$$

5. *The derivative $\Phi'(w)$ diverges at the discontinuity points:*

$$\begin{cases} \lim\limits_{w\to w_i^\pm} \Phi'(w) = +\infty \text{ if } i \leq p_1, \\ \lim\limits_{w\to w_i^\pm} \Phi'(w) = -\infty \text{ if } i > p_1. \end{cases}$$

6. *Φ has a horizontal plateau for $w \to +\infty$ provided that $\lim\limits_{v\to-\infty} F'(v) < -a(b+\sqrt{2})$.*
7. *For $w < \min\left(\frac{d}{1-\gamma}, w_1, w^{**}\right)$, we have $\Phi(w) \geq \gamma w + d > w$.*
8. *If $v_r < v_+$, $\Phi(w) \leq \alpha$ for all $w \in \mathcal{D}$. Moreover, for any w taken between the two branches of the unstable manifold of the saddle, hence in particular for $w \in (w_1, w_p)$, $\Phi(w) > \beta$.*

3.2.2 Infinite number of discontinuity points

We will refer to the points w_i as the discontinuity points of Φ (although Φ is not defined at w_i). We start by treating the case where the adaptation map has an infinite number of discontinuity points for simplicity of notations, before extending our results to the general case. This occurs for $v_r = v_-$, yet the results can be extended to the case where the sub-threshold dynamics has a stable fixed point with a circular attraction basin bounded by the unstable limit cycle (orange region C of the parameter space in Figure 1.1) and the reset line $\{v = v_r\}$ intersects this limit cycle.

Proposition 3.6. *Assume that the reset line has an infinite number of intersections with the stable manifold $\mathcal{W}^s$ of the saddle. If moreover all the discontinuity points $(w_i)_{i\leq p_1}$ (below w^*) belong to $[\beta, \alpha]$, then for every $n \in \mathbb{N}$ and every finite sequence $(s_i)_{i=1}^n$, where $s_i = k_i + l_i/2$, $k_i \in \mathbb{N}$, $l_i \in \{0, 1\}$, there exists an interval $J \subset [\beta, \alpha]$ such that for any $w_0 \in J$, the orbit with initial condition (v_r, w_0) has a transient signature*

$$1^{s_1}1^{s_2}1^{s_3}...1^{s_n}...$$

Note that, in that case, we cannot ensure the stability of the orbit.

3.2.3 Subcases with two discontinuity points

The general case of finite number of discontinuity point is a tremendously difficult question. In [19], we studied the case with two discontinuity points w_1 and w_2 such that $\beta < w_1 < w^* < w_2$ implying that generated MMOs have at most one small oscillation between spikes. Nevertheless, this case splits into several subcases leading already to a large versatility in the signature. The partition of (d, γ) parameter plane according to this subcases is shown in Figure 3.5. We summarize the main results obtained in the different regions. The study is based on the analysis of the rotation number(s) (that can depend on the initial condition).

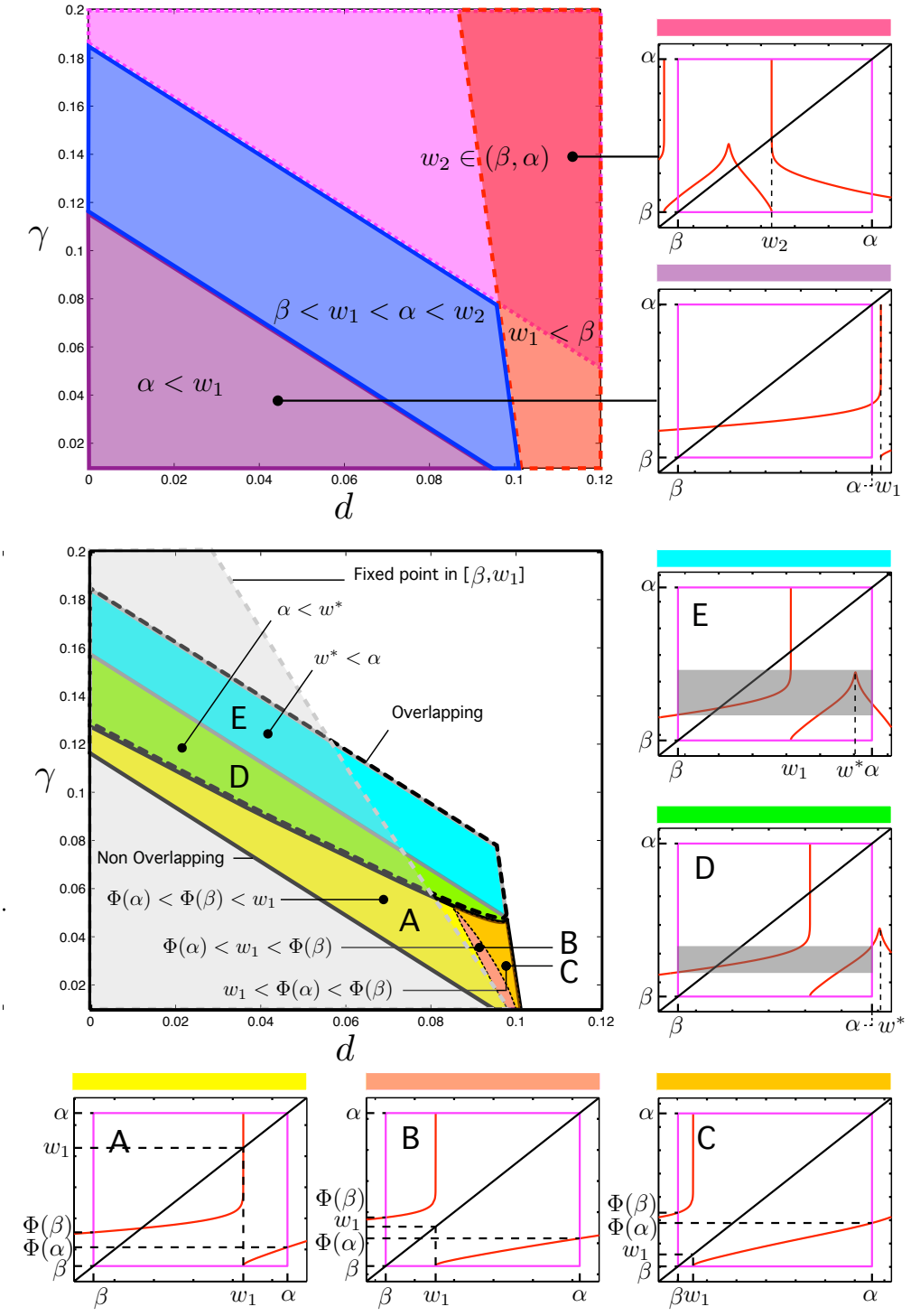

FIGURE 3.5: Partition of (d, γ) parameter space (for fixed values of the other parameters) according to the geometric properties of the Φ map in the case with two intersections points of the reset line with the heteroclinic orbit. For the simulation, we used the quartic function $F = v^4 + 2av$, $a = 0.1$, $b = 1$, $I = 0.1175$ and $v_r = 0.1158$.

Non-overlapping case For introducing a definition of such rotation number, we consider an extension to $\mathbb{R}$ of the adaptation map.

Definition 3.7. Assume that (d, γ) belong to the non-overlapping case (union of regions A, B and C in Figure 3.5). The lift Ψ of $\Phi : \mathcal{I} \to \mathcal{I}$ is defined on $(\beta, \alpha]$ as

$$\Psi = x \in (\beta, \alpha] \mapsto \begin{cases} \Phi(x) & \text{if } \beta < x < w_1 \\ \alpha & \text{if } x = w_1 \\ \Phi(x) + (\alpha - \beta) & \text{if } w_1 < x \leq \alpha. \end{cases} \tag{3.8}$$

For $x \in \mathbb{R}$, we extend Ψ uniquely through the relationship:

$$\forall w \in \mathbb{R}, \quad \forall k \in \mathbb{Z}, \quad \Psi(w + k(\alpha - \beta)) = \Psi(w) + k(\alpha - \beta).$$

Then, provided that the limit exists, the rotation number of Φ (or Ψ) at the point $w \in \mathbb{R}$ is defined as:

$$\varrho(\Psi, w) = \lim_{n \to \infty} \frac{\Psi^n(w) - w}{n(\alpha - \beta)} \tag{3.9}$$

Theorem 3.8. *Assume that (d, γ) belongs to the non-overlapping case. Then the rotation number of map Φ is well-defined and does not depend on w. Moreover, the rotation number is rational $\varrho = p/q \in \mathbb{Q}$ with $p \in \mathbb{N}$ and $q \in \mathbb{N}$ relatively prime if and only if Φ has a periodic orbit, which is related to the MM(B)O pattern fired in the following way:*

1. *If $\varrho = 0$ the model generates tonic asymptotically regular spiking for every initial condition $w_0 \in [\beta, \alpha] \setminus \{w_1\}$.*
2. *If $\varrho = 1$ the model generates asymptotically regular MMOs for every initial condition $w_0 \in [\beta, \alpha] \setminus \{w_1\}$, i.e. the signature is periodic: $1^1 1^1 1^1 ... = (1^1)$.*
3. *If $\varrho = p/q \in \mathbb{Q} \setminus \mathbb{Z}$ (p, q relatively prime, $q > 1$ and $p < q$), then the model generates MMBOs for every initial condition $w_0 \in [\beta, \alpha] \setminus \{w_1\}$. Defining $0 \leq l_1 < \cdots < l_p \leq q - 1$ the integers such that $l_i p/q \mod 1 \geq (q - p)/q$ and $\mathcal{L}_i = l_{i+1} - l_i$ for $i = 1 \cdots p$ (with the convention $l_{p+1} = q + 1$), the MMBO signature is $\mathcal{L}_1^1 \cdots \mathcal{L}_p^1$.*
4. *If $\varrho \in \mathbb{R} \setminus \mathbb{Q}$, then there is no fixed point and no periodic orbit, and the system fires chaotic MMOs.*

Under the same hypothesis, we have proved that the rotation number varies as a devil staircase with d as rigorously stated in the following theorem.

Theorem 3.9. *Assume that for any $d \in [d_1, d_2]$, the adaptation map Φ_d remains in the non-overlapping case and $\Phi_d(\alpha_{d_2}) < \Phi_d(\beta_{d_1})$. Let ϱ_d be the unique rotation number of Φ_d. Then:*

- *$\rho : d \mapsto \varrho_d$ is continuous and non-decreasing;*
- *for all $p/q \in \mathbb{Q} \cap Im(\rho)$, $\rho^{-1}(p/q)$ is an interval containing more than one point, except, maybe, at the boundaries of the interval $\{d_1, d_2\}$;*
- *ρ reaches every irrational number at most once;*
- *ρ takes irrational values on a Cantor-type subset of $[d_1, d_2]$, up to a countable number of points.*

Overlapping case In regions D and E, the rotation number may differ according to the initial condition. We therefore use the notion of rotation interval $[a(\Psi), b(\Psi)]$ with

$$a(\Psi) = \inf_{w\in\mathbb{R}} \liminf_{n\to\infty} \frac{\Psi^n(w)-w}{n(\alpha-\beta)}, \tag{3.10}$$

$$b(\Psi) = \sup_{w\in\mathbb{R}} \limsup_{n\to\infty} \frac{\Psi^n(w)-w}{n(\alpha-\beta)}. \tag{3.11}$$

Theorem 3.10. *Assume that (d,γ) belongs to the overlapping case (union of regions D and E in Figure 3.5) and not Ψ the lift associated with Φ. Then:*

1. *if Φ admits a q-periodic point w with rotation number $\varrho(\Psi,w)=\frac{p}{q}$, then $a(\Psi)\le\frac{p}{q}\le b(\Psi)$;*
2. *if $a(\Psi)<\frac{p}{q}<b(\Psi)$, then Φ admits a periodic point w of period q and rotation number $\varrho(\Psi,w)=p/q$.*

Moreover, for any ϱ_1 and ϱ_2 such that $a(\Psi)\le\varrho_1\le\varrho_2\le b(\Psi)$, there exists w_0 such that

$$\liminf_{n\to\infty}\frac{\Psi^n(w_0)-w_0}{n(\alpha-\beta)}=\varrho_1,\quad \limsup_{n\to\infty}\frac{\Psi^n(w_0)-w_0}{n(\alpha-\beta)}=\varrho_2. \tag{3.12}$$

The second part of the theorem implies in particular that the rotation set in the overlapping case is closed, and that every number $\varrho\in[a(\Psi),b(\Psi)]$ is the rotation number $\varrho(\Psi,w)$ of some $w\in[\beta,\alpha]$.

Tracking the rotation numbers We illustrate numerically the dependence of the rotation numbers (characterizing the MMBO pattern fired) and its possible uniqueness on the values of parameters d and γ.

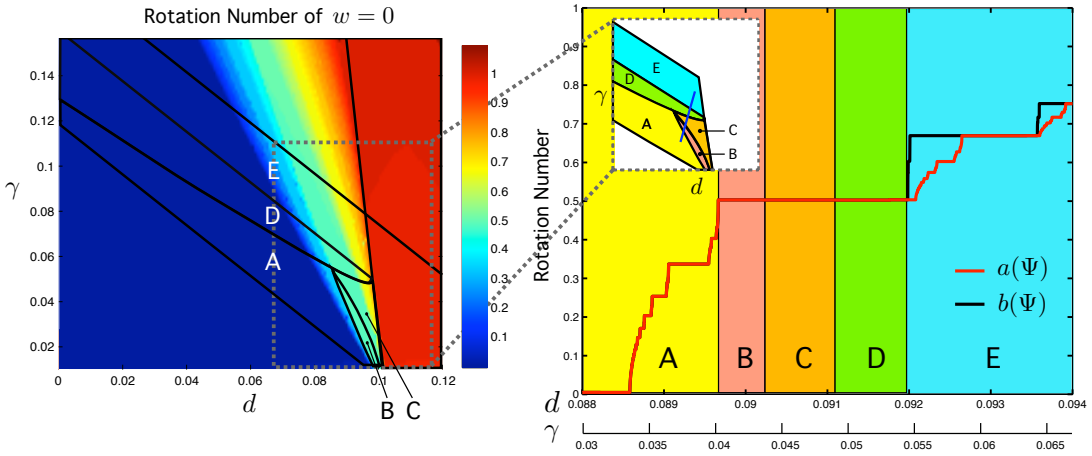

FIGURE 3.6: Rotation numbers according to (d,γ). Left panel : rotation number of $w=0$ together with the boundaries of the regions A to E corresponding to the different subcases when w_1 is the unique discontinuity of the adaptation map lying in the $[\beta,\alpha]$. Right panel : rotation numbers of the left and right lifts Ψ_l and Ψ_r associated with Φ for (d,γ) varying along the blue segment drawn in the insert.

The left panel of Figure 3.6 shows the rotation number associated with the adaptation map of the point $w=0$ as a function of (d,γ). The various regions in the (d,γ)-plane corresponding to the different subcases studied above and already shown in Figure 3.5 are superimposed on the colormap. Several points are worth noticing. First, one can track the appearance and

disappearance of the fixed points according to the value of d and γ together with the evolution of the rotation number or rotation interval. Second, the well-definition of the rotation number or rotation interval has been shown in regions A to E, *i.e.* when considering that the adaptation map features a single discontinuity in the invariant interval.

The right panel of Figure 3.6 illustrates the evolution of the rotation number (or rotation interval) along a segment of (d, γ) values crossing all regions from A to E. We have computed the rotation interval $[a(\Psi), b(\Psi)]$ along this segment.

- In region A, the rotation number associated with Φ is uniquely defined (for any initial condition) and varies along the segment in (d, γ).
- In region B, the rotation number is uniquely defined and constant equal to $1/2$.
- In region C, the rotation number is uniquely defined. Note that the constant value $1/2$ obtained in the simulation only depends on the choice of the segment for (d, γ) values. As shown in the right panel, the rotation number can differ from this value for other values of (d, γ) in region C (*e.g.* in the right part).
- In region D, the rotation number is not uniquely defined in the general case. Nevertheless, along the particular chosen segment (d, γ), $a(\Psi) = b(\Psi) = 1/2$ and the rotation number of Φ does not depend on the initial condition. This particular simulation illustrates a way to evidence that the rotation number is unique by showing that the rotation interval is reduced to a singleton.
- In region E, the rotation interval evolves according to (d, γ) in the tunnel bounded by the black and red lines.

Chapter 4

Synchronization of complex oscillations and network models

Synchronization of coupled oscillators has been widely studied and many studies have focused on the setting of weakly coupled oscillators from a pure mathematical viewpoint (for instance [Coombes and Thul, 2016, Kopell and Ermentrout, 1986, Malkin, 1956]) or applied in neuroscience (for instance [Hansel et al., 1995]). Synchronization depends mainly on the structure of the coupling; some of the frequently considered coupling architectures are "nearest neighbor" [Kopell and Ermentrout, 1986], "all-to-all" [Mirollo and Strogatz, 1990] and coupling depending on a global variable, *e.g.* the average of the phases [Hadley et al., 1988, Rotstein et al., 2003]. More recently some ideas have emerged on how to understand synchronization in the context of slow-fast systems using the limit of strong, rather than weak coupling, see for example [Börgers and Kopell, 2003].

In this chapter, we present contributions to the study of synchronization in the context of applications previously introduced. More precisely, we consider different coupling structure between cell or population dynamics for reproducing the expected structure arising from the corresponding biological system. We therefore reproduce exotic GnRH pattern observed in experimental data by considering two coupled Secretor impacted by the same Regulator. We analyze the effect of either inhibitory or excitatory coupling between two similar cells of ICC, each of them generating MMOs in the uncoupled case. We also consider a network of such cells impacted by the global variable for reproducing episodic synchronization between calcium peaks as observed in GnRH neuron populations.

4.1 Cluster (de)synchronization in a GnRH secretion model with two secretors

The GnRH secretion is far beyond being a simple event and have complex behaviors which remain as open questions. When looking finely at the secretion pattern of GnRH into the portal blood, one can see that, the surge may in some cases be composed of two main bumps instead of a single one (for instance experimental data in [Caraty et al., 1998, Moenter et al., 1990, 1991]. Other interesting observations in the GnRH secretion is the degradation in pulsatility and appearance of noise that blurs the GnRH pulses arising from the desynchronization within the GnRH neuron network, which accompany the increasing pulse frequency at the end of the follicular phase [Evans et al., 1995].

4.1.1 GnRH Secretion model with two coupled neuron subpopulations

In [17], we have built a model adapted from the GnRH secretion system (introduced in section 1.2.1 and studied in sections 2.1 and 3.1) for reproducing a surge with two bumps, accounting two Secretors impacted by the same Regulator (X, Y). Between the two Secretors, we introduce an X-dependent diffusive coupling from the x variables upon the y variables. We consider the following general form for such coupled model:

$$\begin{aligned}
\varepsilon\delta\dot{x_1} &= -y_1 + f(x_1), && \text{(4.1a)}\\
\varepsilon\dot{y_1} &= a_0^{(1)}x_1 + a_1^{(1)}y_1 + V^{(1)}(x_1, x_2, y_1, y_2, X, Y), && \text{(4.1b)}\\
\varepsilon\delta\dot{x_2} &= -y_2 + f(x_2), && \text{(4.1c)}\\
\varepsilon\dot{y_2} &= a_0^{(2)}x_2 + a_1^{(2)}y_2 + V^{(2)}(x_1, x_2, y_1, y_2, X, Y), && \text{(4.1d)}\\
\varepsilon\dot{X} &= -Y + g(X), && \text{(4.1e)}\\
\dot{Y} &= b_0X + b_1Y + b_2, && \text{(4.1f)}
\end{aligned}$$

and

$$\begin{aligned}
y_1^{out}(t) &= y_1(t)\chi_{\{y_1(t)>y_{th}\}}, && \text{(4.2a)}\\
y_2^{out}(t) &= y_2(t)\chi_{\{y_2(t)>y_{th}\}}, && \text{(4.2b)}\\
z(t) &= y_1^{out}(t) + y_2^{out}(t). && \text{(4.2c)}
\end{aligned}$$

We will refer to subsystems (4.1a)-(4.1b) and (4.1c)-(4.1d) as Secretor 1 and 2 (S_1 and S_2) respectively. The global output of the model is $z(t)$ given by (4.2c) as the sum of thresholded S_1 and S_2 outputs. Following the results of parameter estimation for the 4D GnRH Secretion system presented in section 2.1, we choose parameter values for S_1 and S_2 leading to quantitative features in the generated pattern close to the specifications for the ewe, yet we introduce heterogeneity in parameter a_2 and c.

The coupling in (4.1b) and (4.1d) stands for a modulation of the secretor sensitivity to the control exerted by the Regulator, that we assume active only under a threshold value of X. We have therefore introduced an activation function $\psi(X_{sync}, X)$ and X_{sync} a threshold parameter, for instance the sigmoid function:

$$\psi(X_{sync}, X) = \frac{1}{1 + \exp(\rho(X - X_{sync}))}$$

We have considered two types of coupling functions : a so-called constant coupling

$$V^{(1)}(x_1, x_2, y_1, y_2, X, Y) = a_2^{(1)} + c^{(1)}X + g_1(x_1 - x_2)\psi(X_{sync}, X), \tag{4.3a}$$
$$V^{(2)}(x_1, x_2, y_1, y_2, X, Y) = a_2^{(2)} + c^{(2)}X + g_2(x_2 - x_1)\psi(X_{sync}, X), \tag{4.3b}$$

and a so-called dynamical coupling

$$V^{(1)}(x_1, x_2, y_1, y_2, X, Y) = a_2^{(1)} + c^{(1)}X + \hat{g_1}\, y_1^{out}(x_1 - x_2)\psi(X_{sync}, X), \tag{4.4a}$$
$$V^{(2)}(x_1, x_2, y_1, y_2, X, Y) = a_2^{(2)} + c^{(2)}X + \hat{g_2}\, y_2^{out}(x_2 - x_1)\psi(X_{sync}, X). \tag{4.4b}$$

With both coupling we have observed the occurrence of two-bumps surge in a certain region of parameters. In a subregion, we also observe desynchronization between the two Secretors at the end of the pulsatile phase. We have introduced a definition of desynchronization dedicated to the application to GnRH secretion: considering a pulsatile phase, $S1$ and S_2 desynchronize from the first occurrence of two pulses that do not overlap in time.

4.1.2 Dynamical mechanisms

Choosing a value of X_{sync} such that the point $(X_{sync}, g(X_{sync}))$ lies on the middle of the right branch of g (see Figure 4.1(a1, a2)) leads to a deactivation of the coupling function during the first part of the surge, as long as $X(t) > X_{sync}$. If the difference between the parameters of the secretors is sufficient, the 4-phased behavior of secretors interacting through the coupling can be summarized as follows.

1. **Pulsatile regime** $X < 0$**.** The coupling is active, S_1 and S_2 stay synchronized for either the whole pulsatile regime, or a part of it, depending on the parameter values of S_1 and S_2 and the coupling strengths.

2. **Surge triggering**. X increases rapidly and overcomes X_{sync}, which deactivates the coupling. S_1 and S_2 follow their motion along the left branches of $f(x_1)$ and $f(x_2)$ independently.

3. **Surge regime**. As long as $X_{max} > X > X_{sync}$ (first part of the surge), X decreases slowly, S_1 and S_2 move along the left branches of $f(x_1)$ and $f(x_2)$, respectively. In the second part of the surge, the coupling is activated as long as $X_{sync} > X > \gamma$, the secretors get closer to each other as variable y_i decreases in the secretor with greater amplitude while it increases in the other.
   If this two-part regime generates a non-monotonic pattern in z, with an initial increase followed by a decrease, a camel surge is obtained (see for instance, the curves corresponding to $X_{sync} = \{1.8, 1.9, 2\}$ in Panel (b) of Figure 4.1.

4. **Resumption of pulsatility.** X decreases rapidly and triggers the descending parts of the surges followed by the resumption of pulses.

Using quasi-stationary approximations, we have obtained an approximation of the first bump occurrence time as function of the parameters, and therefore, we have obtained a characterization of the X_{sync} values for which the camel surge displays two bumps.

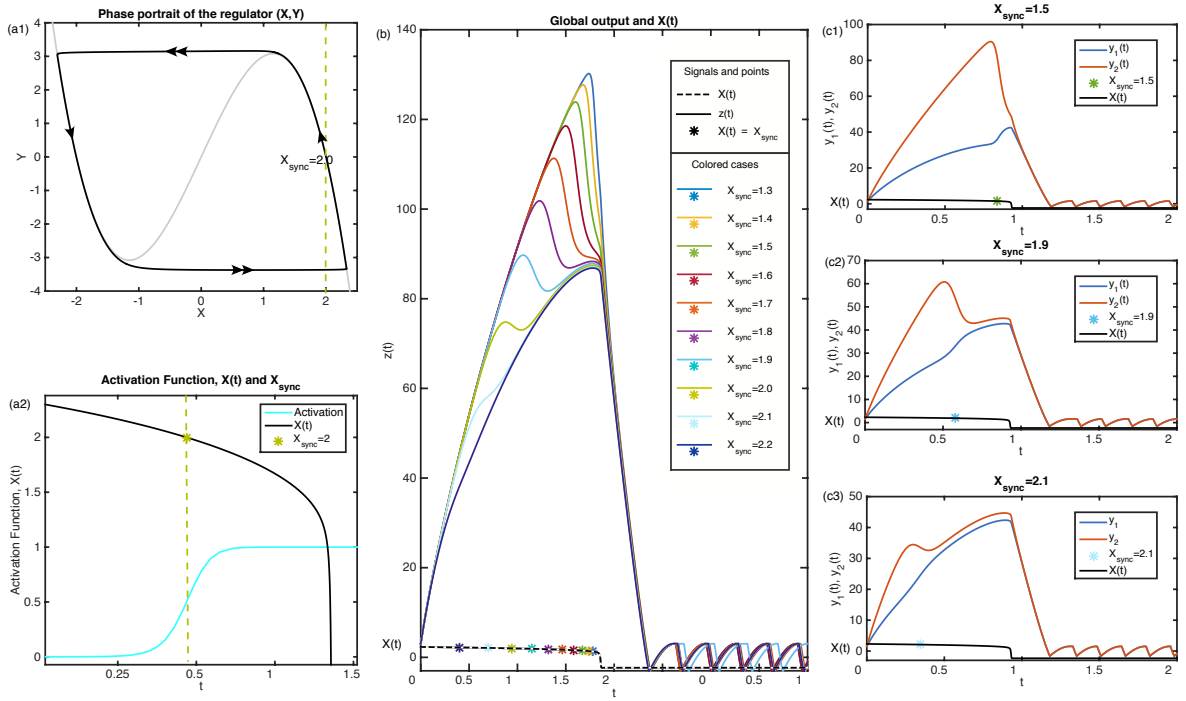

FIGURE 4.1: Activation function $\psi(X_{sync}, X)$ and shaping of a camel surge using constant coupling function. Panel (a1): location of the activation value $X_{sync} = 2$ on the (X, Y) plane. The point $(X_{sync}, g(X_{sync}))$ lies in the middle of the right branch of $Y = g(X)$. Panel (a2): activation signal as a function of time, with initial time chosen at the very beginning of the surge, and change in X starting from its maximal value $X = X_{max}$ and decreasing progressively to reach X_{sync} during the surge. Panel (b): Global output z during the surge according to different values of X_{sync}. Panels (c1-c3): Signals y_i generated with three different values of X_{sync}.

4.1.3 Approximation of the desynchronization between Secretors

The time during which pulses remain synchronized depends on the strength of the coupling and increases with each coupling strengths. We have introduced two different asymptotic tools, namely a 4D quasi-static approach and a geometric approach, for assessing the desynchronization time t^{6D}_{desync} (univocally defined by the value of X at that time denoted by X^{6D}_{desync}).

We take advantage of the timescale separation of the 6D slow-fast feature (4.1). During the pulsatile regime, (X, Y) follows the slowest timescale, while x_i and y_i change at speeds $O(\varepsilon\delta)$ and $O(\varepsilon)$, respectively. Since the change in X is very slow compared to the motion of (x_i, y_i), we consider a reduced system for any fixed value of $X \in [X_{min}, -\mu]$ along the left branch of $Y = g(X)$ by taking $\varepsilon = 0$. The system equations for a constant input $X(t) = X$ with the remaining timescale δ reads:

$$\begin{aligned} \delta \dot{x_1} &= -y_1 + f(x_1), \\ \dot{y_1} &= a_0 x_1 + a_1 y_1 + a_2^{(1)} + c^{(1)} X + \hat{g}_1\, y_1^{out}(x_1 - x_2), \\ \delta \dot{x_2} &= -y_2 + f(x_2), \\ \dot{y_2} &= a_0 x_2 + a_1 y_2 + a_2^{(2)} + c^{(2)} X + \hat{g}_2\, y_2^{out}(x_2 - x_1) \end{aligned} \tag{4.5}$$

which will be simulated for values of $X \in [X_{min}, -\mu]$ to identify X^{4D}_{desync}, *i.e.* the value of X for which the synchronized pulses disappear in (4.5) for a given pair of $(\hat{g}_1, \hat{g}_2)$. The corresponding

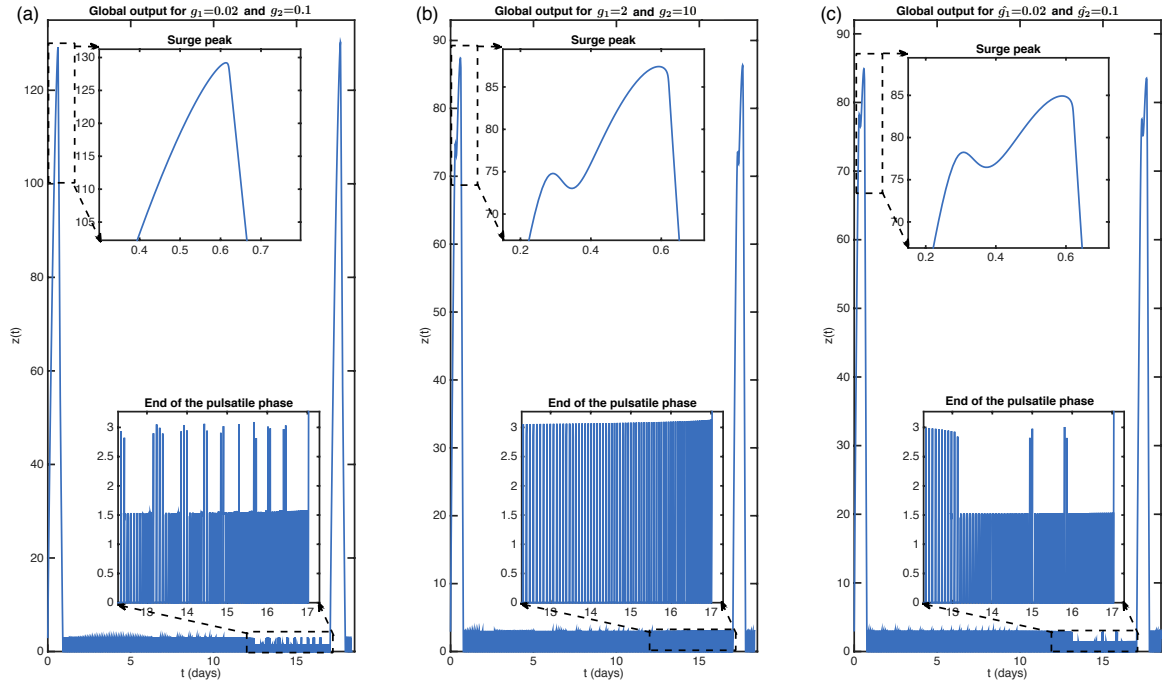

FIGURE 4.2: Signal z for $X_{sync} = 2$. Panel (a) Constant coupling with small coupling strengths $g_1 = 0.02$, $g_2 = 1$; there is no camel surge and the oscillators get desynchronized at the end of the pulsatile regime. Panel (b) Constant coupling with strong coupling strengths $g_1 = 2$, $g_2 = 10$: a camel surge occurs and the oscillators remain synchronized all along the pulsatile regime. Panel (c) Dynamic coupling with small coupling strengths $\hat{g}_1 = 0.02$, $\hat{g}_2 = 0.1$: a camel surge occurs and the oscillators get desynchronized at the end of the pulsatile regime.

desynchronization time t^{4D}_{desync} such that $X^{4D}_{desync} = X(t^{4D}_{desync})$, will be computed from (4.1e) and (4.1f).

The geometric approach is based on our definition of synchronization. The secretors interact via variables y_i, so that the coupling terms directly affect the locations of the y_i-nullclines. Assume that both S_1 and S_2 are on the right branch of the x_i-nullclines and S_2 is ahead ($x_2 < x_1$, $y_2 > y_1$). The coupling may lead to a recurrent bifurcation in S_2 according to the following scenario: when the coupling is switched on, the unstable equilibrium point (x^*_2, y^*_2) lying on the middle branch of $f(x_2)$ moves rightwards and crosses the upper fold. Then, a quasi-stationary equilibrium point appears on the right branch of $f(x_2)$ and slows down the motion of (x_2, y_2), since

$$(a_0 x_2 + a_1 y_2 + a_2^{(2)} + c^{(2)} X) > (a_0 x_2 + a_1 y_2 + a_2^{(2)} + c^{(2)} X + \hat{g}_2\, y_2^{out}(x_2 - x_1))$$

with $\hat{g}_2\, y_2^{out}(x_2 - x_1) < 0$. Once the $(x_2 - x_1)$ difference starts to decrease, the quasi-equilibrium (x^*_2, y^*_2) moves leftwards, crosses the upper fold again and goes back to the middle branch. So that a relaxation limit cycle appears. This 4D geometric approach assumes the following condition: a quasi-equilibrium point, (x^*_2, y^*_2), appears on the right branch when the coupling is switched on, so that S_2 goes on moving slowly, instead of jumping, until S_1 overcomes the y_{th} threshold and produces a pulse. A synchronized pulse can occur if S_1 reaches y_{th} before the leftwards jump of S_2. This will be guaranteed if the quasi-stationary point, (x^*_2, y^*_2), is located at least on the upper fold of the x_2-nullcline, $(\lambda, f(\lambda))$, when $(x_1, y_1) = (x_{th}, y_{th})$ with

$y_{th} = f(x_{th})$, $x_{th} > 0$. This assumption can be expressed from the nullclines of S_2:

$$\begin{aligned} x_2{-}nullcline: &\quad y_2 = f(x_2) \\ y_2{-}nullcline: &\quad y_2 = -\frac{a_0 x_2 + a_2^{(2)} + c^{(2)} X}{a_1 + \hat{g_2}(x_2 - x_1)}, \end{aligned} \tag{4.6}$$

and the maximum X value fulfilling this requirement of synchronization, X_{desync}^{sing}, is given by

$$X_{desync}^{sing} = \frac{-f(\lambda)(a_1 + \hat{g_2}(\lambda - x_{th})) - a_0\lambda - a_2^{(2)}}{c^{(2)}}. \tag{4.7}$$

Note that X_{desync}^{sing} only depends on $\hat{g_2}$ that is the coupling strength of S_2 which is ahead. The desynchronization time assessed according to this geometric approach t_{desync}^{sing} such that $X_{desync}^{sing} = X(t_{desync}^{sing})$ is computed from (4.1e) and (4.1f).

Numerical simulations show that the 4D quasi-static approach matches successfully the desynchronization time of the 6D system output. The geometric approach leads to a poorer result, since both the assessment of X_{desync}^{sing} and t_{desync}^{sing} clearly underestimate the proper values. The effect of $\hat{g_2}$ in the geometric approach is contested: the error in t_{desync}^{sing} values diminishes as $\hat{g_2}$ increases, whereas the error in X_{desync}^{sing} increases. This difference is due to the fact that the change in X (dX/dt) is faster as X approaches $-\mu$, so that a small time step results in a greater change in X than when X is far from the left fold. Even if there is some discrepancy, the values assessed by these approaches, especially the 4D quasi-static approach, can be used as an initial guess to select the parameter values given a priori specifications on the time of the desynchronization.

4.2 A study of the synchronization of two coupled neuron models generating MMOs

4.2.1 A cluster model of intracellular calcium concentrations in neurons

In [16], we have considered two identical oscillators O_1 and O_2 based on the ICCM dynamics, *i.e.* two copies of model (1.5). We consider the same set of parameter values for both, so that they feature the same MMO limit cycle. Such set can be found, following the study presented in section 2.2. We have introduced a bidirectional symmetric and linear coupling between the two oscillators through the fast variable in the slow equation $\dot{y}$ and obtained the following model

$$(O_1) \quad \begin{cases} \dot{x}_1 = (-y_1 + f(x_1) - \phi_{\text{fall}}(Ca_1)), \\ \dot{y}_1 = \varepsilon(x_1 + a_1 y_1 + a_2 + c(x_1 - x_2)), \\ \dot{Ca}_1 = \varepsilon\left(\phi_{\text{rise}}(x_1) - \dfrac{Ca_1 - Ca_b}{\tau_{Ca}}\right), \end{cases} \tag{4.8}$$

$$(O_2) \quad \begin{cases} \dot{x}_2 = (-y_2 + f(x_2) - \phi_{\text{fall}}(Ca_2)), \\ \dot{y}_2 = \varepsilon(x_2 + a_1 y_2 + a_2 + c(x_2 - x_1)), \\ \dot{Ca}_2 = \varepsilon\left(\phi_{\text{rise}}(x_2) - \dfrac{Ca_2 - Ca_b}{\tau_{Ca}}\right). \end{cases} \tag{4.9}$$

We have analyzed both positive and negative values for the coupling gain parameter c to study both excitatory and inhibitory coupling, the synchronization between cell and its property. In particular, we have addressed the question whether the MMO persist in each cell and, in such case, study the property of this synchronization.

First remark that, obviously, the 3D subspace $\{x_1 = x_2, y_1 = y_2, Ca_1 = Ca_2\}$ is an invariant space where there exists an unstable equilibrium point of the 6D system and a limit cycle of the 6D system that is attractive inside that subspace. In other terms, with same initial conditions for O_1 and O_2, the coupling terms do not affect the dynamics of the system, and both systems will behave exactly as if they were uncoupled, having an unstable equilibrium point close to the lower fold and being attracted to the same limit cycle at the same time (synchronized in-phase).

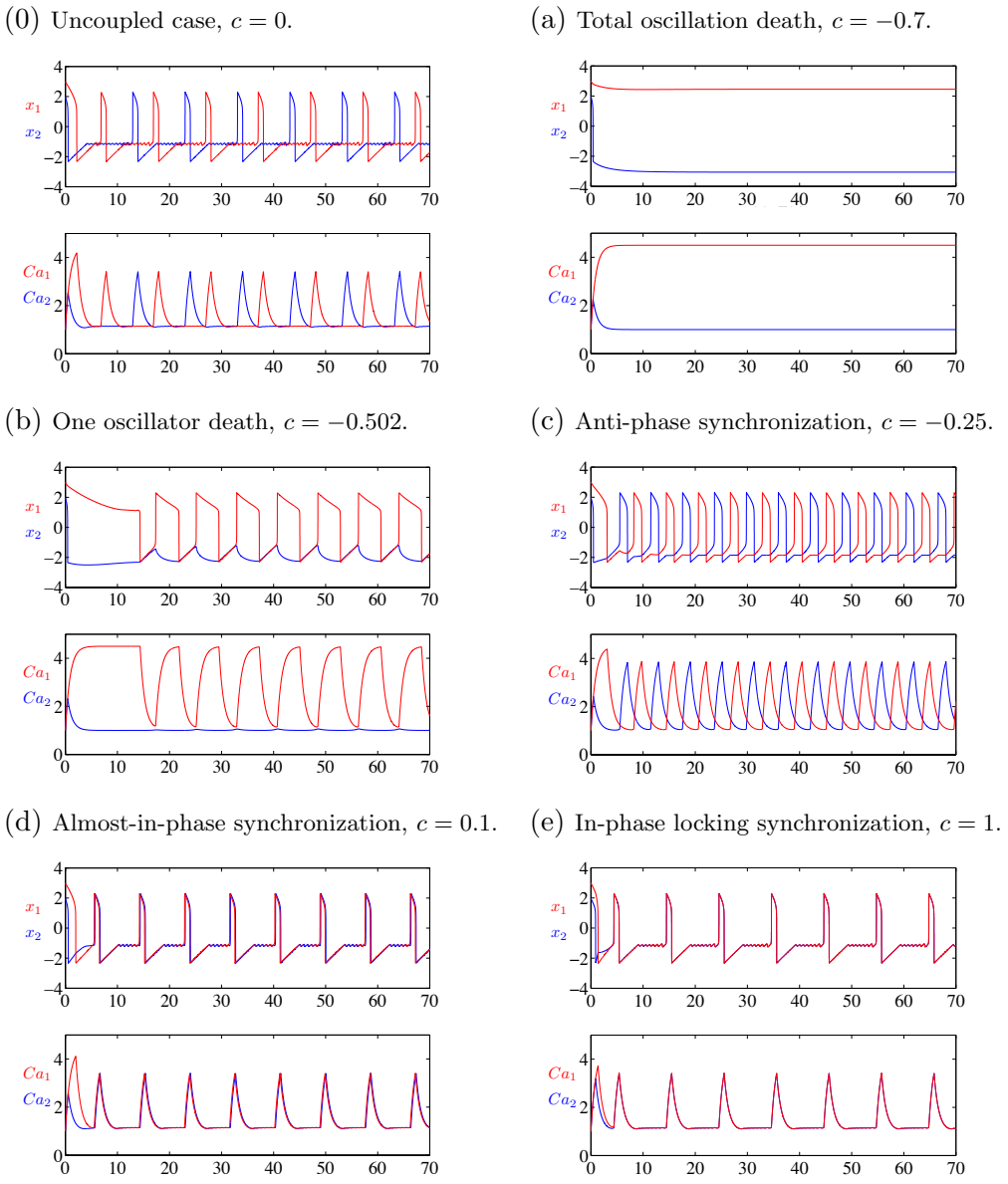

FIGURE 4.3: Representation of the different dynamical patterns that system (4.8)-(4.9) undergoes for different values of c.

We represent in Figure 4.3 (0) the time traces of the first (x_1, x_2) and third (Ca_1, Ca_2) variables in system (4.8)-(4.9) of two identical uncoupled ($c = 0$) oscillators in MMO regime with different initial conditions. When $c \neq 0$, system (4.8)-(4.9) with different initial conditions on each oscillator can display different behaviors depending on c. We represent an instance of each case in Figure 4.3

(a) *Total oscillation death:* both oscillators reach the same stable equilibrium.

(b) *One oscillator death:* one oscillator generates relaxation oscillations, while the other oscillates confined on the left branch.

(c) *Anti-phase synchronization:* the oscillators follow the same periodic or quasi-periodic relaxation orbit, with a half-period phase-shift.

(d) *Almost-in-phase synchronization:* the oscillators follow the same MMO orbit, yet a small phase-shift exists.

(e) *In-phase synchronization:* the oscillators reach asymptotically the MMO limit cycle of the uncoupled case and they are perfectly synchronized.

4.2.2 Main behavior repartition with respect to the coupling strength

We first present a synoptic view of the repartition of the behaviors presented in section 4.2.1 according to parameter c. Figure 4.4 shows return times, shifts and return values associated with the signals generated by O_1 and O_2 according to the value of $c \in [-1, 1]$. Precisely, we note $(x_1^c(t), y_1^c(t), Ca_1^c(t), x_2^c(t), y_2^c(t), Ca_2^c(t))$ the solution of the coupled system for a fixed value of c starting from an initial condition that does not belong to the subspace $\{x_1 = x_2, y_1 = y_2, Ca_1 = Ca_2\}$. We have simulated the solutions for each value of c on a 10^{-3} step grid of $[-1, 1]$ as long as necessary

- either for the orbit to reach the stable equilibrium point (case of total oscillation death, panel (a) in Figure 4.3),
- or for the orbit to cross each section $\{x_1 = 0, y - 1 > 0\}$ or $\{x_2 = 0, y_2 > 0\}$ a hundred times (oscillatory cases, panel (b) to (e) in Figure 4.3).

For each value of c in the grid corresponding to the second case, we have kept the 25 last time values $(t_i^{x_1=0}(c))_{i=1}^{25}$ and $(t_i^{x_2=0}(c))_{i=1}^{25}$. We have calculated the phase shifts between the two oscillators :

$$\phi_i(c) = |t_i^{x_1=0}(c) - t_i^{x_2=0}(c)|, \quad i \in [\![1, 25]\!]. \tag{4.10}$$

Figure 4.4 shows, according to the value of c, the return times $(t_i^{x_1=0}(c))_{i=1}^{25}$ (blue points) and $(t_i^{x_2=0}(c))_{i=1}^{25}$ (green points) respectively and the phase shifts $(\phi_i(c))_{i=1}^{25}$ (red points).

For c in interval A, both oscillators reach a stable equilibrium (panel (a) of Figure 4.3) and, consequently, no return times can be plotted. In intervals B, C and E of c values, the sequences of return times converges to the same limits for both oscillators. Hence, the sets of blue and green points coincide and the blue points are hidden behind the green ones. These cases correspond to cases (b), (c) and (e) of Figure 4.3 respectively. It is also the case for subintervals of D for which the oscillators are in-phase synchronized and generate an MMO orbit. A discrepancy between the return times occur for the other c values in interval D corresponding to almost-in-phase

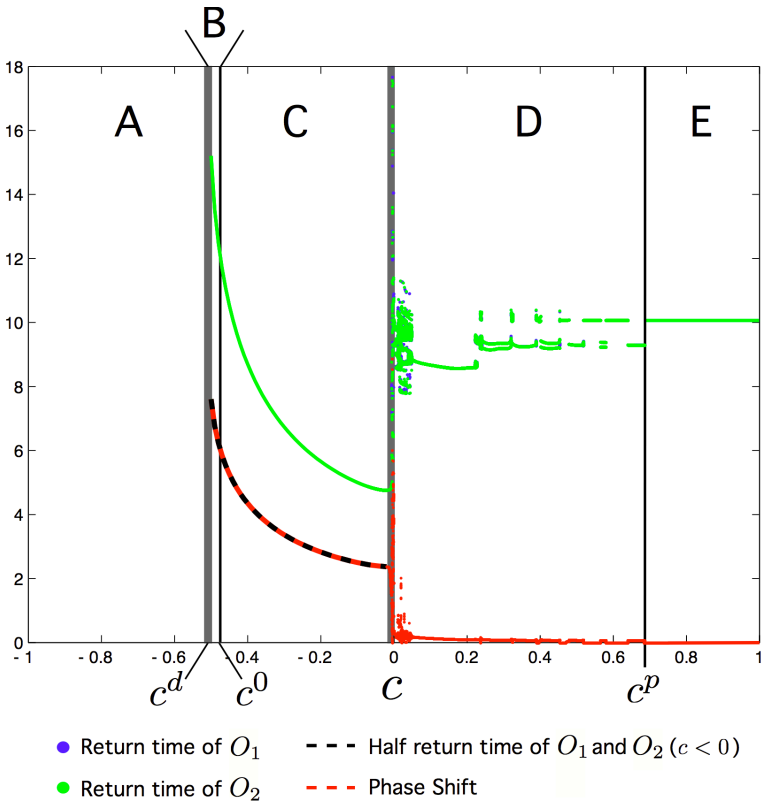

FIGURE 4.4: Global view of the different synchronization patterns described in Theorem 4.1, depending on the value of the coupling parameter c.

synchronization of complex MMO patterns (panel (d) in Figure 4.3). Above interval C, we have also plotted the half of the return time (dashed black line): it coincides precisely with the time shift between oscillators, which highlights the anti-phase synchronization.

The following theorem formalizes the macroscopic structure of this repartition with respect to parameter c shown in Figure 4.4 and the above observations. The proof of this theorem can be found in [16].

Theorem 4.1. *Consider system (4.8)-(4.9). Assume that each subsystem (4.8) and (4.9) possesses the attractive MMOs limit cycle $\gamma_\mu(t)$ when $c = 0$. There exists $0 < \delta \ll 1$, such that, for different initial conditions on each subsystem, the coupled system (4.8)-(4.9) displays the following synchronization patterns, depending on parameter c.*

1. *Case $c > \delta$ (regions D and E in Figure 4.4). There is a phase delayed synchronization pattern. The MMOs persist with the coupling, that is, small oscillations take place in each oscillator before the jump to the right branch of the critical manifold.*

2. *Case $c < -\delta$. We can distinguish three different subcases separated by the limit values $c^d(\mu) < c^0(\mu) < 0$:*

   (a) *If $c \in (c^0(\mu) + \delta, -\delta)$, (region C in Figure 4.4)), there is anti-phase synchronization pattern. The period of the orbit depends on the specific value of c.*

   (b) *For $c \in (c^d(\mu) + \delta, c^0(\mu) - \delta)$, there is a death of one of the oscillators, (region B in Figure 4.4).*

(c) If $c < c^d(\mu) - \delta$, the 6D system (4.8)-(4.9) has a stable equilibrium point, that is, there is a total oscillation death, (region A in Figure 4.4).

The MMOs disappear in the three cases, (see figures 4.3 (a), (b) and (c)). Moreover, $c^0(\mu)$ and $c^d(\mu)$ can be approximated as the single solution c in the interval $(-1, 0)$ of explicit equations (we refer the reader to [16] for the detailed expressions).

4.2.3 Increase of the period with the inhibition strength in the antiphasic case

Figure 4.4 evidences that in region C (case 2.(a) in Theorem 4.1, *i.e.* $c \in (c^0(\mu) + \delta, -\delta)$ and antiphasic synchronization), the oscillation frequency increases with c, *i.e.* the return time increases with the inhibition strength. In this section, we give an approximation of this period for small values of ε by neglecting the duration of the fast parts of the dynamics. We prove that this approximate period decreases while c increases and we provide a global upper bound of its partial derivative with respect to c.

We first give an illustration of the durations that will be computed in the following theorems by mean of Figure 4.5. The asymptotically stable antiphasic cycle benefits from the symmetry between the two coupled identical oscillators. Hence, the active phase during which $x_1 > 0$ and $x_2 < 0$ has the same duration as the active phase during which $x_1 < 0$ and $x_2 > 0$. Similarly, the recovery phase during which $x_1 < x_2 < 0$ has the same duration as the recovery phase during which $x_2 < x_1 < 0$. The global period is then twice the sum of the active phase and the recovery phase durations. For sake of simplicity in the following, we express both approximations T_1 and T_2 of the active phase and recovery phase durations using integrals parameterized by variable x_1 from $x_1^{\max}$ to λ and from x_1^0 to $-\lambda$ respectively, *i.e.* we compute the approximate durations in the cases corresponding to the situations associated with circled T_1 and T_2 in Figure 4.5.

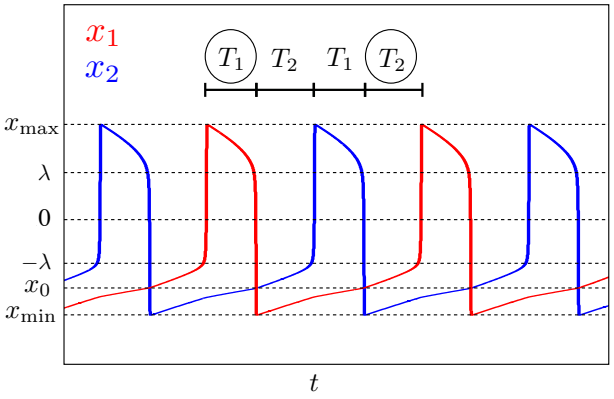

FIGURE 4.5: Decomposition of the global period of the antiphasic pattern into two active phase durations (T_1) and two recovery durations (T_2).

We recall that, during the active phase, the state variables (x_1, y_1, Ca_1) of the first oscillator follow the right slow manifold close to $y_1 = f(x_1, Ca_1), x_1 > \lambda$. Along the corresponding trajectory, x_1 decreases from a maximal value $x_1^{\max}$ to the right fold value λ, and the state variables of the second oscillator remains close to a stable equilibrium point, slowly moving with the value of x_1. Once x_1 becomes less than λ, the first oscillator experiences a fast motion of negligible duration before the beginning of the subsequent recovery phase. The following theorem takes advantage of reductions to the slow manifold and quasi-stationary approximation

to state an integral expression for the duration of (x_1, y_1, Ca_1) slow motion (under the impact of the bidirectional coupling with (x_2, y_2, Ca_2)) corresponding to x from $x_1^{\max}$ to λ. Therefore, it extends to a more sophisticated context the method introduced in [5] for approximating the duration of slow motions in a slow-fast dynamics and building the foliation of the FitzHugh-Nagumo parameter space (see section 2.1.2).

Theorem 4.2. *Assume the hypotheses of Theorem 4.1, 2.(a), ($c \in (c^0(\mu) + \delta, -\delta)$ leading to anti phasic synchronization between oscillators). Consider a parameterization*

$$(x_1(t), y_1(t), Ca_1(t), x_2(t), y_2(t), Ca_2(t))$$

of the limit cycle $\mathcal{C}(c, \varepsilon)$ corresponding to the anti-phase synchronization pattern. The active phase duration, i.e. the time spent by each oscillator close to the right branch of their slow manifold during one cycle, can be approximated at first order in ε by $T_1(c, \varepsilon) + O(1)$ with

$$T_1(c, \varepsilon) = \frac{1}{\varepsilon}\left(\int_{x_1^{\max}}^{\lambda} \frac{f'(x_1) + \frac{\partial \psi_r}{\partial x_1}(x_1, Ca_1, \varepsilon)}{(1+c)x_1 + a_1 f(x_1) - c\tilde{x_2}(x_1, c, \varepsilon) + k_r(x_1, Ca_1, \varepsilon)} dx\right), \tag{4.11}$$

where $\tilde{x_2}(x_1, c, \varepsilon) = x_2^{eq}(x_1, c, \varepsilon) + O(\varepsilon)$, and $x_2^{eq}(x_1, c, \varepsilon)$ denotes the x_2 component of the equilibrium point of system (4.9) moving with x_1 and lying on the left branch of the critical manifold,

$$\begin{aligned} k_r(x_1, Ca_1, \varepsilon) &= a_2 + a_1 \psi_r(x_1, Ca_1, \varepsilon) \\ &- \frac{a_1 \mu Ca_1}{Ca_1 + Ca_d} + \left(\frac{\mu Ca_d}{(Ca_1 + Ca_d)^2} - \frac{\partial \psi_r}{\partial Ca_1}(x_1, Ca_1, \varepsilon)\right)\left(\phi_{\text{rise}}(x_1) - \frac{Ca_1 - Ca_b}{\tau_{Ca}}\right), \end{aligned} \tag{4.12}$$

with ψ_r a differentiable function defined on $(\lambda, x_1^{\max}) \times I_{Ca}^r \times (0, \varepsilon_0)$, with I_{Ca}^r the Ca_1-path while $x_1 \in (\lambda, x_1^{\max})$ along the limit cycle $\mathcal{C}(c, \varepsilon)$, such that

$$\exists \xi_r(\varepsilon) = O(\varepsilon^{2/3}), \quad \forall (x_1, Ca_1) \in (\lambda, x_1^{\max}) \times I_{Ca}^r, \quad |\psi_r(x_1, Ca_1, \varepsilon)| < \xi_r(\varepsilon). \tag{4.13}$$

Theorem 4.3. *With the same hypotheses and notations as in Theorem (4.3), the recovery time of an antiphasic cycle can be approximated at first order in ε by $T_2(c, \varepsilon) + O(1)$ where*

$$T_2(c, \varepsilon) = \frac{1}{\varepsilon}\left(\int_{x_1^0(c)}^{-\lambda} \frac{f'(x_1) + \frac{\partial \psi_l}{\partial x}(x_1, Ca_1, \varepsilon)}{(1+c)x_1 + a_1 f(x_1) - c\hat{x_2}(x_1, c, \varepsilon) + k_l(x_1, Ca_1, \varepsilon)} dx_1\right), \tag{4.14}$$

$x_1^0(c)$ is the x_1 value of the equilibrium point of O_1 at the end of the O_2 active phase, i.e. the unique solution for $x_1 < -\lambda$ of equation

$$a_1(f(x_1) - \phi_{\text{fall}}(Ca_b)) + (1+c)x_1 + a_2 - c\lambda = 0, \tag{4.15}$$

function $\hat{x_2}(x_1, c, \varepsilon)$ is the parameterization of the x_2 value along the part of the limit cycle $\mathcal{C}(c, \varepsilon)$ while $x_1 \in (x_1^{\min}, -\lambda)$,

$$\begin{aligned} k_l(x_1, Ca_1, \varepsilon) &= a_2 + a_1 \psi_l(x_1, Ca_1, \varepsilon) \\ &- \frac{a_1 \mu Ca_1}{Ca_1 + Ca_d} + \left(\frac{\mu Ca_d}{(Ca_1 + Ca_d)^2} - \frac{\partial \psi_l}{\partial Ca_1}(x_1, Ca_1, \varepsilon)\right)\left(\phi_{\text{rise}}(x_1) - \frac{Ca_1 - Ca_b}{\tau_{Ca}}\right), \end{aligned} \tag{4.16}$$

with ψ_l is a differentiable function defined on

$$(x_1^{\min}, -\lambda) \times I_{Ca}^l \times (0, \varepsilon_0),$$

with I_{Ca}^l the Ca_1-path while $x_1 \in (x_1^{\min}, -\lambda)$ along the limit cycle $\mathcal{C}(c, \varepsilon)$, such that

$$\exists \xi_l(\varepsilon) = O(\varepsilon^{2/3}), \forall (x_1, Ca_1) \in (x_1^{\min}, -\lambda) \times I_{Ca}^l, |\psi_l(x_1, Ca_1, \varepsilon)| < \xi_l(\varepsilon). \tag{4.17}$$

Using the two approximations stated above, we can prove the subsequent Theorem (4.4) stating that T_1 and T_2 decrease while c increases in $[c^0(\mu) + \delta, -\delta]$.

Theorem 4.4. *For $c \in [c^0(\mu) + \delta, -\delta]$ and ε small enough,*

$$\frac{\partial T_1}{\partial c}(c, \varepsilon) < 0 \quad \textit{and} \quad \frac{\partial T_2}{\partial c}(c, \varepsilon) < 0 \tag{4.18}$$

Consequently, the first order approximation in ε of the global anti-phasic cycle period, given by $2(T_1(c, \varepsilon) + T_2(c, \varepsilon))$, decreases while parameter c increases and the global oscillation frequency is increasing with c.

4.3 A network model of calcium oscillations in GnRH neurons

4.3.1 Episodic synchronization of calcium peaks in GnRH neurons

Experimental data [Terasawa et al., 1999] have evidenced the existence of isolated episodes of synchronization in the ICC among GnRH neurons[1]: almost all cells begin a peak at approximately the same time and for each cell recruited in the synchronization the height of its calcium peaks during a synchronized peak is higher than the peak heights attained outside of the synchronization periods. These episodes of synchronization are followed by a "post-excitatory suppression" of a few minutes during which calcium levels are at the baseline in all cells. Moreover, the episodes of synchronization occur at regular intervals of nearly 60 minutes. There is also a gradual decrease in the signal amplitude (due to photobleaching) inherent in the experimental protocol and that we did not intend to capture with our modeling study.

Additional experiments have shown the variability in the qualitative organization of these patterns. In particular, partial recruitment of the cells in the synchronized episodes has been identified, and doublets of synchronization have also been observed.

4.3.2 A global variable to control synchronization

In [10], we have proposed a network model of N cells, each one following the cell model of intracellular calcium concentration (1.5), that is able to reproduce the episodic synchronization

[1] See the figure at http://www.jneurosci.org/content/19/14/5898/F5.expansion.html

of calcium peaks observed in Terasawa et al. [1999].

$$\begin{aligned}
\dot{x_j} &= \tau\left(-y_j + f(x_j) - \phi_{\text{fall}}(Ca_j)\right), && \text{(4.19a)}\\
\dot{y_j} &= \tau\varepsilon k_j\left(x_j + a_1 y_j + a_2 - \eta_j \phi_{\text{syn}}(\sigma)\right), && \text{(4.19b)}\\
\dot{Ca_j} &= \tau\varepsilon\left(\phi_{\text{rise}}(x_j) - \frac{Ca_j - Ca_b}{\tau_{Ca}}\right), && \text{(4.19c)}\\
\dot{\sigma} &= \tau\left(\delta\varepsilon\sigma - \gamma(\sigma-\sigma_0)\phi_\sigma\left(\frac{1}{N}\sum_{i=1}^{N} Ca_i - Ca_{\text{desyn}}\right)\right), && \text{(4.19d)}
\end{aligned}$$

for $j = 1, \ldots, N$, with N the number of neurons and

$$\begin{aligned}
\phi_{\text{syn}}(\sigma) &= \frac{1}{1+\exp(-\rho_{\text{syn}}(\sigma-\sigma_{\text{on}}))},\\
\phi_\sigma(u) &= \frac{1}{1+\exp(-\rho_\sigma u)}.
\end{aligned} \qquad \text{(4.20)}$$

Parameters ρ_{syn} and ρ_σ are assumed to be large so that the above sigmoid functions play the role of activation functions, close to Heaviside ones. We assume δ to be small (order of ε), γ large enough relative to ε and δ, and $\sigma_0 < \sigma_{\text{on}}$.

Several differences exist between this approach and the model introduced in the previous section. First we consider a necessary heterogeneity between cells by choosing different parameter values for parameter k: this allows us to reproduce the variability in both the InterPeak Interval (IPI) and the amplitude in the calcium patterns from one cell to another. Second, we add a global variable for inducing synchronization, and not a coupling between each cells. Variable σ represents a global state of the network and acts on each cell through the term $\eta_j\phi_{\text{syn}}(\sigma)$. The differential sensitivity among cells to the impact of σ is reproduced by choosing various values for η_j. Such coupling has been inspired by the work of Hadley et al. [1988] and Rotstein et al. [2003]. Its dynamics consists of a very slow linear part (ε and δ are assumed to be small) and a term that depends on the level of synchronization of the network and acts as a reset mechanism when the network is sufficiently synchronized (function ϕ_σ is applied to the difference between the mean calcium level and the desynchronization threshold Ca_{desyn}).

We briefly explain the σ driven transition of a particular cell of the network from the independent regime to the synchronized regime (see Figure 4.6) and, consequently, how the model can reproduce the alternation of asynchronous phases and episodes of synchronization. Consider an initial value of σ juste above σ_0. While $\sigma < \sigma_{\text{on}}$, $\phi_{\text{syn}}(\sigma)$ is almost zero and, since the values of parameters k_j are different, each cell generates a Ca_j pattern with its own IPI. As a consequence, the calcium peaks are asynchronous and, as time varies, the mean calcium level among cells, given by $\frac{1}{N}\sum_{i=1}^{N} Ca_i$, remains low. As long as it is smaller than Ca_{desyn}, the second term of the σ dynamics is negligible. Then, since δ is assumed to be small, σ increases very slowly. This regime corresponds to the orbit in blue shown in panel A of Figure 4.6 and the blue parts of the time series in panels C to F. Once the mean calcium level exceeds the threshold value σ_{on}, $\phi_{\text{syn}}(\sigma)$ activates. Let us consider the j-th cell: when $\phi_{\text{syn}}(\sigma)$ is activated, the y_j nullcline quickly moves to the right and, provided that η_j is large enough, ends up intersecting the x_j nullcline on its right branch as shown on panel B of Figure 4.6. Hence, as long as $\phi_{\text{syn}}(\sigma)$ is activated, the cell remains in a steady regime. The current point (x_j, y_j) reaches the vicinity of a singular point on the right branch and remains stationary. Therefore,

the corresponding calcium level is higher than usual. Provided that sufficiently many cells are recruited in this process, the mean level quickly becomes higher than Ca_{desyn}. This corresponds to the red parts of the curves in Figure 4.6. Then, the reset term of the σ dynamics activates, σ quickly decreases, crossing back the threshold value σ_{on}, to a value near σ_0. Consequently, $\phi_{\text{syn}}(\sigma)$ is deactivated, and the whole process starts again.

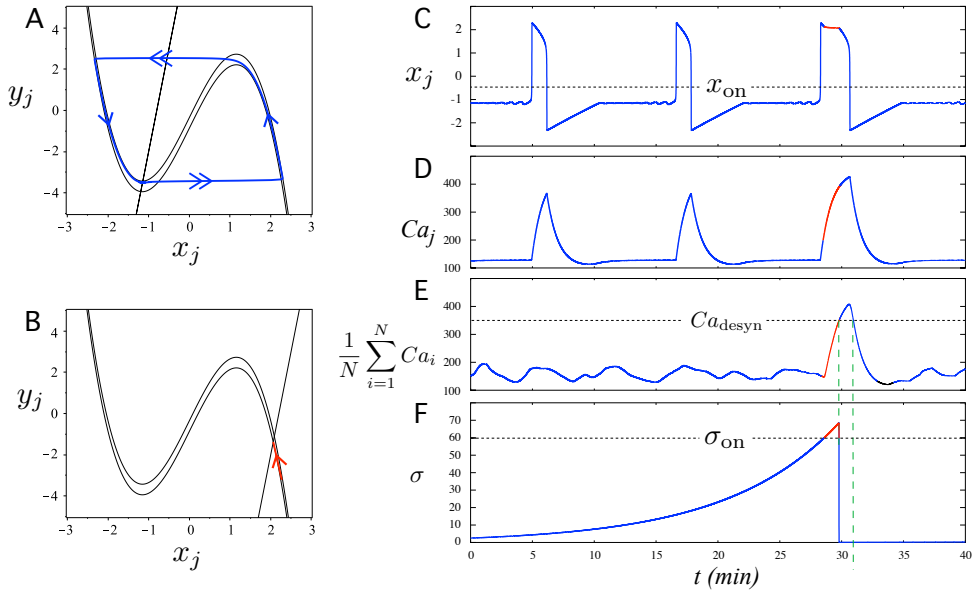

FIGURE 4.6: Transition of the j-th cell of the network from independent to synchronized regime. In each panel, the blue parts correspond to the unsynchronized regime, $\sigma < \sigma_{\text{on}}$ and $\phi_{\text{syn}}(\sigma) \simeq 0$, and the red parts to the synchronized regime, $\sigma > \sigma_{\text{on}}$ and $\phi_{\text{syn}}(\sigma) \simeq 1$.

It is worth noticing that all cells recruited in the event (*i.e.* those corresponding to a large enough value of η_j) were synchronized by the global variable to produce a higher calcium peak than usual. Moreover, they come back to their own pulsatile regime approximately at the same time, starting by a quiescence phase. Hence, all individual calcium levels are at the baseline for a while, before individual peaks rise again unsynchronized, which corresponds to a postexcitatory suppression.

4.3.3 Parameter estimation and sensitivity analysis

We now show how to control the network level parameters σ_0, σ_{on} and δ to obtain global synchronization with a specified frequency. It appears clearly that the evolution of σ depends on the ratio $\sigma_{\text{on}}/\sigma_0$ rather than on each of these parameters independently. Proposition 4.5 gives a formula for the dependence of the frequency of the synchronized peaks on δ and $\sigma_{\text{on}}/\sigma_0$.

Proposition 4.5. *In the case $\rho_\sigma = \infty$, for γ large enough relative to ε and δ, the period between two successive episodes of synchronization in system* (4.19) *is approximated by*

$$T_{\text{syn}} = \frac{1}{\tau\varepsilon\delta} \ln \frac{\sigma_{\text{on}}}{\sigma_0}. \tag{4.21}$$

Using together the results summarized in section 2.2, the qualitative analysis of section 4.3.2 and the above proposition, we have been able to reproduce both the qualitative and quantitative features of the experimental results of Terasawa et al. [1999].

Full synchronization of intracellular calcium peaks in a network of GnRH cells We choose the same value for all parameters η_j, so that the effect of σ on each cell is the same. The value of Ca_{desyn} is chosen just above the mean calcium peak height of individual Ca_j pattern (*i.e.* the one generated by the three-dimensional system (1.5) with parameter values in Table 1). This ensures that random synchronization between few cells will not interrupt the slow increase of σ as the mean calcium level among all cells will not exceed Ca_{desyn}. This happens only if a sufficient number of cells generate at the same time a greater calcium peak than usual.

Panel A of Figure 4.7 displays in the same graph the Ca_j patterns generated by system (4.19) with 50 cells. Outside the synchronization episodes, the oscillations are asynchronous, with each cell producing calcium peaks at its own frequency. Synchronization episodes take place every 61 minutes (at minute 17, 78 and 139). Panel B is a magnified view of the Ca_j patterns during the unsynchronized phase (over a 15 minute interval). Note that, due to the variability in the k_j values, the heights of the calcium peaks and the IPIs differ from one cell to another. Panels C and D show magnified views of two synchronization episodes. All cells are recruited in both episodes, resulting in higher calcium peaks than usual for all cells followed by complete postexcitatory suppression.

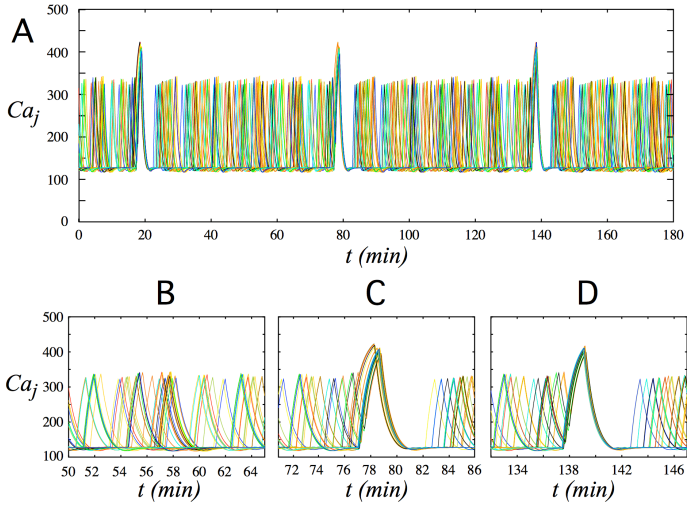

FIGURE 4.7: Patterns of calcium oscillations in a network of 50 GnRH neurons. Panel A shows the individual Ca_j patterns. Panel B displays a magnified view of the asynchronous phase occurring between successive episodes of synchronization. The Ca_j patterns display variability in IPI and height of the peaks between cells. Depending on the phases of each cell when the synchronization is triggered, the calcium peaks may be more or less tightly synchronized as emphasized in Panels C and D.

Partial recruitment As mentioned in the preceding section, parameter η_j tunes the impact of variable σ upon the corresponding cell and, therefore, represents its sensitivity to the impact of the network state. We have mimicked the variability in this sensitivity among cells by choosing different values of η_j with the aim of reproducing the phenomenon of partial recruitment identified by [Terasawa et al., 1999]. Panel A of Figure 4.8 shows the Ca_j patterns generated by the model with η_j chosen randomly. Only 20 cells with sufficiently large value of η_j are completely recruited in the synchronization episodes and generate calcium peaks significantly higher than usual: their Ca_j patterns are assembled in panel B. For 18 other cells (panel C) corresponding to intermediate values of η_j, the Ca_j peaks are not significantly higher than

usual, even if they are synchronized with those in panel B. Moreover, in these Ca_j patterns, the last IPI before the synchronization episode is much shorter than usual which indicates that it does not result from a random coincidence but the cells actually undergo the effect of the synchronization process. Finally, the Ca_j patterns of the 12 remaining cells with low values of η_j (Panel D) are not recruited by the synchronization mechanism: their peak heights are unchanged, their IPI remains constant during the synchronization episode and the calcium level can even be at the baseline.

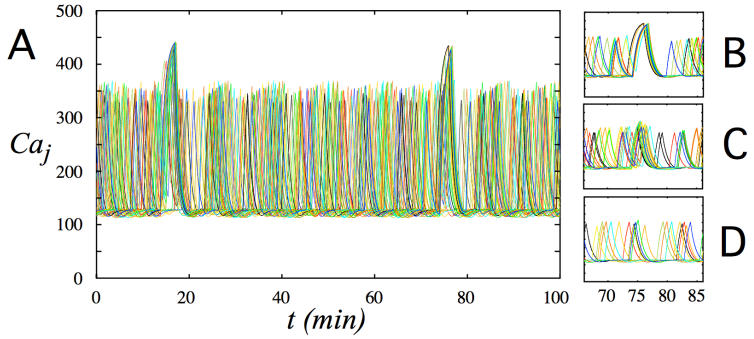

FIGURE 4.8: Patterns of calcium oscillations in a 50 GnRH cells network with various sensitivity to the synchronization process. Panel A shows the Ca_j patterns in all cells. Only a part of the cells participates in the synchronization episodes. The three other panels display magnified views of the second synchronization episodes by assembling the Ca_j patterns in cells which are completely recruited in this event (panel B), recruited with no significant increase in the peak level (panel C) or not recruited at all (panel D).

Doublets As explained previously, the reset mechanism of σ is introduced through a fast part of the dynamics activated by the synchronization of the calcium peaks. The strength of this mechanism is controlled by the value of parameter γ and, in contrast with a classical reset, the decrease of σ can be tuned by choosing the range of γ values. In the preceding simulations, the values of γ were chosen large enough (compared to ε) so that, through the reset mechanism, σ can decrease down to a value very close to σ_0 before the mean calcium level decreases below the threshold Ca_{desyn}. We have reproduce doubled episodes of synchronization[2] by slowing down the σ decrease induced by the synchronization of calcium peaks, *i.e.* by choosing a smaller value of γ.

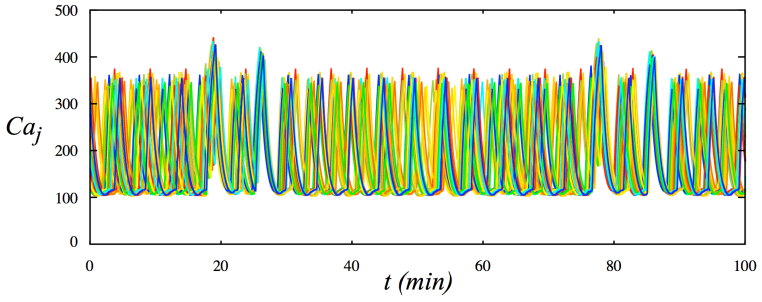

FIGURE 4.9: Synchronization as doublets in patterns of calcium oscillations in the 50 GnRH cells of a network.

[2]Doublets in experimental data: http://www.jneurosci.org/content/19/14/5898/F8.expansion.html

To ensure that, after the episode of synchronization, the mean calcium level decreases as soon as σ starts to decrease, we have selected small enough values of η_j. For the sake of simplicity, we have considered the same value for all η_j, $j \in [\![1, N]\!]$, since the phenomenon of synchronization as doublet does not require variability in the cell sensitivity to synchronization, for obtaining the outputs shown in Figure 4.9. Since the synchronization is not tight, the corresponding peak in the mean calcium level is not much higher than the asynchronous peaks. When σ decreases below σ_{on}, the mean calcium level decreases and quickly becomes smaller than Ca_{desyn}. Parameter γ is small enough so that the σ reset mechanism is not entirely completed: σ starts increasing again from a value much greater than σ_0. Hence, a second episode of synchronization occurs few minutes later (at minute 23) and the corresponding synchronization is tighter than the preceding one, with the calcium peaks occurring in a time interval of 25 second length. The second mean calcium peak of a synchronization doublet is thus higher than the first one. Subsequently, the time needed for the mean calcium level to decrease below Ca_{desyn} is long enough for the σ reset mechanism to be completed. The second doublet of synchronization results from the same mechanism.

Note that the time separating two synchronization episodes of a doublet depends strongly on the value of parameter γ and the tightness of synchronization of the first episode. There is a strong variability in this duration from one doublet to another in a same set of Ca_j patterns. Hence, reproducing a given sequence of doublet is a challenging problem. It is worth noticing that the variability in the doublets reproduced with the model is consistent with the variability observed in the experimental data.

Conclusion and Perspectives

The methods presented in this manuscript result from the application of qualitative analysis tools (mainly bifurcation theory and singular perturbation theory) for retrieving quantitative or semi-quantitative information on the generated outputs of dynamical systems. Designed to tackle the problematic of parameter estimation for neuroscience models, these methods share similarities in the fundamental approach, yet differ according to the features of the dynamics and quantitative specifications considered.

Numerous developments can be imagined for extending these results: we evoke three of them and show three sets of preliminary results of ongoing studies.

Heterogeneity in coupled ICC models. The results presented in section 4.2 concern a coupled system of two identical oscillators (with the same set of parameter values). A natural way to extend the study is to introduce heterogeneity in parameter values among cells and consider the system as a perturbation of the case with identical oscillators. Away from the transition between qualitatively different behaviors, the structural stability of the unperturbed vector field ensures that a hyperbolic limit cycle persists under small perturbation, *i.e.* in case of sufficiently weak heterogeneity between cells. Moreover, the generic bifurcations with respect to c will be shifted yet preserved. We expect to retrieve some information on the repartition of the model behaviors according to c in case of weak heterogeneity among cells. Additional analysis is needed to characterize the new synchronization types obtained in the asymmetric case (see Figure 4.10).

Network model of ICC models. The coupling of two ICC dynamics can be interpreted as an idealized model of two clusters of neurons such that, within each cluster, the neurons are perfectly synchronized. We have already scaled this system by considering each cluster to

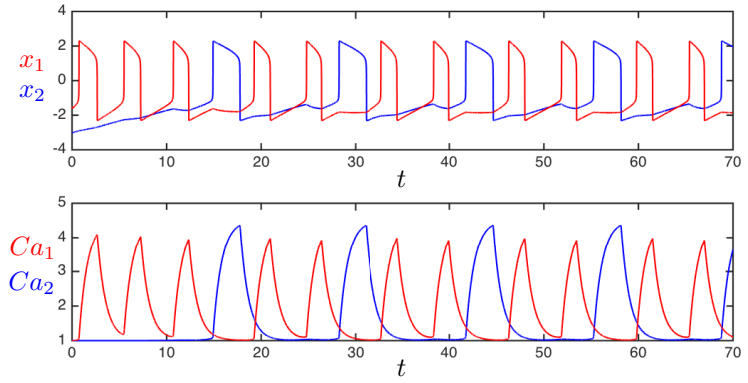

FIGURE 4.10: Instance of calcium oscillation pattern generated by a coupled system of two non-identical ICC dynamics.

be a network of excitatory coupled cells, and inhibiting the other cluster. Such model is well-dedicated to reproduce the interactions between motoneurons, roughly organized as two subpopulations of neurons acting (more or less) jointly. The possible bilateral inhibition between the two subpopulations, suggested by the experimental data, and its precise role in the biological system remains to be characterized. We have successfully reproduced the features of experimental recordings of ICC oscillations in zebrafish motoneurons with our network model (see Figure 4.11 and Figure 1 in [Fallani et al., 2015]). We intend to study the role of inhibition in the model behavior as well as the impact of heterogeneity and connectivity on the synchronization properties, with the aim of inferring the interaction structure of the motoneuron network.

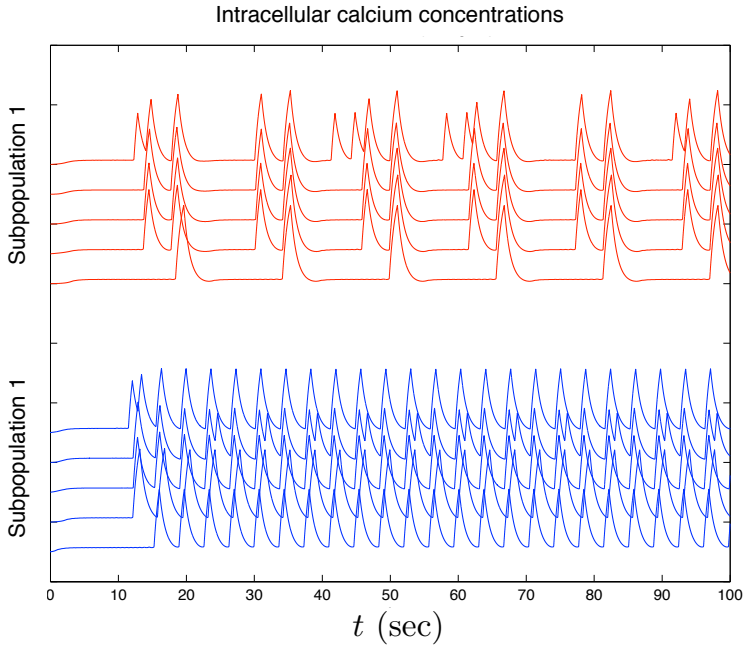

FIGURE 4.11: Patterns of calcium oscillations generated by a clustered ICC network model. Each subpopulation is formed by 5 cells with different parameter values synchronized through an excitatory coupling and the cells of one population inhibit the cells of the other one. The patterns share qualitative and quantitative features with experimental recordings of ICC oscillations in zebrafish motoneurons.

Network model of neuron-glia interactions. We have already developed such network model. Each node represents a voxel formed by local neural and glial populations, whose dynamics is based on the NGMM studied in section 2.4. The coupling between nodes accounts for recent knowledge on diffusive-like interactions between astrocytes in addition to the neural connectivity. We have performed a preliminary numerical study with a reduced number of nodes of the hyperexcitability propagation from a voxel impacted by a deficiency in the astrocytic activity to the other nodes of the network (Figure 4.12). We intend to analyze the differential roles of neural connectivity and astrocyte interactions in the neural activity. With this aim, we will take advantage of the (dynamical) bifurcation analysis performed on the NMM and the NGMM.

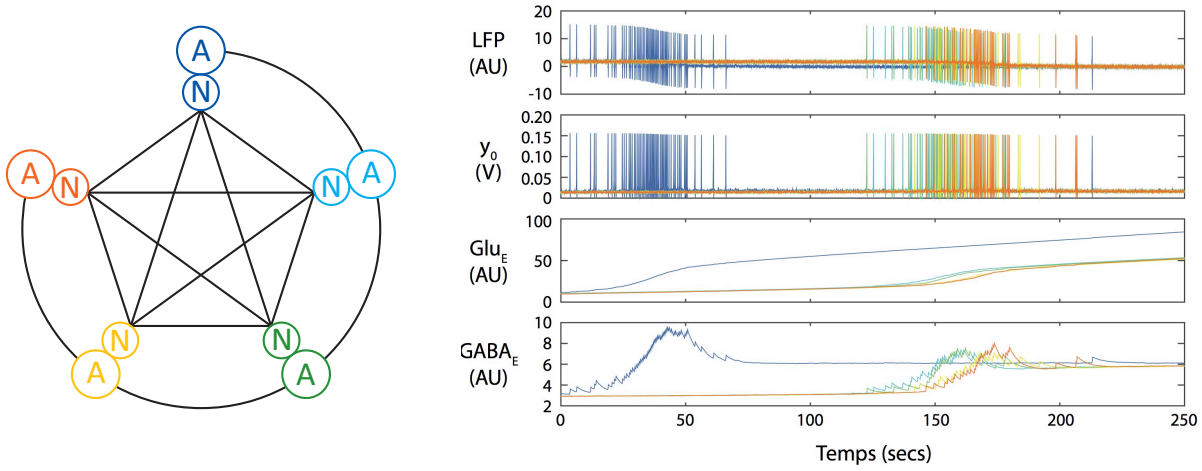

FIGURE 4.12: Propagation of transient hyperexcitability induced by astrocyte deficiency from one node to the other ones in a network of local NGMM accounting for neural connectivity and astrocyte interactions.

Abbreviations and Parameter Table

EEG	**E**lectro-**E**ncephalo**G**raphy
FSH	**F**ollicle-**S**timulating **H**ormone
GABA	**G**amma-**A**mino**B**utiric **A**cid
GnRH	**G**onadotropin **R**eleasing **H**ormone
ICC	**I**ntracellular **C**alcium **C**oncentration
ICCM	**I**ntracellular **C**alcium **C**oncentration **M**odel
LFP	**L**ocal **F**ield **P**otential
LH	**L**uteinizing **H**ormone
MMO	**M**ixed **M**ode **O**scillations
MMBO	**M**ixed **M**ode **B**ursting **O**scillations
MRI	**M**agnetic **R**esonance **I**maging
NIS	**N**oise **I**nduced **S**piking
NIS-OTO	**N**oise **I**nduced **S**piking and **O**ver-**T**hreshold **O**scillations
NIS-STO	**N**oise **I**nduced **S**piking and **S**ub-**T**hreshold **O**scillations
NITAM	**N**oise **I**nduced **T**hresholded **A**mplitude **M**odulation
NMM	**N**eural **M**ass **M**odel
NGMM	**N**euron **G**lia **M**ass **M**odel
NMO	**N**oise **M**odulated **O**scillations
SNIC	**S**addle-**N**ode on **I**nvariant **C**ircle

TABLE 1: Descriptions and values of the neuron-glia mass model parameters

Parameter	Interpretation	Value
	Neuronal compartment	
A	Average excitatory synaptic gain	$3.25\,\mathrm{mV}$
B	Average inhibitory synaptic gain	$22\,\mathrm{mV}$
$\frac{1}{a}$	Time constant of excitatory postsynaptic potentials	$\frac{1}{100}\,\mathrm{s}$
$\frac{1}{b}$	Time constant of inhibitory postsynaptic potentials	$\frac{1}{50}\,\mathrm{s}$
e_0	Half of the maximum discharge rate of a neuronal population	$2.5\,\mathrm{s}^{-1}$
v_0	Basic excitability threshold for neurons	$6\,\mathrm{mV}$
r	Stiffness of neuronal excitability	$0.56\,\mathrm{mV}^{-1}$
C_1	Strength of the synaptic connections from P to P'	135
C_2	Strength of the synaptic connections from P' to P	108
C_3	Strength of the synaptic connections from P to I	33.75
C_4	Strength of the synaptic connections from I to P	33.75
G	Gain of the direct excitatory feedback from P to itself	40
	Glial compartment	
W	Tunes the peak amplitude of glutamate concentrations	$53.6\,\mu\mathrm{M.s}^{-1}$
Z	Tunes the peak amplitude of GABA concentrations	$53.6\,\mu\mathrm{M.s}^{-1}$
w_1	Tune the rise and decay times of glutamate release transfer function	$90\,\mathrm{s}^{-1}$
w_2		$33\,\mathrm{s}^{-1}$
z_1	Tune the rise and decay times of GABA release transfer function	$90\,\mathrm{s}^{-1}$
z_2		$33\,\mathrm{s}^{-1}$
V_G^{en}	Maximal rate of glutamate reuptake by neurons	$0.5\,\mu\mathrm{M.s}^{-1}$
V_G^{ea}	Maximal rate of glutamate reuptake by astrocytes	$4.5\,\mu\mathrm{M.s}^{-1}$
s_g	Activation threshold of sigmoid glutamate reuptakes	$6\,\mu\mathrm{M}$
r_g	Stiffness of sigmoid glutamate reuptakes	$0.9\,\mu\mathrm{M}^{-1}$
V_γ^{ea}	Maximal rate of glial GABA reuptake	$2\,\mu\mathrm{M.s}^{-1}$
K_γ^{ea}	Maximal concentration for Hill dynamics of glial GABA reuptake	$8\,\mu\mathrm{M}$
V_γ^{en}	Maximal rate of neuronal GABA reuptake	$5\,\mu\mathrm{M.s}^{-1}$
K_γ^{en}	Maximal concentration for Hill dynamics of neuronal GABA reuptake	$24\,\mu\mathrm{M}$
V_G^c	Rate of glutamate degradation by astrocytes	$9\,\mu\mathrm{M.s}^{-1}$
V_γ^c	Rate of GABA degradation by astrocytes	$9\,\mu\mathrm{M.s}^{-1}$
	Neuron excitability modulations by neurotransmitter concentrations (feedbacks)	
v_G	Excitability threshold of glutamate feedback function	$30\,\mu\mathrm{M}$
r_G	Stiffness of sigmoid glutamate feedback function induced by glutamate	$0.15\,\mu\mathrm{M}^{-1}$
m_G^P	Maximal coupling gain of glutamate feedback on pyramidal cells	$2.5\,\mathrm{mV}$
m_G^I	Maximal coupling gain of glutamate feedback on interneurons	$1\,\mathrm{mV}$
v_γ	Excitability threshold of GABA feedback function	$25\,\mu\mathrm{M}^{-1}$
r_γ	Stiffness of sigmoid GABA feedback function	$0.12\,\mu\mathrm{M}^{-1}$
m_γ	Maximal coupling gain of GABA feedback	$1\,\mathrm{mV}$

Bibliography

Araque, A., Parpura, V., Sanzgiri, R. P., and Haydon, P. G. (1998). Glutamate-dependent astrocyte modulation of synaptic transmission between cultured hippocampal neurons. The European Journal of Neuroscience, 10(6):2129–2142.

Araque, A., Parpura, V., Sanzgiri, R. P., and Haydon, P. G. (1999). Tripartite synapses: glia, the unacknowledged partner. Trends in Neurosciences, 22(5):208–215.

Aubert, A. and Costalat, R. (2002). A model of the coupling between brain electrical activity, metabolism, and hemodynamics: application to the interpretation of functional neuroimaging. NeuroImage, 17(3):1162–1181.

Aubert, A. and Costalat, R. (2005). Interaction between astrocytes and neurons studied using a mathematical model of compartmentalized energy metabolism. Journal of Cerebral Blood Flow and Metabolism, 25(11):1476–1490.

Aubert, A., Costalat, R., Magistretti, P. J., and Pellerin, L. (2005). Brain lactate kinetics: Modeling evidence for neuronal lactate uptake upon activation. Proceedings of the National Academy of Sciences of the United States of America, 102(45):16448–16453.

Baer, S., Kooi, B., Kuznetsov, Y., and Thieme, H. (2006). Multiparametric bifurcation analysis of a basic two-stage population model. SIAM Journal on Applied Mathematics, 66(4):1339–1365.

Baird, D. T., Swanston, I. A., and McNeilly, A. S. (1981). Relationship between LH, FSH, and prolactin concentration and the secretion of androgens and estrogens by the preovulatory follicle in the ewe. Biology of Reproduction, 24:1013–1025.

Benoît, E. (1990). Canards et enlacements. Publications Mathématiques de l'IHÉS, 72:63–91.

Beurle, R. L. (1956). Properties of a mass of cells capable of regenerating pulses. Philosophical Transactions of the Royal Society of London B: Biological Sciences, 240(669):55–94.

Blanchard, S., Saillet, S., Ivanov, A., Benquet, P., Bénar, C.-G., Pélégrini-Issac, M., Benali, H., and Wendling, F. (2016). A new computational model for neuro-glio-vascular coupling: astrocyte activation can explain cerebral blood flow nonlinear response to interictal events. PloS one, 11(2):e0147292.

Börgers, C. and Kopell, N. (2003). Synchronization in networks of excitatory and inhibitory neurons with sparse, random connectivity. Neural Computation, 15(3):509–538.

Brette, R. and Gerstner, W. (2005). Adaptive exponential integrate-and-fire model as an effective description of neuronal activity. Journal of Neurophysiology, 94:3637–3642.

Brøns, M., Krupa, M., and Wechselberger, M. (2006). Mixed-mode oscillations due to generalized canard phenomenon. In Bifurcation Theory and Spatio-Temporal Pattern Formation, pages 39– 64. Fields Institute Communications.

Campbell, S. L. and Hablitz, J. J. (2008). Decreased glutamate transport enhances excitability in a rat model of cortical dysplasia. Neurobiology of Disease, 32(2):254–261.

Caraty, A., Fabre-Nys, C., Delaleu, B., Locatelli, A., Bruneau, G., Karsch, F. J., and Herbison, A. (1998). Evidence that the mediobasal hypothalamus is the primary site of action of estradiol in inducing the preovulatory gonadotropin releasing hormone surge in the ewe. Endocrinology, 139:1752–1760.

Catchpole, H. R. and Wagenen, G. V. (1975). Reproduction in the rhesus monkey, Macaca mulatta. In Bourne, G. H., editor, The Rhesus Monkey, pages 117–140. Academic Press.

Chever, O., Dossi, E., Pannasch, U., Derangeon, M., and Rouach, N. (2016). Astroglial networks promote neuronal coordination. Science Signaling, 9(410):ra6.

Clément, F. and Françoise, J.-P. (2007). Mathematical modeling of the GnRH-pulse and surge generator. SIAM Journal on Applied Dynamical Systems, 6:441–456.

Coombes, S. and Byrne, Á. (2016). Next generation neural mass models. In Lecture Notes in Nonlinear Dynamics in Computational Neuroscience: from Physics and Biology to ICT. Springer.

Coombes, S. and Thul, R. (2016). Synchrony in networks of coupled non-smooth dynamical systems: Extending the master stability function. European Journal of Applied Mathematics, pages 1–19.

Coombes, S., Thul, R., and Wedgwood, K. (2012). Nonsmooth dynamics in spiking neuron models. Physica D: Nonlinear Phenomena, 241(22):2042–2057.

Curtu, R. and Rubin, J. (2011). Interaction of Canard and Singular Hopf Mechanisms in a Neural Model. SIAM Journal on Applied Dynamical Systems, 10 (4):1443–1479.

De Maesschalck, P., Kutafina, E., and Popović, N. (2014). Three time-scales in an extended bonhoeffer–van der pol oscillator. Journal of Dynamics and Differential Equations, 26(4):955–987.

De Maesschalck, P., Kutafina, E., and Popović, N. (2016). Sector-delayed-hopf-type mixed-mode oscillations in a prototypical three-time-scale model. Applied Mathematics and Computation, 273:337–352.

De Pittà, M., Volman, V., Berry, H., and Ben-Jacob, E. (2011). A tale of two stories: astrocyte regulation of synaptic depression and facilitation. PLoS computational biology, 7(12):e1002293.

Desroches, M., Guckenheimer, J., Krauskopf, B., Kuehn, C., Osinga, H. M., and Wechselberger, M. (2012). Mixed-mode oscillations with multiple time scales. SIAM Review, 54:211–288.

Dumortier, F. and Roussarie, R. (1996). Canard cycles and center manifolds. Memoirs of the A. M. S., 121(577):1–100.

Dumortier, F., Roussarie, R., Sotomayor, J., and Zoladek, H. (1991). Bifurcation of planar vector fields. Lectures Notes in Mathematics, 1480:165–224.

Ermentrout, B. and Wechselberger, M. (2009). Canards, clusters, and synchronization in a weakly coupled interneuron model. SIAM Journal on Applied Dynamical Systems, 8:253–278.

Evans, N. P., Dahl, G. E., Mauger, D. T., Padmanabhan, V., Thrun, L. A., and Karsch, F. J. (1995). Does estradiol induce the preovulatory gonadotropin-releasing hormone (GnRH) surge in the ewe by inducing a progressive change in the mode of operation of the GnRH neurosecretory system? Endocrinology, 136:5511–5519.

Fallani, F. D. V., Corazzol, M., Sternberg, J. R., Wyart, C., and Chavez, M. (2015). Hierarchy of neural organization in the embryonic spinal cord: Granger-causality graph analysis of in vivo calcium imaging data. IEEE Transactions on Neural Systems and Rehabilitation Engineering, 23(3):333–341.

Fenichel, N. (1979). Geometric singular perturbation theory for ordinary differential equations. Journal of Differential Equations, 31:53–98.

FitzHugh, R. (1961). Impulses and physiological states in theoretical models of nerve membrane. Biophysical Journal, 1(6):445.

Freeman, W. (1975). Mass action in the nervous system. Academic Press, New York.

Frick, A., Feldmeyer, D., Helmstaedter, M., and Sakmann, B. (2008). Monosynaptic connections between pairs of l5a pyramidal neurons in columns of juvenile rat somatosensory cortex. Cerebral cortex (New York, N. Y. : 1991), 18(2):397–406.

Griffith, J. S. (1963). A field theory of neural nets: I: Derivation of field equations. Bulletin of Mathematical Biology, 25:111–120.

Griffith, J. S. (1965). A field theory of neural nets: Ii: Properties of the field equations. Bulletin of Mathematical Biology, 27:187–195.

Gruetter, R., Seaquist, E. R., and Ugurbil, K. (2001). A mathematical model of compartmentalized neurotransmitter metabolism in the human brain. American Journal of Physiology. Endocrinology and Metabolism, 281(1):E100–112.

Guckenheimer, J. (2008). Singular hopf bifurcation in systems with two slow variables. SIAM Journal on Applied Dynamical Systems, 7:1355–1377.

Guckenheimer, J. and Meerkamp, P. (2011). Unfoldings of singular hopf bifurcation. SIAM Journal on Applied Dynamical Systems, 11:1325–1359.

Hadley, P., Beasley, M., R., and Wiesenfeld, K. (1988). Phase locking of josephson-junction series arrays. Physical Review B, 38:8712–8719.

Hansel, D., Mato, G., and Meunier, C. (1995). Synchrony in excitatory neural networks. Neural Computation, 7(2):307–337.

Harvey, E., Kirk, V., Wechselberger, M., and Sneyd, J. (2011). Multiple timescales, mixed mode oscillations and canards in models of intracellular calcium dynamics. Journal of Nonlinear Science, 21(5):639–683.

Hodgkin, A. L. and Huxley, A. F. (1952). A quantitative description of membrane current and its application to conduction and excitation in nerve. The Journal of Physiology, 117(4):500–544.

Huang, Y. H., Sinha, S. R., Tanaka, K., Rothstein, J. D., and Bergles, D. E. (2004). Astrocyte glutamate transporters regulate metabotropic glutamate receptor-mediated excitation of hippocampal interneurons. The Journal of Neuroscience: The Official Journal of the Society for Neuroscience, 24(19):4551–4559.

Izhikevich, E. M. (2004). Which model to use for cortical spiking neurons? IEEE Transactions on Neural Networks, 15(5):1063–1070.

Jansen, B. H. and Rit, V. G. (1995). Electroencephalogram and visual evoked potential generation in a mathematical model of coupled cortical columns. Biological Cybernetics, 73(4):357–366.

Jansen, B. H., Zouridakis, G., and Brandt, M. E. (1993). A neurophysiologically-based mathematical model of flash visual evoked potentials. Biological Cybernetics, 68(3):275–283.

Jones, C. K. (1995). Geometric singular perturbation theory. In Dynamical systems, pages 44–118. Springer.

Katznelson, R. D. (1981). Normal modes of the brain: neuroanatomical basis and a physiological theoritical model. In: Nunez P (ed) Electrical fields of the brain: the neurophysics of EEG. Oxford University Press, New York.

Kopell, N. and Ermentrout, G. B. (1986). Symmetry and phaselocking in chains of weakly coupled oscillators. Communications on Pure and Applied Analysis, 39(5):623–660.

Kowianski, P., Lietzau, G., Steliga, A., Waskow, M., and Morys, J. (2013). The astrocytic contribution to neurovascular coupling–still more questions than answers? Neuroscience Research, 75(3):171–183.

Krupa, M., Popović, N., and Kopell, N. (2008). Mixed-mode oscillations in three time-scale systems: A prototypical example. SIAM Journal on Applied Dynamical Systems, 7:361–420.

Krupa, M. and Wechselberger, M. (2010). Local analysis near a folded saddle-node singularity. Journal of Differential Equations, 248:2841–2888.

Lapicque, L. (1907). Recherches quantitatives sur l'excitation électrique des nerfs traitée comme une polarisation. Journal de Physiologie et Pathologie General, 9:620–635.

Lee, M., Schwab, C., and Mcgeer, P. L. (2011). Astrocytes are GABAergic cells that modulate microglial activity. Glia, 59(1):152–165.

Liang, S. L., Carlson, G. C., and Coulter, D. A. (2006). Dynamic regulation of synaptic GABA release by the glutamate-glutamine cycle in hippocampal area ca1. The Journal of Neuroscience, 26(33):8537–48.

Liley, D. T., Cadusch, P. J., and Dafilis, M. P. (2002). A spatially continuous mean field theory of electrocortical activity. Network: Computation in Neural Systems, 13(1):67–113.

Liley, D. T. J. and Walsch, M. (2013). The mesoscopic modeling of burst suppression during anesthesia. Frontiers in Computational Neuroscience, 7(4).

Lopes da Silva, F. H., Hoeks, A., Smits, H., and Zetterberg, L. H. (1974). Model of brain rythmic activity. Kybernetik, 15(1):27–37.

Lopes da Silva, F. H., van Rotterdam, A., Barts, P., van Heusden, E., and Burr, W. (1976). Models of neuronal populations. the basic mechanisms of rhythmicity. Progress in Brain Research, 45:281–308.

Losi, G., Cammarota, M., and Carmignoto, G. (2012). The Role of Astroglia in the Epileptic Brain. Frontiers in Pharmacology, 3.

Losi, G., Mariotti, L., and Carmignoto, G. (2014). Gabaergic interneuron to astrocyte signalling: a neglected form of cell communication in the brain. Philosophical Transactions of the Royal Society of London B, 369(1654):20130609.

Malkin, I. G. (1956). Some Problems in Nonlinear Oscillation Theory (in Russian). Gostexizdat, Moscow.

McKinney, R. A., Debanne, D., Gähwiler, B. H., and Thompson, S. M. (1997). Lesion-induced axonal sprouting and hyperexcitability in the hippocampus in vitro: Implications for the genesis of post-traumatic epilepsy. Nature Medicine, 3:990–996.

Miles, R. and Wong, R. K. (1986). Excitatory synaptic interactions between ca3 neurones in the guinea-pig hippocampus. The Journal of Physiology, 373:397–418.

Milik, A., Szmolyan, P., Löffelmann, H., and Gröller, E. (1998). Geometry of mixed-mode oscillations in the 3-d autocatalator. International Journal of Bifurcation and Chaos, 8(03):505–519.

Mirollo, R. and Strogatz, S. (1990). Synchronization of pulse-coupled biological oscillators. SIAM Journal on Applied Mathematics, 50(6):1645–1662.

Moenter, S. M., Brand, R. C., and Karsch, F. J. (1992). Dynamics of gonadotropin-releasing hormone (GnRH) secretion during the GnRH surge: insights into the mechanism of GnRH surge induction. Endocrinology, 130(5):2978–2984.

Moenter, S. M., Caraty, A., and Karsch, F. J. (1990). The estradiol-induced surge of gonadotropin-releasing hormone in the ewe. Endocrinology, 127:1375–1384.

Moenter, S. M., Caraty, A., Locatelli, A., and Karsch, F. J. (1991). Pattern of gonadotropin-releasing hormone (GnRH) secretion leading up to ovulation in the ewe: existence of a preovulatory GnRH

surge. Endocrinology, 129:1175–1182.

Molaee-Ardekani, B., Benquet, P., Bartolomei, F., and Wendling, F. (2010). Computational modeling of high-frequency oscillations at the onset of neocortical partial seizures: From 'altered structure' to 'dysfunction'. NeuroImage, 52(3):1109–1122.

Molaee-Ardekani, B., Márquez-Ruiz, J., Merlet, I., Leal-Campanario, R., Gruart, A., Sánchez-Campusano, R., Birot, G., Ruffini, G., Delgado-García, J.-M., and Wendling, F. (2013). Effects of transcranial Direct Current Stimulation (tDCS) on cortical activity: A computational modeling study. Brain Stimulation, 6(1):25–39.

Nadkarni, S. and Jung, P. (2005). Synaptic inhibition and pathologic hyperexcitability through enhanced neuron-astrocyte interaction: a modeling study. Journal of Integrative Neuroscience, 4(2):207–226.

Nadkarni, S. and Jung, P. (2007). Modeling synaptic transmission of the tripartite synapse. Physical Biology, 4(1):1–9.

Nagumo, J., Arimoto, S., and Yoshizawa, S. (1962). An active pulse transmission line simulating nerve axon. Proceedings of the IRE, 50(10):2061–2070.

Patel, A. B., de Graaf, R. A., Mason, G. F., Rothman, D. L., Shulman, R. G., and Behar, K. L. (2005). The contribution of GABA to glutamate/glutamine cycling and energy metabolism in the rat cortex in vivo. Proceedings of the National Academy of Sciences of the United States of America, 102(15):5588–5593.

Pinilla, L., Aguilar, E., Dieguez, C., Millar, R.-P., and Tena-Sempere, M. (2012). Kisspeptins and reproduction: physiological roles and regulatory mechanisms. Physiological Reviews, 92:1235–1316.

Pittenger, C., Bloch, M. H., and Williams, K. (2011). Glutamate abnormalities in obsessive compulsive disorder: neurobiology, pathophysiology, and treatment. Pharmacology & Therapeutics, 132(3):314–332.

Postnov, D. E., Koreshkov, R. N., Brazhe, N. A., Brazhe, A. R., and Sosnovtseva, O. V. (2009). Dynamical patterns of calcium signaling in a functional model of neuron-astrocyte networks. Journal of Biological Physics, 35(4):425–445.

Postnov, D. E., Yazanova, L. S., and Sosnovtseva, O. V. (2007). Functional modeling of neural-glial interaction. BioSystems, 89(1-3):84–91.

Richter, T. A., Keen, K. L., and Terasawa, E. (2002). Synchronization of Ca2+ oscillations among primate LHRH neurons and nonneuronal cells in vitro. Journal of Neurophysiology, 88(3):1559–1567.

Robinson, P., Rennie, C., and Wright, J. (1997). Propagation and stability of waves of electrical activity in the cerebral cortex. Physical Review E, 56(1):826–840.

Rotstein, H., Wechselberger, M., and Kopell, N. (2008). Canard Induced Mixed-Mode Oscillations in a Medial Entorhinal Cortex Layer II Stellate Cell Model. SIAM Journal on Applied Dynamical Systems, 7(4):1582–1611.

Rotstein, H. G., Kopell, N., Zhabotinsky, A. M., and Epstein, I. R. (2003). Canard phenomenon and localization of oscillations in the belousov–zhabotinsky reaction with global feedback. The Journal of Chemical Physics, 119(17):8824–8832.

Rubin, J. and Wechselberger, M. (2007). Giant squid - hidden canard: the 3d geometry of the Hodgkin–Huxley model. Biological Cybernetics, 97(1):5–32.

Sahlender, D. A., Savtchouk, I., and Volterra, A. (2014). What do we know about gliotransmitter release from astrocytes? Philosophical Transactions of the Royal Society of London B, 369(1654):20130592.

Salin, P., Tseng, G. F., Hoffman, S., Parada, I., and Prince, D. A. (1995). Axonal sprouting in layer V pyramidal neurons of chronically injured cerebral cortex. Journal of Neuroscience, 15:8234–8245.

Savin, C., Triesch, J., and Meyer-Hermann, M. (2009). Epileptogenesis due to glia-mediated synaptic scaling. Journal of The Royal Society Interface, 6(37):655–668.

Schousboe, A., Bak, L. K., and Waagepetersen, H. S. (2013). Astrocytic control of biosynthesis and turnover of the neurotransmitters glutamate and GABA. Frontiers in Endocrinology, 4:102.

Seifert, G., Schilling, K., and Steinhäuser, C. (2006). Astrocyte dysfunction in neurological disorders: a molecular perspective. Nature Reviews. Neuroscience, 7(3):194–206.

Silchenko, A. N. and Tass, P. A. (2008). Computational modeling of paroxysmal depolarization shifts in neurons induced by the glutamate release from astrocytes. Biological Cybernetics, 98(1):61–74.

Skinner, D. C., Caraty, A., Malpaux, B., and Evans, N. P. (1997). Simultaneous measurement of gonadotropin-releasing hormone in the third ventricular cerebrospinal fluid and hypophyseal portal blood of the ewe. Endocrinology, 138(11):4699–4704.

Stefanescu, R. A. and Jirsa, V. K. (2008). A low dimensional description of globally coupled heterogeneous neural networks of excitatory and inhibitory neurons. PLoS computational biology, 4(11):e1000219.

Szmolyan, P. and Wechselberger, M. (2001). Canards in $\mathbb{R}^3$. Journal of Differential Equations, 177:419–453.

Terasawa, E. I., Schanhofer, W. K., Keen, K. L., and Luchansky, L. (1999). Intracellular Ca2+ oscillations in luteinizing hormone-releasing hormone neurons derived from the embryonic olfactory placode of the rhesus monkey. Journal of Neuroscience, 19:5898–5909.

Thul, R., Bellamy, T. C., Roderick, H. L., Bootman, M. D., and Coombes, S. (2008). Calcium oscillations. In Cellular Oscillatory Mechanisms, pages 1–27. Springer.

Touboul, J. (2008). Bifurcation analysis of a general class of nonlinear integrate-and-fire neurons. SIAM Journal on Applied Mathematics, 68(4):1045–1079.

Van Rotterdam, A., Lopes da Silva, F. H., van den Ende, J., Viergever, M., and Hermans, A. (1982). A model of the spatial-temporal characteristics of the alpha rhythm. Bulletin of Mathematical Biology, 44(2):283–305.

Vo, T., Bertram, R., Tabak, J., and Wechselberger, M. (2010). Mixed mode oscillations as a mechanism for pseudo-plateau bursting. Journal of Computational Neuroscience, 28 (3):443–458.

Volman, V., Bazhenov, M., and Sejnowski, T. J. (2012). Computational models of neuron-astrocyte interaction in epilepsy. Frontiers in Computational Neuroscience, 6:58.

Volman, V., Bazhenov, M., and Sejnowski, T. J. (2013). Divide and conquer: functional segregation of synaptic inputs by astrocytic microdomains could alleviate paroxysmal activity following brain trauma. PLoS Computational Biology, 9(1):e1002856.

Volman, V., Ben-Jacob, E., and Levine, H. (2007). The astrocyte as a gatekeeper of synaptic information transfer. Neural Computation, 19(2):303–326.

Wang, D. and Bordey, A. (2008). The astrocyte odyssey. Progress in Neurobiology, 86(4):342–367.

Wang, Y., Markram, H., Goodman, P. H., Berger, T. K., Ma, J., and Goldman-Rakic, P. S. (2006). Heterogeneity in the pyramidal network of the medial prefrontal cortex. Nature Neuroscience, 9(4):534–542.

Wechselberger, M. (2005). Existence and Bifurcations of Canards in $\mathbb{R}^3$ in the Case of the Folded Node. SIAM Journal on Applied Dynamical Systems, 4:101–139.

Wendling, F., Bellanger, J.-J., Bartolomei, F., and Chauvel, P. (2000). Relevance of nonlinear lumped-parameter models in the analysis of depth-eeg epileptic signals. Biological Cybernetics, 83(4):367–378.

Wilson, H. R. and Cowan, J. D. (1972). Excitatory and inhibitory interactions in localized populations of model neurons. Biophysical Journal, 12(1):1–24.

Wilson, H. R. and Cowan, J. D. (1973). A mathematical theory of the functional dynamics of cortical and thalamic nervous tissue. Kibernetik, 13(2):55–80.

Xia, L., Vugt, D. V., Alston, E. J., Luckhaus, J., and Ferin, M. (1992). A surge of gonadotropin-releasing hormone accompanies the estradiol-induced gonadotropin surge in the rhesus monkey. Endocrinology, 131(6):2812–2820.

Internal References

[1] A. Vidal. Stable periodic orbits associated with bursting oscillations in population dynamics. Lecture Notes in Control and Information Sciences, 341:439–446, 2006.

[2] A. Vidal. Periodic orbits of tritrophic slow-fast systems and double homoclinic bifurcations. Discrete and Continunuous Dynamical Systems, Series B, Suppl. vol.:1021–1030, 2007.

[3] J.-P. Françoise, C. Piquet, and A. Vidal. Enhanced delay to bifurcation. Bulletin of the Belgian Mathematical Society Simon Stevin, 15:825–831, 2008.

[4] A. Vidal, C. Médigue, B. Malpaux, and F. Clément. Endogenous circannual rhythm in LH secretion: insight from signal analysis coupled to mathematical modelling. Philosophical Transactions of the Royal Society A, 367:4759–4777, 2009.

[5] F. Clément and A. Vidal. Foliation-based parameter tuning in a model of the GnRH pulse and surge generator. SIAM Journal on Applied Dynamical Systems, 8(4):1591–1631, 2009.

[6] A. Vidal and F. Clément. A dynamical model for the control of the GnRH neurosecretory system. Journal of Neuroendocrinology, 22:1251–1266, 2010.

[7] A. Vidal and J.-P. Françoise. Canard cycles in global dynamics. International Journal of Bifurcation and Chaos, 22(02):1250026, 2012.

[8] A. Vidal, Q. Zhang, C. Médigue, St. Fabre, and F. Clément. Dynpeak: An algorithm for pulse detection and frequency analysis in hormonal time series. PloS one, 7(7):e39001, 2012.

[9] M. Krupa, A. Vidal, M. Desroches, and F. Clément. Mixed-mode oscillations in a multiple time scale phantom bursting system. SIAM Journal on Applied Dynamical Systems, 11:1458–1498, 2012.

[10] M. Krupa, A. Vidal, and F. Clément. A network model of the periodic synchronization process in the dynamics of calcium concentration in GnRH neurons. Journal of Mathematical Neuroscience, 3(4), 2013.

[11] P.A. Fletcher, F. Clément, A. Vidal, J. Tabak, and R. Bertram. Interpreting frequency responses to dose-conserved pulsatile input signals in simple cell signaling motifs. PloS one, 9(4):e95613, 2014.

[12] A. Garnier, C. Huneau, A. Vidal, F. Wendling, and H. Benali. Identification of dynamical behaviors in epileptic discharges using a neural mass model with double excitatory feedbacks. Proceedings of ICCSA 2014, Normandie University, Le Havre, France, pages 205–210, 2014.

[13] A. Garnier, A. Vidal, C. Huneau, and H. Benali. A neural mass model with direct and indirect excitatory feedback loops: identification of bifurcations and temporal dynamics. Neural Computation, 27:329–364, 2015.

[14] F. Clément and A. Vidal. Modeling the dynamics of gonadotropin-releasing hormone (GnRH) secretion in the course of an ovarian cycle. Computational Neuroendocrinology, p. 284, 2016.

[15] A. Garnier, A. Vidal, and H. Benali. A theoretical study on the role of astrocytic activity in neuronal hyperexcitability by a novel neuron-glia mass model. Journal of Mathematical Neuroscience, In press, 2016.

[16] S. Fernandez-Garcia, A. Vidal, F. Clément, and F.D.V. Fallani. Symmetric coupling of multiple timescale systems with mixed-mode oscillations. To be submitted, 2017.

[17] E. Koksal, A. Vidal, and F. Clément. Coupled multiple timescale dynamics in populations of endocrine neurons: Pulsatile and surge patterns of GnRH secretion. Submitted, 2017.

[18] J. Rubin, J. Signerska-Rynkowska, J. Touboul, and A. Vidal. Wild oscillations in a nonlinear neuron model with resets: (I) Bursting, spike adding and chaos. Submitted, 2017.

[19] J. Rubin, J. Signerska-Rynkowska, J. Touboul, and A. Vidal. Wild oscillations in a nonlinear neuron model with resets: (II) Mixed-Mode Oscillations. Submitted, 2017.